Stray-light characterisation of the GLORIA-Lite limb sounder

Master's Thesis in
Meteorology and Climate Physics
by

Mark Danny Deibele

October 2025

INSTITUTE OF METEOROLOGY AND CLIMATE RESEARCH
KARLSRUHE INSTITUTE OF TECHNOLOGY (KIT)

Supervisor:	PD Dr. Michael Höpfner
Co-supervisor:	Prof. Dr. Björn-Martin Sinnhuber
Advisors:	Felix Friedl-Vallon, Dr. Erik Kretschmer

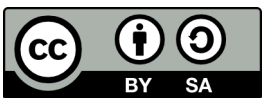

Abstract

GLORIA-Lite is a newly developed lightweight imaging Fourier transform spectrometer (IFTS) developed by IMKASF at KIT and FZ Jülich. It measures thermal infrared emissions of atmospheric components in limb geometry to retrieve temperature and trace gas concentration profiles with high spatial resolution. The instrument features a compact and versatile design by using a double pendulum Michelson interferometer and a monolithic core unit that incorporates the beam splitter and retroreflectors that were aligned together in the manufacturing process. This leads to athermal behaviour of the interferometer as key feature. With a mass of 28 kg and a space demand of 20 l GLORIA-Lite is significantly smaller and simpler as its predecessor GLORIA. The current version of GLORIA-Lite acts as basis for a new generation of compact IFTS instruments suited for a wide range of atmospheric research applications, including future operation on research aircraft, long-duration balloons and small satellite platforms.

Stray light by definition is unwanted light within an optical system. The presence of stray light reduces measurement accuracy and affects the final vertical profiles by bringing additional radiation from other atmospheric regions to the detector. Thus, stray light characterisation is an important part of the further instrument development.

The methods used comprise both a analysis of the data gained during the first balloon campaign and extensive laboratory measurements. During the TRANSAT campaign, GLORIA-Lite performed its maiden flight on a stratospheric balloon at altitudes up to 40 km. During the flight, it obtained atmospheric measurements and demonstrated functionality under campaign conditions. The experimental setup used an uncollimated blackbody with chopper modulation, allowing precise variation of azimuth and elevation angles of the incoming radiation. Data processing was done by a digital lock-in algorithm using Fourier analysis to separate the modulated signal from background radiation.

The results gained from the flight data provided an estimate for the amount of stray light present in the optical system of $5\,\mathrm{nW/cm^2\,sr\,cm^{-1}}$ and showed stray light artifacts caused by the sun. The laboratory measurements could reproduce the effects seen in the flight. The measurement results identified the main stray light effects and their causes. Most of the stray light originates from ghost reflections caused by the wedged beam splitter, double pass reflections within the interferometer and ghost-like reflections from radiation incident at elevations more than 6° above the line of sight (LOS). Other spot-like artifacts from radiation incident at large horizontal angles are assigned to reflections within the interferometer housing. Effects of aperture diffraction were also assessed but this turned out to play a minor role. The point source transmittance (PST) measurement enabled a first instrument model including stray light over ±10° in azimuth and elevation, showing that most stray light originates within ±4° of the LOS. Forward simulations with atmospheric radiance data supported the stray light magnitude derived from flight data.

Design optimization recommendations include reducing reflectivity within the rotating cylinder of the pointing optic module, coating or baffling reflective surfaces in the interferometer housing, minimizing the pass-throughs between the modules, and adding a stray light baffle at the pointing optic module (POM) entrance. These measures follow a “coat or block” strategy to mitigate stray light without major redesigns.

Zusammenfassung

GLORIA-Lite ist ein neu entwickeltes, leichtes, abbildendes Fourier-Transformations-Spektrometer (IFTS), das vom IMKASF am KIT und dem FZ Jülich entwickelt wurde. Es misst thermische Infrarotstrahlung von atmosphärischen Bestandteilen in der Limb-Geometrie, um Vertikalprofile von Spurengaskonzentrationen und Temperatur mit hoher räumlicher Auflösung abzuleiten. Das Instrument zeichnet sich durch ein kompaktes Design aus, das ein Michelson-Interferometer in Doppelpendelbauweise und einen monolithischen Strahlteilerblock beinhaltet. Im Strahlteilerblock werden der Strahlteiler und die Retroreflektoren bereits während der Herstellung zusammen ausgerichtet. Der monolithische Strahlteilerblock führt zu athermalen Verhalten des Interferometers als zentrale Eigenschaft. Mit einer Masse von 28 kg und einem Platzbedarf von 20 l ist GLORIA-Lite deutlich kleiner und einfacher als sein Vorgänger GLORIA. Die aktuelle Version von GLORIA-Lite dient als Grundlage für eine neue Generation kompakter IFTS-Instrumente, die für ein breites Spektrum atmosphärischer Forschungsanwendungen geeignet sind, einschließlich zukünftiger Einsätze auf Forschungsflugzeugen, Langzeitballons und Cubesats.

Streulicht ist per Definition unerwünschtes Licht innerhalb eines optischen Systems. Das Vorhandensein von Streulicht reduziert die Messgenauigkeit und beeinflusst die endgültigen vertikalen Profile, indem zusätzliche Strahlung aus anderen atmosphärischen Regionen auf den Detektor gebracht wird. Daher ist die Charakterisierung von Streulicht ein wichtiger Bestandteil der weiteren Instrumentenentwicklung. Die verwendeten Methoden umfassen sowohl die Analyse der während der ersten Ballonmission gewonnenen Daten als auch umfangreiche Laboruntersuchungen. Während der TRANSAT-Kampagne absolvierte GLORIA-Lite seinen Erstflug auf einem Stratosphärenballon in Höhen von bis zu 40 km. Während des Flugs wurden atmosphärische Messungen durchgeführt und die Funktionalität des Instruments unter Einsatzbedingungen nachgewiesen.

Der experimentelle Aufbau verwendet einen unkolimierten Schwarzkörper mit Chopper-Modulation, wodurch eine präzise Variation der Azimut- und Elevationswinkel der einfallenden Strahlung möglich war. Die Datenverarbeitung erfolgte mittels eines digitalen Lock-in-Algorithmus mit Verwendung der Fourier-Analyse, um das modulierte Signal von der Hintergrundstrahlung zu unterscheiden. Die aus den Flugdaten gewonnenen Ergebnisse lieferten eine erste Abschätzung der im optischen System vorhandenen Streulichtintensität von $5\,\mathrm{nW/cm^2\,sr\,cm^{-1}}$ und zeigten Streulichtartefakte, die durch die Sonne verursacht wurden. Die Laboruntersuchungen konnten die während des Flugs beobachteten Effekte reproduzieren. Die Messergebnisse identifizierten die wichtigsten Streulicht-Effekte und deren Ursachen. Ein Großteil des Streulichts stammt von Geisterreflexionen durch den keilförmigen Strahlteiler, Doppelpass-Reflexionen innerhalb des Interferometers und geisterähnlichen Reflexionen von Strahlung, die von Elevationswinkeln oberhalb 6° der Sichtlinie in das Instrument gelangt. Weitere punkförmige Reflexe werden durch Strahlung die unter großen azimuthwinkeln einfällt verursacht. Diese werden Reflexionen innerhalb des Interferometergehäuses zugeschrieben. Effekte der Aperturbeugung wurden ebenfalls betrachtet, es zeigte sich jedoch, dass diese eine untergeordnete rolle spielen. Die Messung der PST produzierte ein erstes Instrumentenmodell das Streulicht einschließt und einen Winkelbereich von $\pm 10°$ in Azimut und Elevation umfasst. Dabei wurde gezeigt,dass der Großteil des Streulichts aus einem

Winkelbereich von $\pm 4^\circ$ kommt. Vorwärtsrechnungen mit atmosphärischen Strahlungsdaten bestätigten die aus den Flugdaten abgeleitete Streulichtstärke.
Empfehlungen zur Designoptimierung umfassen die Reduzierung der Reflexion innerhalb des rotierenden Zylinders des Pointing-Optik-Moduls, die Beschichtung reflektierender Flächen im Interferometergehäuse mit Materialien höherer Emissivität oder der Einbau von Streulichtblenden, sowie die reduzierung der Durchgänge zwischen den Modulen und das Hinzufügen einer Streulichtblende am Eingang des POM. Diese Maßnahmen folgen einer „beschichten oder blockieren“-Strategie, um Streulicht zu reduzieren, ohne größere Anderungen am optischen oder mechanischen Design vornehmen zu müssen.

Contents

1 Introduction

1.1 Motivation and Relevance

The upper troposphere/lower stratosphere is a region of the atmosphere with a highly complex chemical and dynamical vertical structure that is governed by a variety of processes such as convection, lightning, biomass burning, aircraft exhaust and exchange between troposphere and stratosphere (Ungermann et al., 2022; Holton et al., 1995). Small variations of greenhouse gases such as water vapor (H_2O) and ozone (O_3), aerosols and high cirrus clouds have significant effects on radiation balance and thus to the surface climate (Riese et al., 2014; Ungermann et al., 2022). This atmospheric region has been sounded by several remote sensing instruments for decades. In the last 14 years, the GLORIA spectrometer offered 2-D cross sections and 3-D tomographic retrievals of atmospheric volumes at high spatial, temporal and spectral resolution (Friedl-Vallon et al., 2014). After more than 600 flight hours and ten successful campaigns with GLORIA, its successor-to-be GLORIA-Lite (GLite) had its first flight in Summer 2024 (Ungermann et al., 2022; Friedl-Vallon, 2025). GLite is a newly developed advanced limb sounding imaging Fourier transform spectrometer, that is significantly lighter, smaller, and more cost-effective due to the use of state-of-the-art detectors, miniaturized electronics and an innovative optical design (Friedl-Vallon, 2025).

Retrieving information from measurements of the weak thermal emission lines of the atmospheric components requires a well-designed, calibrated, and characterized instrument. A part of this process is the characterization of stray light. Stray light is by definition unwanted light that reaches the focal plane of an optical system (Fest, 2013). The thermal infrared in which GLite operates is a spectral region, where every photon counts due to the weak thermal emission of the atmospheric substances. Additional unwanted stray photons may occupy a significant part of the dynamic range of the detector and thus reduce the sensitivity of the measurements. If stray light hits the detector, this also may lead to distortions or errors of the measured spectra. These errors depend on the spectral and spatial intensity distribution of the incoming radiation and may cause error patterns within the retrieved data. These patterns can be misinterpreted as high concentrations or even plumes of atmospheric substances (Huhs et al., 2025). The errors caused by stray light can be corrected either during data processing or by altering the optical design of the instrument, whereby the latter is preferable. Both solutions are possible only if a comprehensive understanding of the stray light effects, their magnitude, and causes is provided.

1.2 Objectives

This thesis aims to characterise the stray light present in the optical system of GLORIA-Lite. Therefore, a comprehensive description of the occurring effects and their magnitude is necessary. This allows to identify the main stray light effects that are expected to have the most influence onto measurement quality. For these main effects, an analysis of the stray light paths provides deeper understanding of the mechanisms causing the stray light. Based on this knowledge, suggestions for stray light mitigation are developed. For effects that are difficult to mitigate, this thesis aims to provide sufficient knowledge to enable their consideration within operational data processing.

1.3 Thesis structure

This thesis is structured as follows: First in Chapter 2 background information about the topic of stray light, its effects, characterization methods and mitigation strategies is given. Second, an overview of the measurement principle and development of GLORIA-Lite is provided. This is followed by a detailed description of the instrument. Following in Chapter 4, the flight measurement campaign and the laboratory measurements are presented. There, also the used processing algorithms are described. After that, the results from the flight measurements in Chapter 5 and from the lab measurements in Chapter 6 are presented. In Chapter 7 the results previously presented are discussed and compared to each other and to theory. Lastly, in Chapter 8 conclusions, recommendations for future improvement of the instrument design, and an outlook is provided.

2 Theoretical Background

2.1 Stray Light in optical systems

Stray light is defined as unwanted light that reaches the focal plane of an optical system (Fest, 2013). Stray light takes paths that do not follow the desired and designed optical path in the instrument. The main mechanisms are reflection, refraction, diffraction, and scattering at optical components, surfaces, edges, and other parts of the surrounding instrument.
These mechanisms can be separated into two categories: specular or scatter. The stray light generated by specular mechanisms is deterministic and follows Snell's laws or the grating equation, while light generated by scatter mechanisms does not follow these laws and is not deterministic.
Another categorisation for stray light is the position of the source. If the source of the stray light is located within the FOV, it is categorized as in-field stray light. If the source is outside of the FOV it is called out-of-field or outfield stray light.
Stray light can also be categorized by the order of the stray light path, which is the number of stray light mechanisms mentioned above that occur on the path. Non-stray-light events are not counted when the order of the path is determined. An example of a zero-order path would be light hitting the focal plane directly without any other optical mechanisms, a so-called "sneak" path. A ghost reflection as in Figure 2.1 is a second-order stray light path as there are two reflections that occur.
The mentioned stray light processes can happen only at objects that are reached by light. Objects reached by outside light are called illuminated. However, an illuminated object generating stray light is not enough to see the effects on the detector. The generated stray light has to make its way onto the detector, so the object has to be "seen" by the detector. Objects that can be seen by the detector are termed critical. Any component of the designed optical path, e.g. lenses, mirrors, or windows, are critical by definition. However, parts of the instrument housing and mountings of optical components may also be seen by the detector.
To actually detect stray light effects in the optical system, the object that generates stray light must be illuminated and critical (Fest, 2013).

2.2 Typical stray light effects

This section provides a brief overview of various stray light effects. All of them are common effects that can occur in infrared optical systems as GLite.

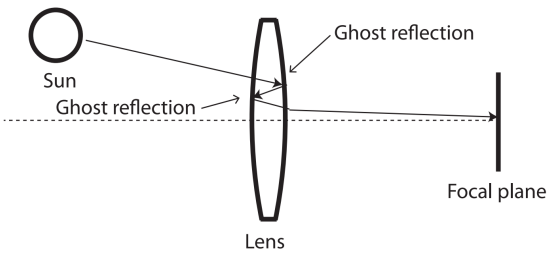

Figure 2.1: Example of a Ghost reflection as second order stray light path. Figure from (Fest, 2013).

2.2.1 Ghost reflections

Ghost reflections are a common specular stray light effect that will occur in any optical system with at least one refractive element. Ghost reflections are caused by multiple reflections at the interfaces between materials of different refractive indices. An example for a ghost reflection within a lens is shown in Figure 2.1. The ghost reflections result in bright spots that usually occur if the radiation source is within the FOV or at least close to it. The path transmittance τ_p depends on the number of reflections n and the reflectance ρ_i of each surface at which a reflection occurs:

$$\rho_p \propto \prod_{i=1}^{n} \rho_i \tag{2.1}$$

The values of ρ_i are usually small, so small variations can significantly change the path transmittance. As the path transmittance decreases further with each additional reflection, paths with a small number of reflections, usually two, are most likely to observe. The number of possible 2^{nd} order ghost reflections paths N is given by:

$$N = \frac{1}{2}(n^2 - n) \tag{2.2}$$

where n is the number of refractive surfaces. This equations shows that the number of ghost reflection paths with two reflections increases roughly quadratically with the number of refractive surfaces. This leads to a general rule of optical design: To improve stray light performance, the number of refractive elements should be as small as possible. It is important to notice that multi-reflection paths commonly are called ghosts, even if they do not originate from reflections in refractive elements as defined here. In this case the therm ghost describes a broader field of effects that cause artifacts similar to those from refractive ghost reflections (Murray, 1949; Fest, 2013).

2.2.2 Narcissus reflections

Narcissus reflections are a type of stray light that is also caused by reflections but occurs only in infrared systems. In high-sensitivity and high-speed infrared optical systems, the detector is usually cooled and thus much colder than the surrounding instrument. Through unintended optical paths, the detector can see a reflection of its own surface that is colder than the other surrounding surfaces. In the detected image the narcissus reflection can be seen as a colder area with sharp edges.

In optical systems with focal plane arrays, the narcissus is removed during the calibration process as it is considered as part of the background and then subtracted. However, changes in the temperature of the instrument housing would make the narcissus reflection visible again. This requires recalibration in regular intervals if the ambient temperature changes (Fest, 2013; Scherr et al., 1996; Lau, 1977).

2.2.3 Aperture diffraction

Aperture diffraction is the most common diffraction effect in optical systems. Following diffraction theory, the entrance aperture leads to a diffraction pattern at the focal plane array detector. The diffraction pattern is mainly determined by the focal length and the shape and size of the aperture. The irradiance at the image plane $E_f(u,v)$ is also called point spread function (PSF) and is given as:

$$E_f(u,v) = \frac{1}{\lambda^2 f^2} \mid \mathfrak{F}[t_A(x,y)] \mid^2 \tag{2.3}$$

where f is the focal plane, $\mathfrak{F}$ the Fourier transform and t_A the pupil transmittance function. In general t_A is a complex function that describes the intensity transmittance and wavefront error of the pupil. The PSF of a circular aperture of diameter D is given as:

$$E_f(r) = \left(\frac{\pi D^2}{4\lambda f}\right)^2 \left[2\frac{J_1(\pi Dr/\lambda f)}{\pi Dr/\lambda f}\right] \tag{2.4}$$

where $r = \sqrt{u^2+v^2}$ and J_1 is the Bessel function. The intensity distribution for a pupil of 1 mm is shown in Figure 2.2 while the influence of the shape of the aperture onto the diffraction pattern is shown in Figure 2.3.
If the angle of the incident beam is much greater than the angle of the airy disk $(1.22\lambda/D)$ or if the diffraction angle is quite large, the PST becomes difficult to calculate. In this case it is easier to model the aperture diffraction as a scattering phenomenon by using the bidirectional diffraction distribution function (BDDF). For a circular aperture, the BDDF results from normalizing the far-field diffraction pattern of the aperture with the irradiance incident on it:

$$BDDF = \frac{D^2}{\lambda^2}\left[\frac{\pi J_1(\pi D \mid sin\theta_d - sin\theta_i \mid /\lambda)}{\pi D \mid sin\theta_d - sin\theta_i \mid /\lambda}\right]^2 \tag{2.5}$$

The corresponding geometry is shown in Figure 2.4. This BDDF can be treated as any other BDSF as described in Section 2.2.4. In this way, the aperture diffraction can be modelled by a first-order stray light model instead of performing computationally intensive Fourier transforms. Due to the Bessel function, the BDDF oscillates at high frequency with $\mid sin\theta_d - sin\theta_i \mid$. These oscillations are usually not observable as the measurements average over detector pixel area and wavelength. In this case it is easier to use the asymptotic form:

$$BDDF = \frac{\lambda}{\pi^3 D \mid sin\theta_d - sin\theta_i \mid^3} \tag{2.6}$$

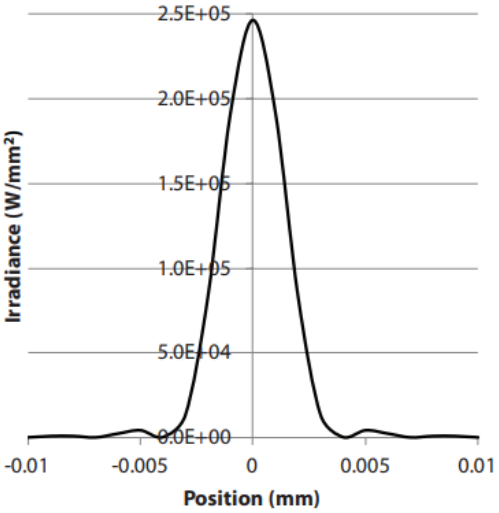

Figure 2.2: Intensity distribution of a circular aperture with 2 mm and a focal length of the system of 10 mm. The aperture is illuminated with a collimated beam of wavelength 0.6328 µm and irradiance $1\,\mathrm{W/mm^2}$. Figure from (Fest, 2013)

As this function has a quite steep slope, which indicates that diffraction can be the dominant stray light mechanism close to the specular beam but usually not at large incident angles (Fest, 2013).

2.2.4 Scattering

Scattering in optical systems is a broad topic covering scattering from rough surfaces, surface coatings, particle contamination, or surface damage like scratches and digs. As the description and modelling of scattering is a complex and wide field, only a brief overview is given here. Scattering is a non-specular stray light mechanism and depends strongly on the microscopic properties of the surface that is involved in the process. An example for scattering from a rough surface is shown in Figure 2.5. The surface roughness determines magnitude and angular distribution of the scattered light. As the roughness is determined by the actual manufacturing process of the surface, modelling of its properties is rather difficult and thus most descriptions of the roughness and its scattering behaviour rely on measurement data.

A common way to describe scattering properties of a surface is the bidirectional scattering distribution function (BSDF). It is the differential radiance dL of a scattering surface, normalized by the differential irradiance dE incident on the surface:

$$BSDF(\theta_i, \phi_i, \theta_s, \phi_s) = \frac{dL(\theta_i, \phi_i, \theta_s, \phi_s)}{dE(\theta_i, \phi_i)} \tag{2.7}$$

where θ_i and ϕ_i are elevation and azimuth angle of the incident ray while θ_s and ϕ_i are the corresponding angles for the scattered ray. Figure 2.6 is a schematic drawing of the mentioned angles and the incident and scattered beams. The unit of the BSDF is $\frac{1}{sr}$, for real surfaces the BSDF

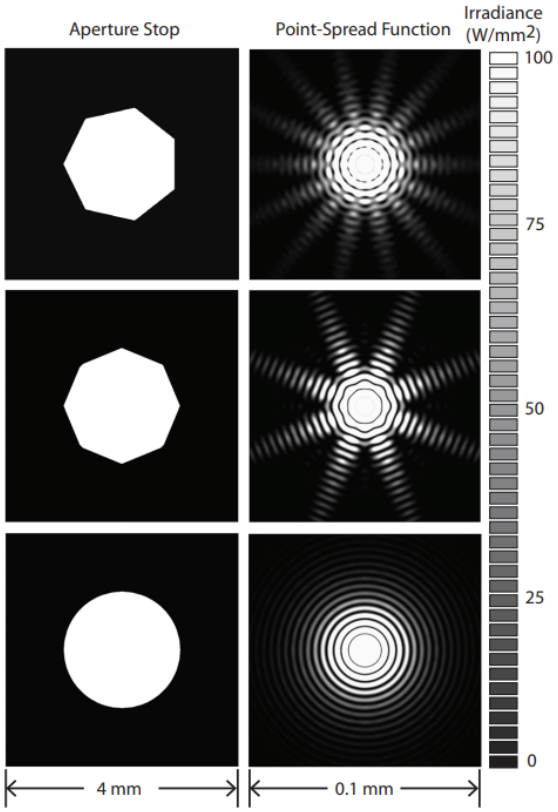

Figure 2.3: Different aperture shapes on the left and their resulting far-field diffraction pattern on the right side. The illumination is similar to Figure 2.2. Figure from (Fest, 2013).

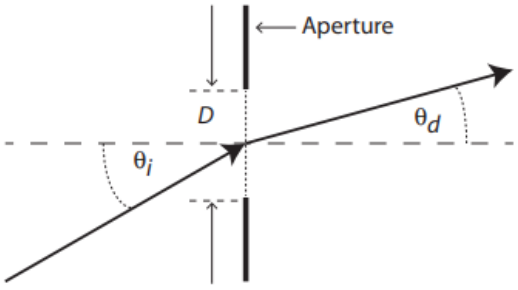

Figure 2.4: Geometry and quantities as used in the definition of the BDDF. Figure from (Fest, 2013).

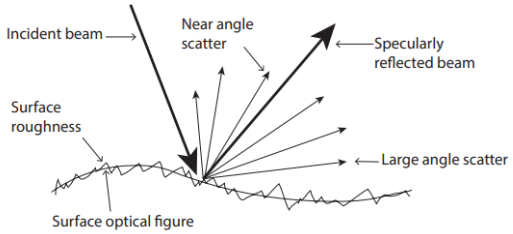

Figure 2.5: Scattering from surface roughness. Figure from (Fest, 2013).

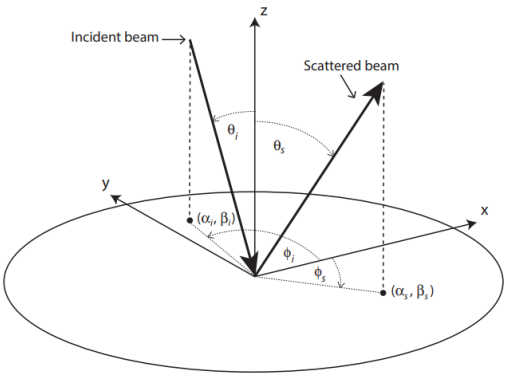

Figure 2.6: Geometry and angles used for the BSDF definition. Figure from (Fest, 2013).

is always greater than zero and can be greater than one. From conservation of energy follows that the BDSF has to be the same if incident and scattered rays are reversed:

$$BSDF(\theta_i, \phi_i, \theta_s, \phi_s) = BSDF(\theta_s, \phi_s, \theta_i, \phi_i) \tag{2.8}$$

If the BSDF of a surface at normal irradiance only varies with θ_s the surface is called isotropic scatterer while surfaces with a BSDF that also varies with ϕ_s are called anisotropic scatterers.
The BSDF describes the amount of light an object scatters from a specific direction into a specific direction. In general, the BDSF is a function of incident and scatter angles, wavelength, and position and is usually determined by measurements (Fest, 2013).

2.3 Effects on measurement accuracy

Stray light can affect the measurement accuracy of an infrared Fourier imaging spectrometer in several ways. At first, stray light will increase radiative noise as simply more photons hit the detector. In addition, it can reduce the contrast and resolution of the image (Wei et al., 2022). From an interferometric point of view, stray light that is generated inside the interferometer by reflective processes can cause aliasing. This will decrease interference fringe contrast and affect the capability of spectrum recovery (Ben et al., 2024).
The main issue is, that the final products generated from the measurements are also affected by stray light. Due to the stray light, spectral information from other angles of incidence are mixed with the true information. This changes the vertical distribution of radiance and specific spectral

lines. Thus error patterns are brought into the vertical profiles. These error patterns caused can be misinterpreted as enhanced concentrations of trace gases or even plumes in a few cases (Huhs et al., 2025).

2.4 Straylight characterization methods

2.4.1 Point Source Transmittance (PST)

The point source transmittance (PST) is a transfer function that describes the amount of stray light in an optical system. It is the ratio of stray light at the focal plane divided by the amount of light at the entrance aperture. Depending on the definition, the PST is the ratio of fluxes or the ratio of irradiances. Using the latter possibility, the PST is as follows:

$$PST = \frac{E_{SL}}{E_i} \tag{2.9}$$

Here, E_{SL} is the irradiance at the focal plane caused by stray light and E_i the irradiance at the entrance aperture plane. Usually, the PST varies with the angle between the stray light source and the optical axis. The irradiance E_{SL} can be defined as the irradiance averaged across the entire detector or as average over a smaller sub-region (Fest, 2013).

2.4.2 Collimated source test

A common method to measure the PST is the collimated source test. It measures the amount of stray light on the focal plane from a point-like or sun-like source. The source is placed in the focus of a collimator to illuminate the optical system with parallel rays. The system itself is placed on a rotating table to measure incoming radiation from different off-axis angles θ. The schematic drawing of a typical setup is shown in Figure 2.7. The chopper modulates the radiation emitted by the source to make it distinguishable from other radiation. Especially in the infrared, this is important to separate the source from the thermal radiation of the surroundings. The lock-in amplifier connected to the detector and chopper amplifies only the measured signal at the chopper frequency. It acts as a very narrow bandpass filter and thus increases the signal-to-noise ratio (SNR). To be detectable, the stray light irradiance has to be greater than the detector noise (Fest, 2013).

2.4.3 Detector field of view

The detector field of view (Detector FOV) is a transfer function commonly used in stray light analysis software. There, the light is propagated backwards from an extended source at the detector through the optical system. That leads to intensity I as a function of azimuth (θ) and elevation ϕ (Fest, 2013).

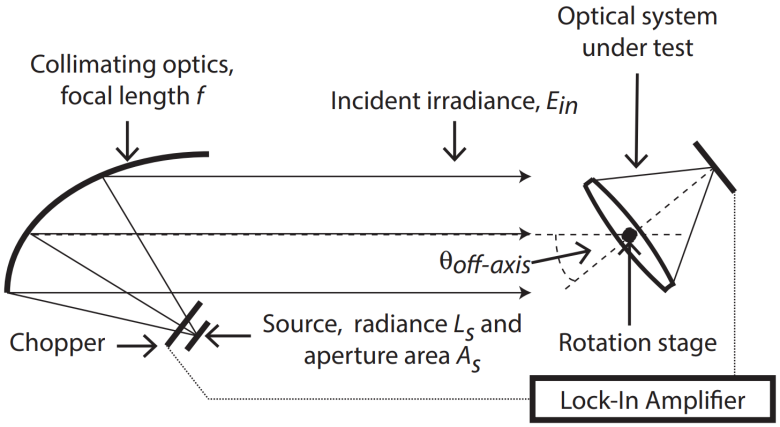

Figure 2.7: Schematic diagram of a collimated source test with Lock-in Amplifier and optical system on a rotating stage. Figure from (Fest, 2013).

2.5 Straylight mitigation

The main goal of the previously described methods and measures is to identify stray light and in the end, to alter the optical design to reduce it. The possibilities of minimizing stray light can be summarized by the following phrase:**"Move it or block it or paint/coat it or clean it"**.

- "Move it" simply means to move an object that causes stray light so that it is not illuminated or critical any more.
- "Block it" refers to blocking the stray light path at some point, usually by inserting a baffle or stop. This also prevents the object that causes stray light from being critical or illuminated.
- "Paint/coat it" refers to painting some surfaces black to reduce reflection and scattering. Coating can also smoothen surfaces to reduce scatter, or in the case of anti-reflective coatings, to reduce the reflectance of transmissive elements such as lenses.
- "Clean it" refers to reducing particle contamination on surfaces to reduce scatter.

These strategies range from changes in optical design to simpler operational solutions, depending on the cause of the stray light and the technical possibilities (Fest, 2013).

3 GLORIA Lite

GLORIA-Lite (GLite) is a new Imaging Fourier Transform Spectrometer (IFTS) developed by IMKASF at KIT and FZ Jülich. It measures infrared radiation emitted by atmospheric components in the limb sounding geometry. The goal is to retrieve trace gas concentrations and temperature with high spatial resolution by using a light, small, and versatile device. The first version of GLite had its first flight in June 2024 and showed proof of concept.

3.1 Measurement principle

3.1.1 Michelson Interferometer

The core of the GLite spectrometer is a Michelson Interferometer. The following section focuses on a general description of the interferometer without considering the special design of GLite. The basic form of a Michelson interferometer is shown in Figure 3.1. It has one fixed mirror, one moving mirror, and a beam splitter (BS). The interferometer consists of two arms. A light beam from a source in arm one is split by the BS into two light beams of equal amplitude if the BS is assumed to be ideal. One beam is reflected at the fixed mirror back to the BS and travels the path length s_1. The other beam is reflected at the moving mirror back to the BS and travels the variable path length $s_2(x)$. At the BS both beams recombine and are reflected/transmitted towards the detector and the source.
The difference between both path lengths is the optical path difference: $OPD(x) = s_1 - s_2(x)$. If $s_1 = s_2$ the OPD is zero, this mirror position is called zero optical path difference (ZOPD). For the detector path, maximum intensity is measured if both beams interfere constructively at ZOPD. Constructive interference occurs at all OPDs when both beams meet in phase: $OPD = n\lambda$ where λ is the wavelength of the light and $n = 0, 1, 2, 3, 4, \ldots$.
At destructive interference, the intensity reaches its minimum at the detector. In the ideal case, there would be no signal, as the two beams meet exactly out of phase. In this case $OPD = (n + \frac{1}{2})\lambda$, with λ and n as above.
For a monochromatic source of wavelength λ_0 (and wavenumber σ_0) with intensity $S(\sigma_0)$ the intensity as a function of the optical path difference x is given as:

$$I_0(x) = S(\sigma_0)(1 + cos(\frac{2\pi x}{\lambda_0})) \tag{3.1}$$

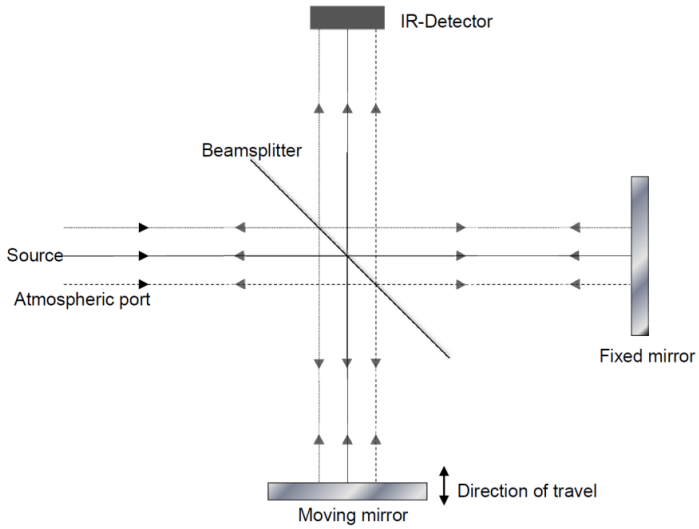

Figure 3.1: Scheme of a Michelson interferometer as it is used in FTS. Figure from (Sha, 2013).

The intensity contains an unmodulated term and an OPD-dependent modulated term. For polychromatic radiation, the detector measures a superposition of the modulated terms:

$$I_1(x) = \int_0^\infty S(\sigma)(1 + cos(2\pi\sigma x))d\sigma \tag{3.2}$$

By subtracting the mean of I_1 the modulated part is given as:

$$I(x) = I_1(x) - \overline{I_1(x)} = \int_0^\infty S(\sigma)cos(2\pi\sigma x)d\sigma \tag{3.3}$$

A complete interferogram is taken as the mirror moves along its axis. The interferogram has its maximum intensity at ZOPD as all wavelengths of light interfere constructively. The farther away the mirror moves from the ZOPD position, the more the interferogram intensity decreases, as more different wavelengths are out of phase. The interferogram contains all the spectral information of the incoming radiation $S(\sigma)$.

3.1.2 Fourier Transformation

Equation 3.3 is the positive part of the cosine transformation. By extending the integration range from $-\infty$ to $+\infty$ the spectrum of negative wavenumbers $S(-\sigma)$ is also produced. The actual signal is real and symmetric to ZOPD, so $S(-\sigma)$ is the complex conjugate $S^*(\sigma)$. In this case, the cosine transformation in 3.3 can be expressed as a complex Fourier transformation:

$$I(x) = \int_{-\infty}^\infty S(\sigma)e^{i2\pi\sigma x}d\sigma \tag{3.4}$$

So, the interferogram is the Fourier transform of the spectrum of the measured radiation. The spectral information contained in the interferogram can be obtained by performing the inverse Fourier transformation:

$$S(\sigma) = \int_{-\infty}^{\infty} I(x) e^{-i2\pi\sigma x} dx \tag{3.5}$$

This process of obtaining spectral information from an interferogram by inverse Fourier transformation is the core of all Fourier transform spectrometers.

3.1.3 The measured interferogram

Compared to the previously discussed case of an ideal interferogram, the measured interferogram differs in some points: The real interferogram does not extend into infinity, but has a limited number of sampling points. This also brings up the second difference: The interferogram is not continuous, it is discrete with values only at the sampled points. In addition, the sampling points may be distributed in a way that the maximum of the interferogram at ZOPD might not be hit.
The discrete sampling points of the interferogram leads to a limited maximum wavenumber σ_{max} in the transformed spectrum. This follows from the Nyquist Theorem as shown in Sha, 2013.
The maximum wavenumber is:

$$\sigma_{max} = \frac{1}{2\Delta x} \tag{3.6}$$

Here, Δx is the distance between two sampling points on the OPD-axis.
As the Fourier transformation of the discrete interferogram is also calculated at discrete points, the obtained spectrum is also discrete. This leads to a spectral sampling given as

$$\delta\sigma = \frac{1}{2L} = \frac{1}{N\Delta x} \tag{3.7}$$

where $2L$ is the length of the interferogram with N sampling points with a sampling interval of Δx. The finite length $2L$ of the interferogram leads to a broadening of the spectral lines. This happens because the ideal infinite interferogram is convoluted with a rectangular function of width $2L$. In the spectral space this equals the convolution of the ideal spectrum with a sinc function of with $1/(2L)$. An infinitely small line is broadened to a finite width. This width can be expressed as full width at half maximum (FWHM):

$$FWHM = 1.207 \frac{1}{2L} \tag{3.8}$$

This equation shows that a longer interferogram will produce less broadened spectral lines (Sha, 2013).

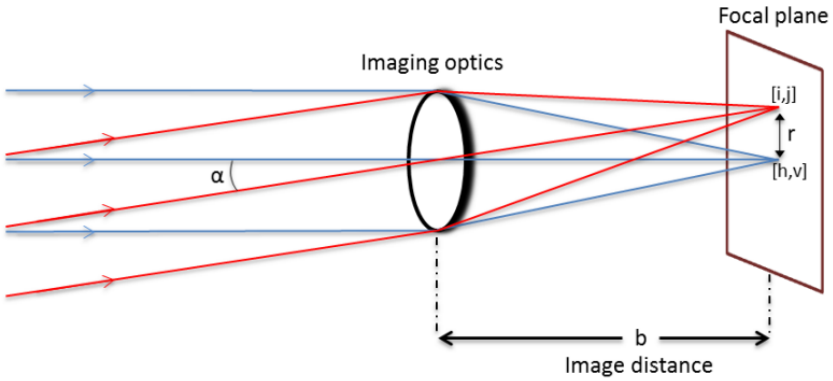

Figure 3.2: Schematic drawing of the imaging principle. The parallel blue on-axis beams are projected onto the on-axis pixel [h,v] while the red beams incident under angle α are projected to an off-axis pixel[i,j]. Figure from (Sha, 2013)

3.1.4 Imaging FTS

GLite is an imaging FTS that uses an array detector. The radiation goes through an imaging optic before it hits the array detector, which is placed in the focal plane of the optic. A scheme of such an imaging optic is shown in Figure 3.2. In that configuration, parallel rays incident along the optical axis hit the on axis pixel $[h, v]$ while radiation incident under a given angle α hits a correspondig off-axis pixel $[i, j]$. In that way, the imaging FTS is capable of measuring multiple interferograms from different directions within its FOV at the same time. Basically, it takes a spectral image of the atmosphere, making it possible to measure concentrations of atmospheric components at very high vertical and horizontal resolution. In that way, 3D chemical structures and atmospheric dynamics of the middle atmosphere become visible (Friedl-Vallon et al., 2014).
The principle of an imaging FTS also affects the straylight behaviour. Due to the bigger FOV compared to a scanning instrument, the sensitivity for infield stray light is bigger. This also makes baffling within the instrument more difficult.

3.1.5 Limb Measurements

GLite measures in the limb sounding geometry. In this geometry, observations are taken along paths through the atmosphere. These paths are tangents to a layer parallel to the earths surface. The tangent point is the position where the line of sight is deepest in the atmosphere. Its height above the geoid is called the tangent altitude. A schematic representation of the limb geometry is shown in Figure 3.3. All atmospheric layers along the line of sight contribute to the signal, while the main part of the signal comes from the tangent point, as this is the most dense part of the atmosphere with the longest path in it. As the line of sight passes through the atmosphere into space, to spectroscopic methods are possible: By using the sun as background, absorption spectroscopy of the atmosphere can be done. There, atmospheric substances absorb radiation from the sun leading to an absorption spectrum. The absorption spectrum is basically the spectrum of the sun subtracted by the specific absorption lines of the atmospheric substances. This method provides a good signal-to-noise ratio

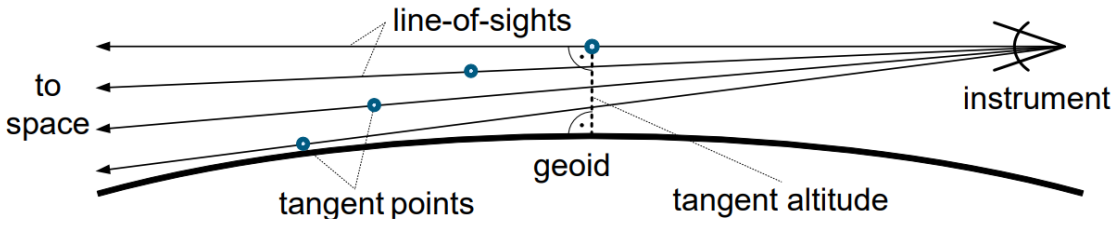

Figure 3.3: Schematic representation of the limb measurement geometry showing the different lines of sight and their tangent points. Figure from (Ungermann et al., 2013).

(SNR). On the other hand, spatial and temporal freedom of the measurements are limited by the sun's occultation.

When using the cold deep space as background emission spectroscopy is performed. There, only the thermal emission of the atmospheric substances. The emission spectrum consists only of the emission lines of the corresponding substances. The relation between absorption and emission spectra is shown in Figure 3.4. This method gives a great temporal and spatial freedom for the measurements, but has a low signal-to-noise ratio and requires a sensitive and well-designed instrument because the received radiation is weak. In general, limb measurements have an excellent vertical resolution, while the horizontal resolution is limited due to the long paths through the atmosphere along which the signal is averaged. Additionally, movement of the instrument during one measurement leads to horizontal averaging of the air masses that are swept during that time period (Johansson, 2019).

The special limb sounding geometry also affects the stray light within the instrument. The upper atmosphere emits few radiation, while the lower atmosphere and the earth are strong radiance sources. This strong vertical gradient of the scene also affects the weight, stray light from a given direction has. Stray light that mixes radiation from lower elevations upwards has a very strong effect, while stray light that mixes radiation downwards has less to almost no effect. Depending on the direction of the line of sight, the sun can also be close to the FOV.

3.2 Heritage

Fourier transform spectroscopy has been in use for atmospheric observations since the mid/late 1960s (Poli and Brunel, 2016). At KIT, GLORIA-Lite is the newest development in a long line of successful infrared Fourier transform spectrometers, beginning with MIPAS (Michelson interferometer for passive atmospheric sounding) in its balloon (MIPAS-B2), aircraft (MIPAS-STR), and satellite version on ENVISAT. MIPAS was still a scanning instrument, while its successor GLORIA (Gimballed Limb Observer for Radiance Imaging of the Atmosphere) is the first imaging FTS. The GLORIA-AB aircraft version is operational since 2011, followed by the GLORIA-B balloon version with its first flight in 2021 (Friedl-Vallon, 2025).

An illustration of GLORIA-AB is shown in Figure 3.5. The instrument is designed to operate on the high-altitude research aircrafts HALO and Geophysica, thus the spectrometer is gimbal-mounted to keep its line of sight (LOS) stable. This also allows to perform tomographic measurements, where a

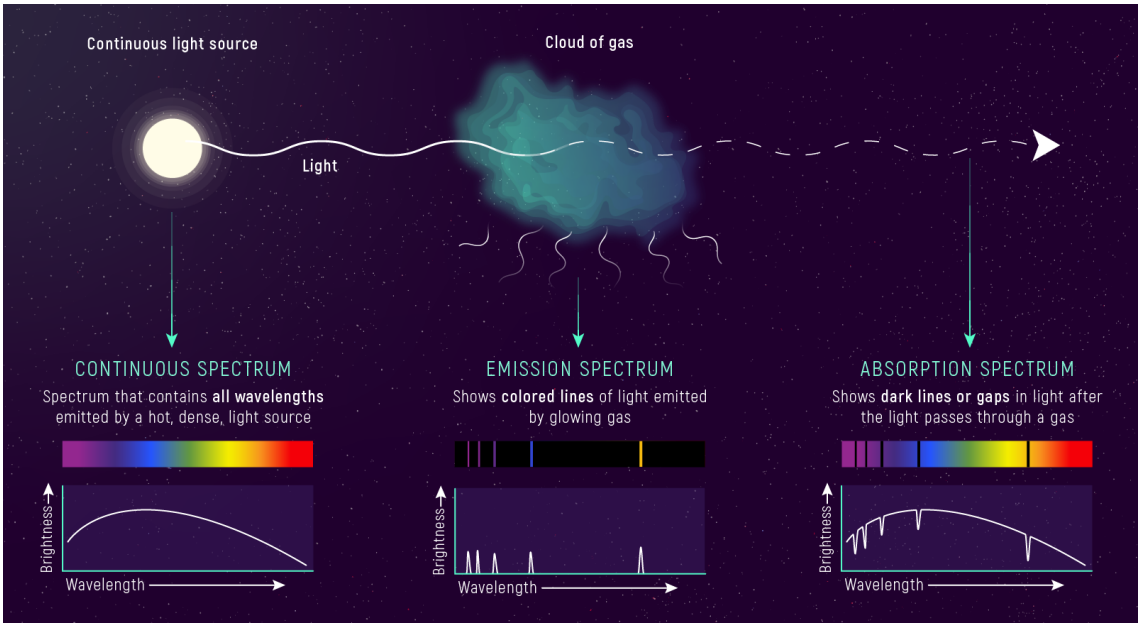

Figure 3.4: Scheme of the relation between the continuous solar spectrum and the absorption spectrum as measured by using the sun as background and the emission spectrum that can be measured when using the cold space as background for limb sounding. Figure from (NASA;ESA; CSA; Leah Hustak, 2021).

volume of air is measured from different viewing directions to increase horizontal spatial resolution. The interferometer itself is quite similar to Figure 3.1, apart from the mirrors. GLORIA uses two three-sided corner cubes instead of plain mirrors. The interferometer unit is cooled by dry ice to a temperature of $200 - 220\,\mathrm{K}$ to reduce self emission and thus improve sensitivity. The instrument can be operated at two different modes depending on whether a high spectral resolution (chemistry mode) or a high temporal resolution (dynamics mode) is necessary. In dynamics mode, the travel distance of the moving mirror is reduced. This reduces the time per measurement, but the OPD and the spectral resolution are also reduced, as shown in Equation 3.7.

A more detailed description of GLORIA, its internal setup and operations is omitted here, as this work focuses on GLORIA-Lite, which differs in its internal structure.

The following properties and specifications of GLORIA act as a reference for the development of GLORIA-Lite: Table 3.1 shows the basic properties of the entire assembly as mounted on the aircraft, Table 3.2 gives an overview of the optical and spectroscopic properties while detector properties are given in Table 3.3.

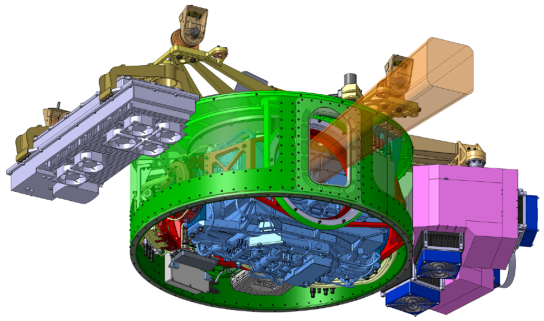

Figure 3.5: Schematic diagram of the GLORIA instrument. The interferometer is colored blue, while the gimbal frames are coloured green and red. The transparent orange bar is the field of view. On the left side is the power supply unit. On the right side the two calibration blackbodies are mounted. Figure from (Friedl-Vallon et al., 2014).

Property	Value
Total Mass	240 kg
Mass of instrument	212 kg
Mass of control computer	28 kg
Overall length	1610 mm
Overall width	975 mm
Overall height	675 mm
Typical power consumption	ca. 800 W
Typical raw data rate	600 Mbit/s

Table 3.1: Basic instrument properties of GLORIA. Data from (Friedl-Vallon et al., 2014).

Property	Value
Entrance window diameter	100 mm
Focal length of infrared objective	72.2 mm at 218 K
Vertical spatial sampling	140 m
Horizontal spatial coverage	6.7 km
Spectral Coverage	$780 - 1400\,\mathrm{cm}^{-1}$
OPD	(8.0/0.8)cm
Spectral sampling	$(0.0625/0.625)\,\mathrm{cm}^{-1}$
Temporal sampling	(13.5/2.5)s

Table 3.2: Optical and spectrometric properties of GLORIA. Values in brackets refer to (chemistry/dynamics) mode. Vertical sampling and horizontal coverage refer to a observer altitude of 15 km and a tangent altitude of 10 km. Data from (Friedl-Vallon et al., 2014; Ungermann et al., 2022).

Property	Value
Detector Type	256^2 HgCdTe-LFPA
Manufacturer	AIM Infrarotmodule GmbH
Detector array and full frame readout frequency	256×256 pixels with 884 Hz
Used array and readout frequency	128×128 pixels with 2665 Hz 64×128 pixels with 4940 Hz 48×128 pixels with 6281 Hz
Pixel pitch	40 µm
Full well capacity of pixel	23.26 Me^-
Operation temperature	50 K

Table 3.3: Detector properties of GLORIA. Data from (Sha, 2013; Friedl-Vallon et al., 2014).

3.3 Development goals

The main development goal of GLORIA-Lite is to design a smaller, lighter, and less complex instrument compared to its predecessor, GLORIA.
In terms of weight and size, the design aims at a weight of around 20 kg and a space requirement of about 20 L. This allows GLite to be operated on a wider range of carriers such as stratospheric balloons and research aircraft, e.g. HALO. In the future operation on long-duration balloons and CubeSat's will also be possible. The reduction of complexity makes the instrument easier to operate and should make it simpler to adapt the instrument to different scientific tasks, spectral ranges, and carriers, as mentioned above (Friedl-Vallon, 2025). On the other hand, there is a financial advantage: In aviation, most of the payload costs are weight-driven, and thus a lighter instrument is likely to cause fewer costs.
The central design decisions to achieve these goals are described here. To make the instrument substantially smaller, the maximum OPD is reduced to 2.5 cm. That also results in a smaller spectral resolution, which was accepted by scientific users. To further reduce the system size, a smaller throughput is chosen. In order to reduce operational effort and technical complexity, active cooling is not used in GLite. To deal with the challenges that arise from this decision, the core parts of the instrument are designed in a quasi-monolithic way, so the instrument is athermal and does not respond to temperature changes (Friedl-Vallon, 2025; Schwab, 2021). The technical design in detail is described in the following section.

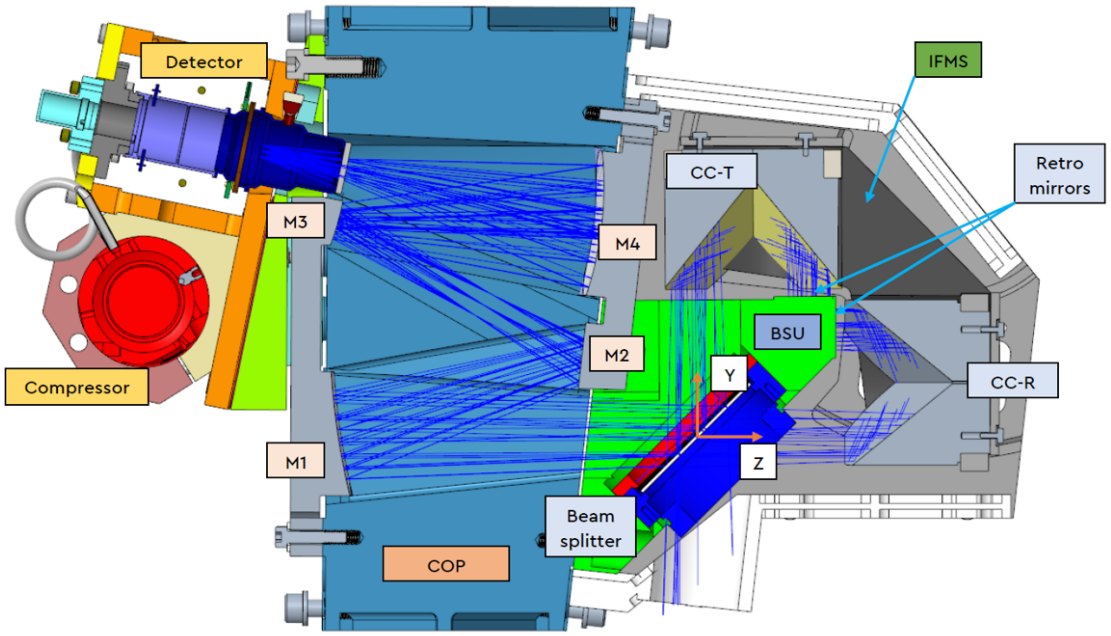

Figure 3.6: Schematic drawing of the GLORIA-Lite spectrometer with the interferometer structure, the camera optics and the detector module shown. The pointing optic module is not shown and would be on the lower right side. Figure from (Schwab, 2021).

Property	Value
Total Mass	34.27 kg
Mass of instrument	27.97 kg
Mass of electronics	6.3 kg
GLite length	550 mm
GLite width	450 mm
GLite height	300 mm

Table 3.4: Basic instrument properties of GLite. The masses refer to the setup used during the first flight. The dimensions only apply to the instrument itself, as the electronics have two external housings, that could be placed anywhere. A version that integrates the electronics into the instrument housing is under development. Data from (Kretschmer, 2024; Friedl-Vallon, 2023).

3.4 Mechanical and Optical Design

The instrument consists of four separate modules, each serving one single purpose. Along the optical path, first, there is the pointing optic module (POM) that controls and stabilizes the elevation angle of the line of sight (LOS). Second there is the core of the instrument, the interferometer structure (IFMS), which contains the Michelson interferometer with its mirrors and the beamsplitter unit (BSU). It is followed by the third module, the camera optics (COP) that focuses the beam via four mirrors to the fourth module, the detector unit. The units, their technical design and their properties are described in the following sections. A schematic drawing of the current version of GLite is shown in Figure 3.6. The basic properties of GLite are shown in Table 3.4, while the main optical and spectrometric properties are provided in Table 3.5.

3.4.1 Pointing Optic Module

The POM controls the elevation angle of the LOS by rotating a 45° scanning mirror around one axis. The POM has two tasks: First, set the LOS to the selected target and second, to stabilize the LOS during atmospheric measurements. The possible targets and according elevation angles for the LOS are:

- Atmosphere during limb view measurements $(-6^\circ$ to $4^\circ)$
- Atmosphere during nadir measurements (-90°)
- Calibration blackbody above the POM (90°)
- Deep Space calibration measurement (20°)

Depending on the actual measurement mode, the LOS has to be stabilized relative to a given tangent altitude, elevation angle, or a target point on ground. To achieve this, the POM has to compensate for pitching movements and altitude changes of the instrument platform. The POM includes the iNAT-M200/TLE-DA navigation system by iMAR Navigation GmbH, which provides position, velocity, attitude, and acceleration data based on inertial measurements and dual GPS (iMAR Navigation GmbH, 2022; Kretschmer, 2023a). The overall achieved elevation stability is better than 2 mrad.
A scheme of the POM is shown in Figure 3.7. The mirror is surrounded by a rotating baffle that prevents radiation from entering through any port except the one that is in use. In addition, it protects the inside of the instrument from dust when closed.
As the scanning mirror is mounted at 45°, the image is rotated to the according to the elevation angle of the mirror. That rotation is not compensated anywhere during the measurement process. It has to be compensated later in the data processing, if considered necessary (Kretschmer, 2023b).

3.4.2 Interferometer Structure

General design

In Figure 3.6 the interferometer structure is the gray coloured structure on the right side. The michelson interferometer in this case is a bit more complicated that the one shown in Figure 3.1. Instead of a common michelson interferometer with one linear moving mirror, the interferometer is designed as double pendulum interferometer where both corner cube reflectors are moving. Both corner cubes are mounted together onto the modulator carriage, which moves the mirrors on a section of a circular path. In this case, the optical path lengths in each arm are dependent on the mirror position. As one path length decreases, the other increases, thus the gained OPD per physical mirror movement is twice as big. To increase that factor even more, the light is not reflected directly to the beam splitter, but is reflected towards two plane retroreflectors placed on the sides of the beam splitter unit (BSU). They reflect the radiation back to the cube corners and from there, the

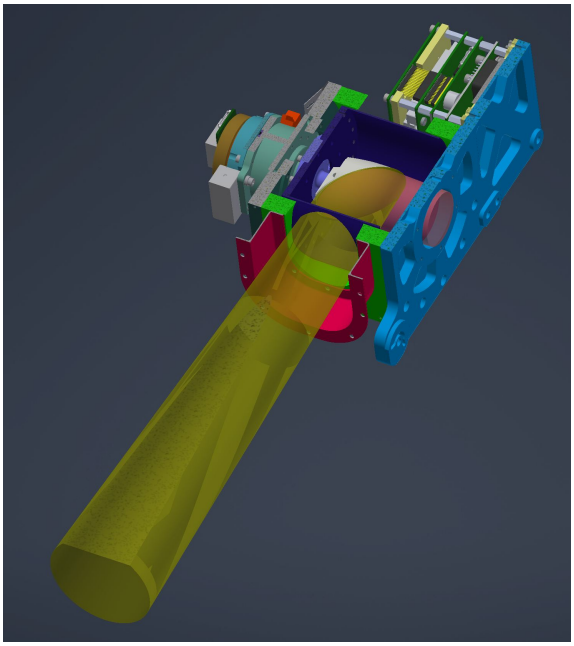

Figure 3.7: Schematic drawing of the pointing optic module of GLite. The transparent yellow cone is the field of view that is reflected by the 45° mirror into the IFMS block of the instrument. The blue cylinder turns together with the mirror and holds the entrance aperture. Figure by Roland Schmucker.

light is finally reflected backwards to the beam splitter. In Figure 3.6, the BSU is colored green, the corner cube reflectors are labelled CC-T and CC-R.
For the common Michelson interferometer the OPD is related to the physical position difference Δx by:

$$OPD = 2\Delta x \tag{3.9}$$

For a double pendulum interferometer where both mirrors move by Δx the OPD is twice as big, as each arm gives a path difference of $2\Delta x$.
In an interferometer arm with a moving mirror and a fixed retro reflector, the light beam has to travel four times the distance Δx. This leads to $OPD = 4\Delta x$ in one interferometer arm. The combination of retro-reflectors and the double pendulum as in GLite leads to:

$$OPD = 2 \cdot 4\Delta x = 8\Delta x \tag{3.10}$$

This makes it possible to build an interferometer that is substantially smaller than the maximum OPD it provides. In the case of GLite with $OPD = 2.5\,\text{cm}$ this leads to a distance of $0.3125\,\text{cm}$ the mirrors have to travel in each direction from the ZOPD position.

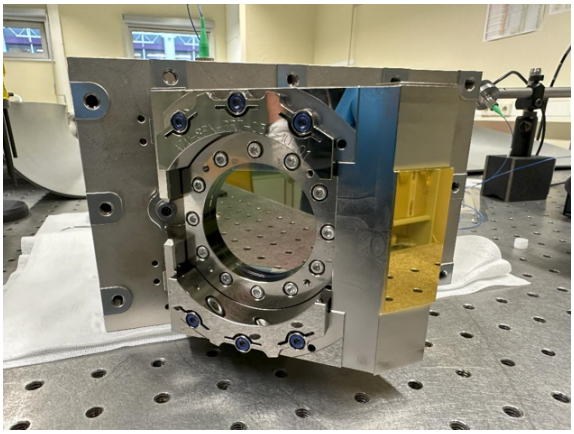

Figure 3.8: Beam splitter unit made of AlSi40 with diamond beam splitter and one retroreflector visible. The second retroreflector is on the right side around the corner. Figure from (Friedl-Vallon, 2025).

Beam splitter unit

In this type of interferometer, performance is driven by the relative alignment between the beam splitter and the retroreflectors. In contrast, the relative alignment between the corner cubes and other components is not critical. The solution to this challenge is to mount the beam splitter and both retroreflectors onto one monolithic block of AlSi40, the beam splitter unit. The alignment between BS and reflectors is done during the manufacturing process, so the BSU is delivered as a ready-to-use module that does not need any further adjustment. A picture of the BSU with beam splitter and one retroreflector is shown in Figure 3.8. The beam splitter itself is a 1 mm thick window of synthetic (CVD) diamond. The entire window is wedged by 10 arcmin to avoid interference patterns within the two surfaces. The front surface towards the entrance optics is the one defined as the splitting surface. It is coated to achieve a beam splitting behaviour close to $50/50$. The backward surface is coated with anti-reflective coating to reduce the reflectivity to $1/99$. The design of the BSU is one of the main contributions to the reduction of complexity and athermal behaviour of the instrument (Schwab, 2021).

Length measurement interferometer

To measure the position of the interferometer carriage in a very precise way, the length measurement interferometer (LMI) is used. It consists of an SWIR-laser that is coupled into the optical path of the interferometer via a fiber optic cable and a collimator. The collimator is placed in the COP module above the path for atmospheric measurements and sends the laser towards the beam splitter. The laser beam runs through the interferometer and travels back through the fiber optic to a circulator that deflects the beam towards an IR detector. The detector measures the intensity of the laser that passed through the interferometer.
To gain positional information, the zero-crossings of the LMI laser are counted, and each zero-crossing gets a time stamp. Each frame of an atmospheric measurement is also labelled with a time stamp. The LMI measurement delivers a spatio-temporal relation that allows to interpolate the atmospheric frames from temporal space onto a spatially equidistant grid. By using that process,

Property	Value
Entrance aperture diameter	18 mm
Effective focal length of COP	60 mm
Vertical spatial sampling	300 m
Horizontal spatial coverage	14 km
Spectral coverage	$750 - 1390\,\mathrm{cm}^{-1}$
OPD	2.5 cm
Spectral sampling	$0.2\,\mathrm{cm}^{-1}$
Temporal sampling	20 s

Table 3.5: Optical and spectrometric properties of GLite as used in the setup for the first flight. Data from (Friedl-Vallon, 2025; Schwab, 2021).

the influence of velocity fluctuations of the moving mirrors is corrected. The interferograms can now be Fourier transformed from the equidistant spatial grid to the wave number space (Ebert, 2024).

3.4.3 Camera Optics

The camera optics (COP) images the light onto the actual image plane of the detector. It consists of four off-axis aspheric mirrors, where the vertices of the mirrors share a common axis. As shown in Figure 3.6 the mirror pairs M1 and M3, and M2 and M4 are each mechanically coupled and manufactured as duoliths. The COP is designed to show athermal behaviour and independency of air pressure changes. While the instrument operates at an spectral range of 7 µm to 14 µm, the COP is designed for wavelengths from 3 µm to 14 µm. This makes later adaptions to different wavelengths easier, as the COP does not have to be changed.
The COP is designed in a quasi monolithic way out of three parts, the COP housing and the two mirror modules M1M3 and M2M4. The COP housing is a monolithic block of AlSi40, with channels machined in for the optical paths from the BSU to the mirror modules and to the detector. This massive design shall ensure mechanical stability, high thermal conductivity and heat dissipation. This is neccesary, as the COP housing acts as central unit of the instrument. All other parts, POM, IFMS, BSU and Detector are mounted to the COP housing. Top and bottom surface of the COP housing have mounting interfaces to mount the entire instrument into a gondola or satellite structure (Schwab, 2021).

3.4.4 Detector

The detector system is a modified HIPIR 640L VLWIR IDCA manufactured by AIM Infrarotmodule GmbH. The semiconductor used is Mercury-Cadmium-Telluride (HgCdTe, MCT) that is sensitive in the long-wavelength infrared spectral range. The mole fraction of Hg and Cd influences the band gap and thus the spectral window of the detector. This allows to tune the material for specific

Property	Value
Detector Type	Modified HIPIR 640L VLWIR IDCA
Manufacturer	AIM Infrarotmodule GmbH
Detector array and full frame readout frequency	640×512 pixels with 120 Hz
Used array and readout frequency	48×128 binned pixels with 3853 Hz
Pixel pitch	15 µm
Pixel pitch of binned pixels	30 µm
Full well capacity of binned pixel	$25\,\mathrm{Me}^-$
Operation temperature	75 K

Table 3.6: Detector properties of GLite. Data from (Friedl-Vallon, 2025).

applications (Sha, 2013). The system for GLite has a nominal spectral range from 7.7 µm to 14 µm and uses the low dark current p on n technology. The detector has 640×512 pixels with a pixel pitch of 15 µm. In order to reduce detector noise and the amount of data, 2×2 pixels are binned together, resulting in 320×256 pixels with a pixel pitch of 30 µm. For atmospheric measurements, only 48×128 pixels are used, which increases the readout frequency.
Each pixel charges a capacitor when the semiconductor is hit by photons. After the integration time, the capacitor charge is measured and converted by analog-to-digital converters (ADC). The ADC-Counts are saved in three-dimensional cubes, where the first two coordinates are the coordinates of the corresponding pixels. The third coordinate is the frame number. For each frame, a timestamp is also stored.
The detector is delivered as Integrated Detector Cooler Assembly (IDCA) which consists of the large focal plane array, a dewar with window and cold stop to separate the detector from the atmosphere, a stirling cooler to keep the detector at operation temperature and front-end electronics with the ADCs (Friedl-Vallon, 2025; Ebert, 2024). The major detector parameters are given in Table 3.6.

4 Methods

4.1 Flight measurement campaign

The maiden flight of GLite took place as part of the TRANSAT campaign on a stratospheric balloon operated by CNES. The takeoff took place on 22. June 2024 at ESRANGE in Kiruna, Sweden. After takeoff, the balloon ascended to an altitude of $37-40\,\mathrm{km}$ and was moved westward by stratospheric winds. From Sweden, the balloon crossed Norway and the Norwegian Sea north of Iceland. After that it crossed Greenland and Baffin Bay, before balloon and payload were separated over the northern part of Baffin Island after a total flight time of three days and 17 hours. The resulting flight path is shown in Figure 4.1. The gondola, shown in Figure 4.2, carried 8 scientific instruments from France, Sweden, Germany, and Canada and had a total weight of $2.9\,\mathrm{t}$. The aim of all instruments was to investigate atmospheric chemistry on a lager scale (Friedl-Vallon, 2025; Centre national d'études spatiales, 2024).

After the ascend, GLite successfully started taking measurements for several hours. During that time, the Gondola pointing was fixed to anti-sun direction due to heating of two other instruments. In normal measuring mode, the LOS elevation angle changes between $-1°$ and $-4°$ every three minutes. This results in 9 consecutive measurements per elevation angle. Every 30 minutes a calibration cycle is performed. For calibration measurements of deepspace and a calibration blackbody are taken. A detailed description of the calibration process is provided in section 4.4. On 23.06 at 23:34 UTC, CNES lost control of the gondolas azimuth control and the gondola performed

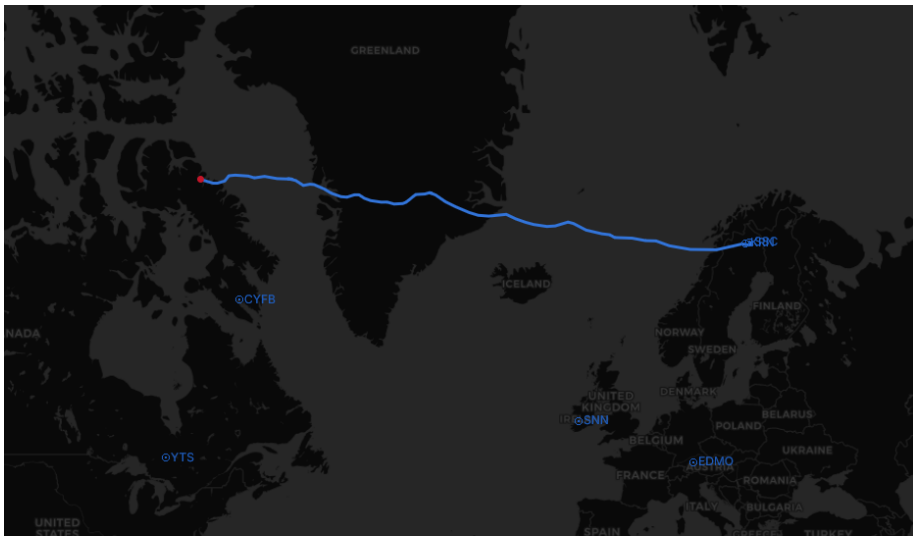

Figure 4.1: Flight path of the TRANSAT balloon from Esrange in Kiruna, Sweden to Baffin Island. Map by Erik Kretschmer.

Figure 4.2: The TRANSAT gondola with GLite mounted on it. Photo: Thomas Gulde

a full revolution around its vertical axis over the course of 50 minutes. This time period will be relevant in Chapter 5. Approximately one hour later, on 24.06 at 01:15 UTC, first problems with GLite arose. The interferometer carriage did not move and spectral measurements were not possible. Several attempts to fix this were only partially successful as the carriage always stopped again after a short time. During that period, stray light measurements were performed. By increasing the engine current and the movement speed of the carriage, the problem could be solved for a while with only a few failures inbetween. On 25.06 at 09:05 UTC interferometric measurements were stopped, as the interferometer drive finally failed. After that, some DC measurements without modulation were performed until the instrument was shut down for landing on 26.06 at 08:24 UTC. During the flight, a total of 5.5 terabytes of data were recorded. Investigations after the flight showed that the mechanical connection between interferometer carriage and the drive was broken. This has caused the problems and later failure of the modulator system. From then on, the interferometer carriage was not fastened anywhere. At the next strong acceleration, possibly the shock of the opening parachute or the ground impact, one of the corner cube reflectors slammed into the BSU and shattered. The damaged corner cube is shown in Figure 4.3.

4.2 Laboratory measurements

The laboratory measurements were performed after the instrument returned from Canada after the TRANSAT campaign. Its main objectives are the reproduction of the stray light effects seen during the flight as described in Chapter 5 and to produce a comprehensive qualitative description

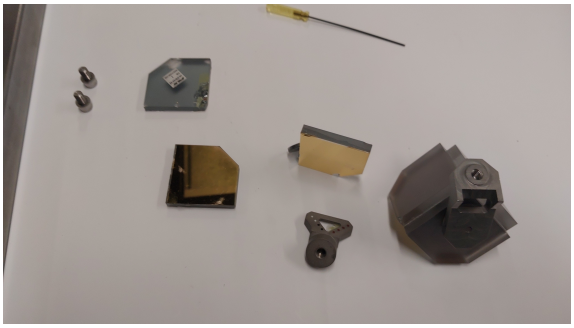

Figure 4.3: The damaged corner cube reflector is on the left side, shattered into its individual parts. The intact reflector is on the right side. Photo: GLORIA-Team

of the stray light behaviour of the instrument. Furthermore the PST as described in Chapter 2.4.1 should be determined. If some prominent stray light effects are detected, a further investigation of these should be done by measurements adapted to these effects. If possible, this should provide additional information to describe the actual stray light process and to identify the stray light path and the objects that cause the stray light.

The measurement setup is adapted from the collimated source test described in Chapter 2.4.2. A scheme of the setup is shown in Figure 4.4 while Figure 4.5 shows a photo the actual measurement setup.
The radiation source is a combined blackbody/chopper unit mounted on a height adjustable tripod. The radiation is not collimated but sent directly towards the instrument. Due to the build in electronics of GLite, no lock-in amplifier is used. Instead, a digital lock-in is used in the data processing. Because the interferometer is inoperable, the radiation is not modulated and the detector simply records one frame after another without providing timestamps to relate the frames to the OPD. This mode is called DC mode. The detector samples at 3853 Hz, each frame is saved in the cube together with its timestamp. During data processing this allows to separate the chopper signal via Fourier transform from background radiation. A detailed description of the data processing is provided in Chapter 4.4.

During measurement, the tripod is permanently placed at its position and not moved. The elevation angle of the blackbody relative to the horizontal plane ϕ_{BB} is adjusted by moving the tripod up and down. The azimuth of the blackbody relative to the LOS of the instrument θ is adjusted by turning the instrument on a turntable. The instrument is placed on the turntable so that the 45 scanning mirror is aligned with the rotation axis. The elevation angle of the LOS is controlled by the POM. The height of the blackbody above the reference plane is determined by using a pocket rule with millimetre scale. The reference plane itself is marked by a self-levelling cross-line laser as used on construction sites. This simply allows to measure the vertical distance between the laser marking

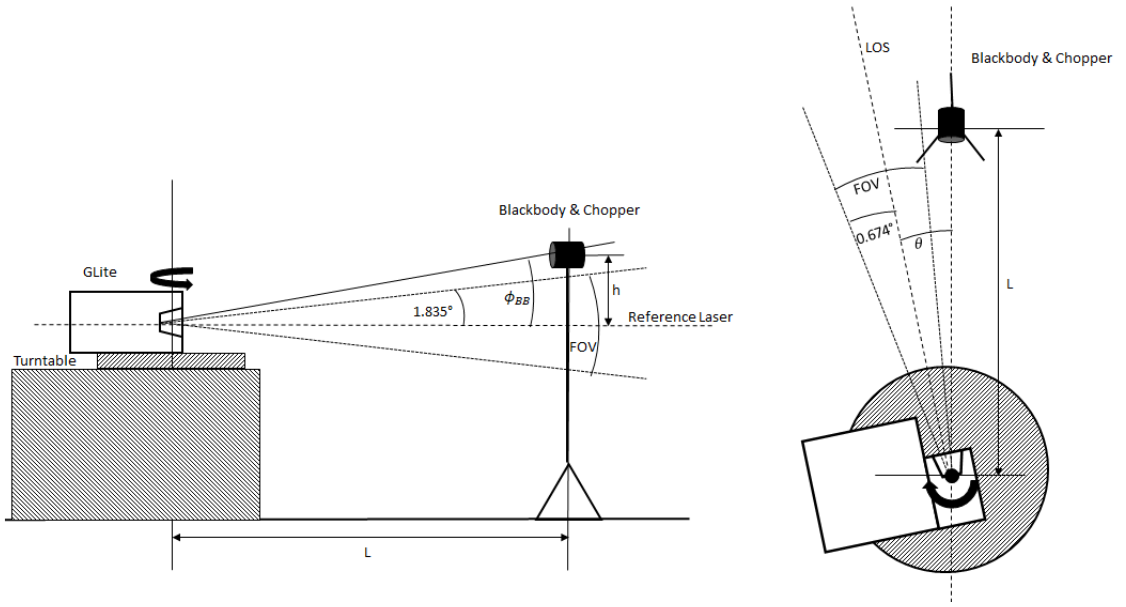

Figure 4.4: Schematic representation of the measurement setup.

and the centre of the blackbody which is also marked on the blackbody housing. This height h is related to the elevation angle of the blackbody ϕ_{BB} by:

$$tan(\phi_{BB}) = \frac{h}{L} \tag{4.1}$$

where L is the distance between the blackbody and the aperture entrance of the instrument. As shown in Figure 4.6, the azimuth angle θ can be read directly on the side of the turning table on a $0.25°$ scaling with a sight. Here, θ is negative if the LOS is on the left of the BB and positive if the LOS is on the right.

The measurements were taken in a low-dust optic lab room at KIT Campus Nord. The temperature in the lab could not be controlled as the room has only a ventilation system but no air-conditioning. Sun blinds at the windows block sun radiation in order to reduce room heating in summer and to reduce the background radiation. This has no effect on the chopper signal but can reduce general photon load and detector noise.

4.3 Data acquisition in the laboratory

After completion of the measurement setup, the instrument was levelled by using levelling screws. For a calibration of the line of sight, the reference laser and the blackbody aperture were brought to the height of the LOS at the aperture. Then the elevation angle of the scanning mirror G_E was varied until the image of the blackbody appeared in the middle of the detector image. That was the case at an angle of $G_E = -0.15$. This angle is used at all the following measurements if the instrument is supposed to look straightforward.

The distance L between blackbody and instrument was set to 1.08 m for all measurements. A short distance would provide more radiation even at large off-axis angles, while a large distance results in

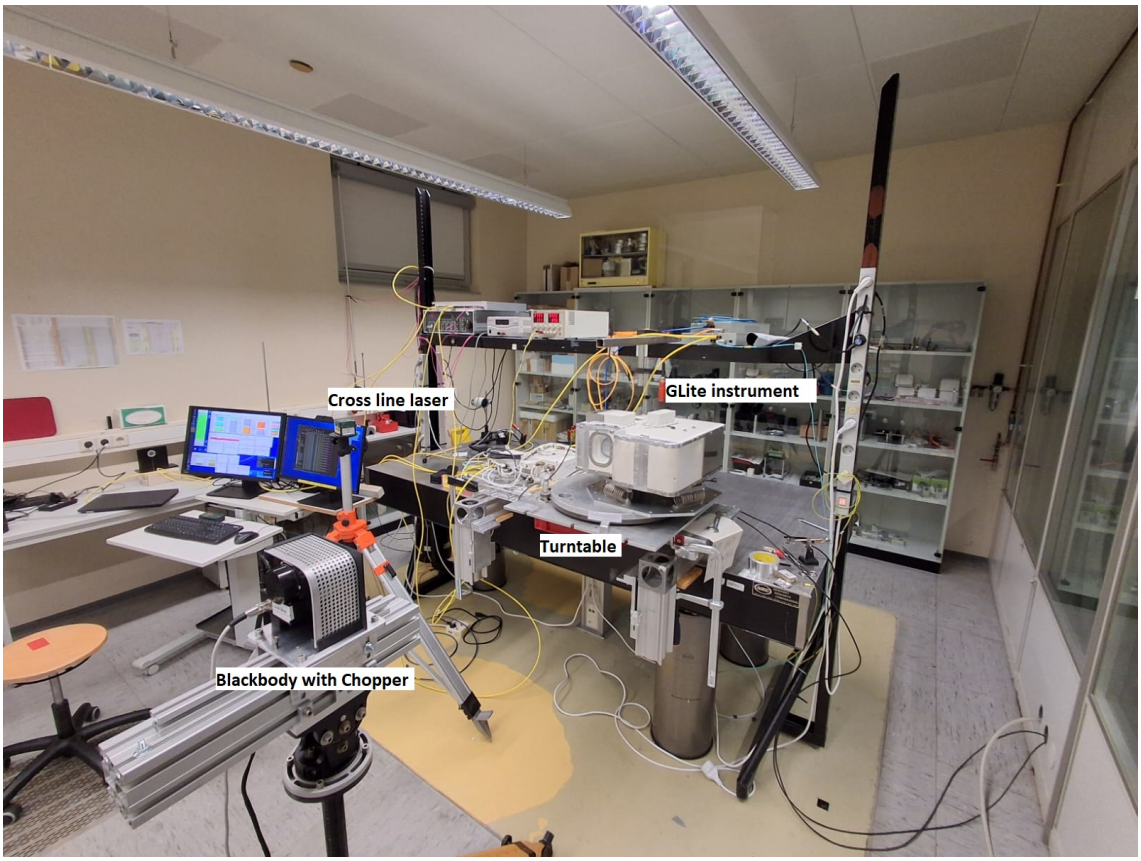

Figure 4.5: Photo of the measurement setup with the blackbody unit in the foreground, the instrument on the turntable in the middle, the cross-line laser on the second tripod, and the control station in the background.

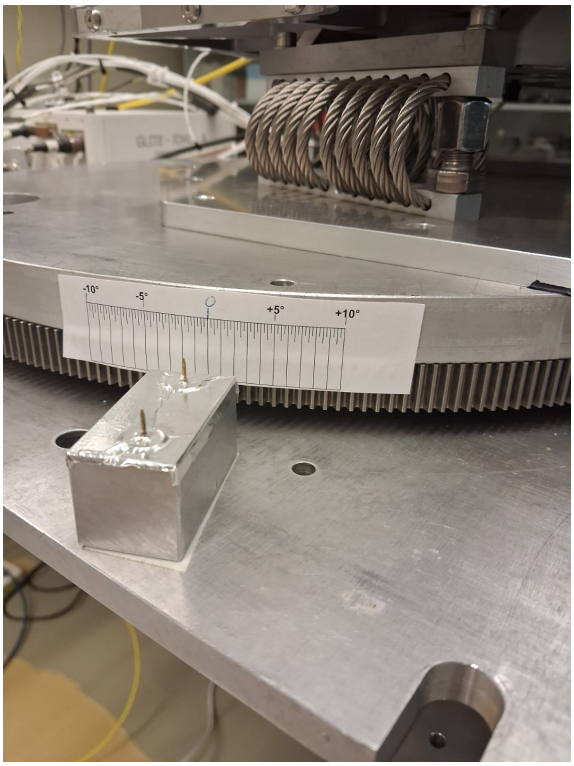

Figure 4.6: Depiction of the azimuth scale on the turntable with the sight out of two pins on an aluminium block for more precise reading.

sharper images because the rays would be closer to perfectly parallel rays. Here, the distance was chosen in favour of more signal. In addition, at that distance the aperture of the blackbody roughly would have the apparent size of the sun.
For all measurements the temperature of the BB is set to $1000\,^{\circ}\mathrm{C} = 1273.15\,\mathrm{K}$ which is the maximum operation temperature of the BB in order to produce the strongest possible signal. The chopper frequency is set to 188 Hz which is some kind of arbitrary. It is important that the chopper signal has a frequency lower than the Nyquist frequency of the detector that is $f_{nyquist} = f_{det}/2 = 3852\,\mathrm{Hz}/2 = 1926\,\mathrm{Hz}$ otherwise aliasing would occur. It is also reasonable to choose a frequency that is not a multiple of 50 Hz otherwise interference signals from the regular power grid could influence the data.
The integration time of the detector is determined by the ITC (InTegrationCounter) value. If the BB is supposed to be close or within the FOV ITC= 47 is set which equals an integration time of 14.3 µs to prevent overexposition. If the BB is further away from the FOV ITC= 20 is set resulting in a longer integration time of 152 µs to increase sensitivity to the weaker signal.
A single measurement has a duration of approximately 10 s. This is a trade-off between a very long measurement in order to measure as many periods of the chopper signal as possible and the amount of data generated. Practical considerations for performing the measurement also played a role.

4.3.1 First stray light measurements

For the first series of measurements the measurement geometry is shown in Figure 4.7. Relative to the FOV the BB is moved in 1° steps along the azimuth and elevation axis from -10° to 10°. First the measurements along the azimuth axis are performed for ITC values 47 and 20. The vertical measurements had to be split up, because the vertical freedom of the tripod is limited and does not cover the whole vertical range. Thus the tripod had to be rearranged. The first part along the vertical axis from -10° to 6° was measured for both ITC values. After that, the second part along the vertical axis from 6° to 10° is measured for both integration times.
The goal of this measurement is to measure in a simple geometry to get an expression of the stray light behaviour of the system to plan further measurements. These measurements also provide data for some basic analyses and improvement of the processing algorithms. The results are described in Chapter 6.1.

4.3.2 Reproduction of the in-flight effects

The aim of the second measurement series was to reproduce the effects described in Chapter 5.2. Therefore, the LOS should move horizontally from -3.5° to 3.5° in 0.5° steps. This was done at three different elevation angles ϕ_{BB}: 3.0°, 3.7°, and 4.0° because there is some uncertainty in the flight data with respect to azimuth and elevation. The measurement geometry is shown in Figure 4.8. Here measurements are taken only at $ITC = 47$ as the BB is quite close to the FOV and a longer integration time would lead to overexposure. The results are shown in Chapter 6.2.

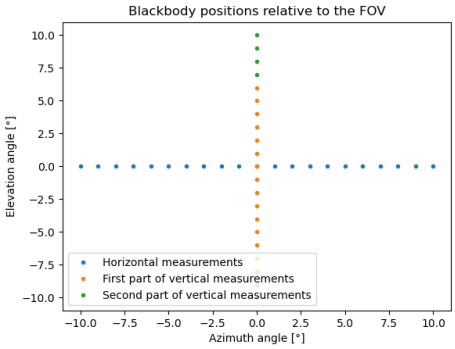

Figure 4.7: Measurement geometry for the first stray light measurements. The dots represent the blackbody position relative to the field of view. For better visibility the size of the dots is not to scale. The vertical measurements are split up into two parts because the vertical range of the tripod is limited and it has to be rearranged.

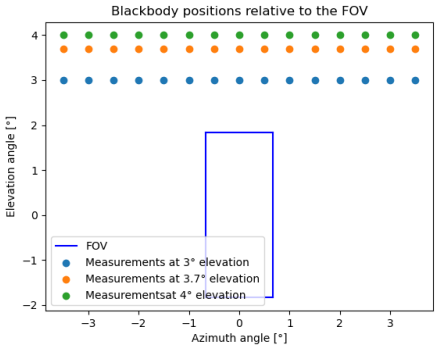

Figure 4.8: Measurement geometry for the reproduction of the in-flight effects of the sun. The dots represent the blackbody position relative to the field of view. For better visibility the size of the dots is not to scale.

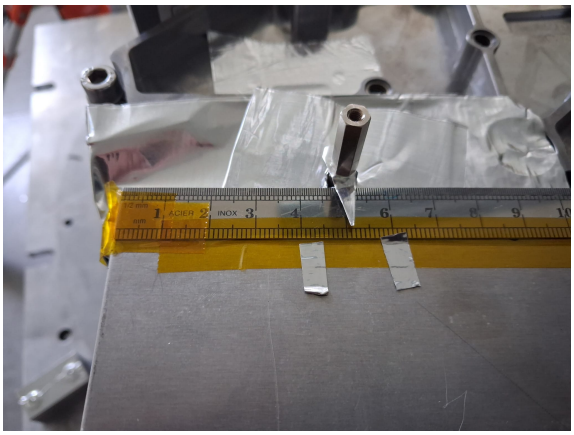

Figure 4.9: Ruler and positioning handle for the interferometer carriage. The aluminium stripes at 4.5 cm and 5.7 cm show the mechanically possible range of movement.

4.3.3 Effect of the interferometer carriage position

The aim of this measurement is to establish whether the position of the interferometer carriage influences the stray light behaviour.

As the interferometer drive was inoperable, the interferometer carriage has to be manually positioned. To reproduce the positions of the interferometer carriage during the measurements, a ruler is placed on top of the instrument next to the handle that moves the carriage, as shown in Figure 4.9. The reference position is not related to the OPD. For the measurement the reference positions 5.0 cm, 5.2 cm, and 5.4 cm are chosen. Here, the LOS varied along the azimuth axis from $-10°$ to $10°$ in $1°$ steps while ϕ_{BB} is fix at $0°$. In addition two measurements are taken with azimuth$= 0°$ and elevation angles $6°$ and $7°$. At each blackbody position a measurement for each of the three interferometer carriage positions is taken. The whole process is performed twice for the different ITC values 47 and 20. The results are described in Chapter 6.3

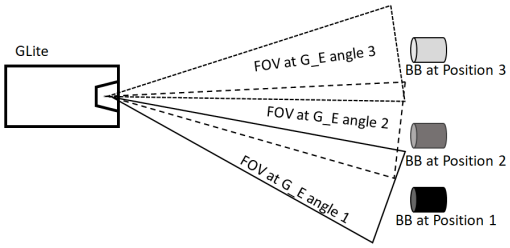

Figure 4.10: Schematic depiction of the measurement principle for varying the G_E angle. For each BB position measurements at all elevation angles are taken. This results in seeing the same relative scenes at different absolute elevation angles.

4.3.4 Investigation of a selected stray light effect and the effect of different improvements

To understand the origin of a selected ghost-like reflection that occurs if the blackbody is placed 6° or more above the LOS, additional measurements are taken. This effect was chosen, because is relatively strong and its origin could not be explained at all. The first measurements varies the angle of the scanning mirror G_E to check whether this affects the reflection. The measurement principle is shown in Figure 4.10. The blackbody is placed at azimuth 0° for all measurements. For a given vertical position of the BB, G_E is varied from $-6.15°$ to 10.85° in 1° steps after each measurement. This results in elevation angles of the LOS relative to the horizontal plane ranging from $-6°$ to 11°. After each series, the elevation angle of the blackbody ϕ_{BB} is increased by 1° ranging from $-2°$ to 10°. The effect that is investigated is weak and far away from the FOV. Thus, the ITC is set to 20 for all measurements. This results in increased sensitivity in the region of interest when the BB is more than 6° above the LOS. However, measurements closer to the FOV are overexposed and thus not usable. Following, a series of measurements is taken where certain parts of the instrument that are suspected of being involved in the stray light path are covered. The interior of the instrument is mainly bare metal and thus reflective. To reduce the reflectivity, the metal surface is covered with cardboard or foam sheets. Cardboard has a emissivity of 0.81 for styrofoam the emissivity is 0.6. The reflectivity r is given by $r = 1 - \varepsilon$, where ε is the emissivity. Thus, the reflectivity for both materials is significantly lower than for bare AlSi. For aluminium, the emissivity is 0.05, so the reflectivity is very high (Marshall, 1982).
For the measurements the blackbody is placed at $\phi_{BB} = 6°$, G_E is varied as in the previous measurement. This measurements are done only for one blackbody position due to practical reasons. Measuring multiple BB positions for each change within the instrument would increase effort, while the additional gain of information is expected to be low. If the stray light path is blocked for one BB position, it may be expected that this is also valid for other positions close to the one measured. Especially because the relative angle between BB and LOS is varied during the measurement. The results of these measurements are described in Chapter 6.4.

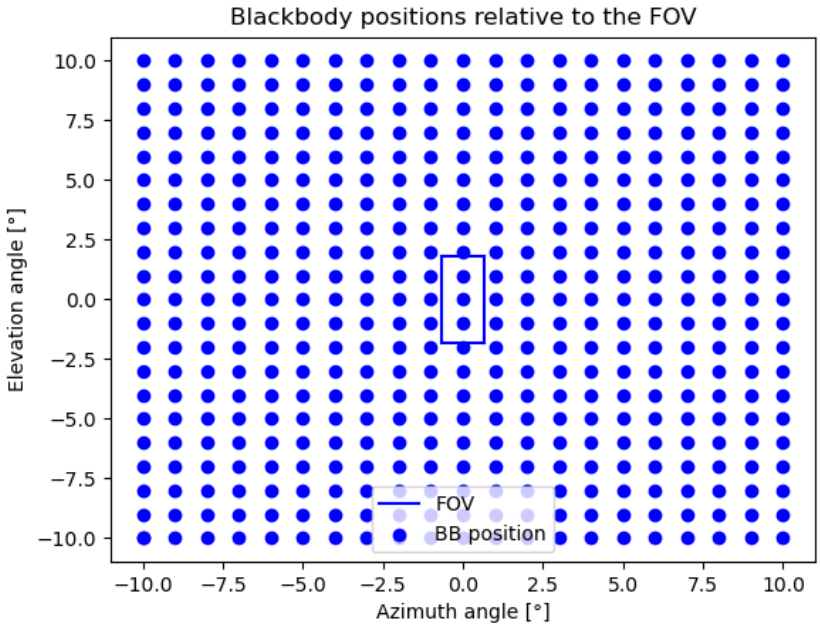

Figure 4.11: Measurement geometry for the stray light measurement in the full angular space similar to Figure 4.7.

4.3.5 Comprehensive stray light measurement

This measurement series aims for a comprehensive measurement of the stray light behaviour in the angular space from $-10°$ to $10°$ in azimuth and elevation with a spacing of $1°$. The measurement geometry is shown in Figure 4.11. From these measurements the PST will be determined. This measurement also provides an overview around the FOV and might find effects that are not on the main axes and thus are not seen by the previous measurements.
For this measurement, the interferometer carriage was positioned very close to the ZOPD position. This was done by moving a wedge between the moving handle of the carriage and a fixed point. By slowly moving the wedge the carriage position could be adjusted very precisely until the detector image shows a Haidinger fringe pattern indicating the ZOPD position. From there, the wedge is moved a bit until the fringe pattern disappears. At this position the carriage is fixed to prevent unintended movement.

4.4 Data processing of flight measurements

The data processing for GLORIA-Lite is based on the data processing of GLORIA as described in (Kleinert et al., 2014). A flow-chart of the level 0 and level 1 data processing is shown in Figure 4.12. As this process is not the focus of this thesis, only a brief description is provided here.

Level 0 processing

The core of the level 0 processing is the resampling of the raw interferogram from the temporal space to a spatial-equidistant grid. This is done by using the approach from (Brault, 1996). The frames in the interferogram are labeled with a timestamp and thus provide a intensity-time relation. The length-measurement interferometer (LMI) delivers a space-time relation that allows to interpolate the interferogram to an equidistant grid to get an intensity-space relation that can be further processed by Fourier transform. In addition, the level 0 processing checks for missing frames and performs different corrections for nonlinearity and spikes in the data (Sha, 2013; Kleinert et al., 2014).

Level 1 processing

The level 1 processing generates a radiometric calibrated spectrum out of the resampled interferogram. This is achieved by performing a Fourier transformation of the resampled interferogram. This provides an uncalibrated spectrum. By using calibration measurements of the deep space and an integrated blackbody the calibrated spectrum is calculated as:

$$A_a = S_a \frac{L_{BB}}{S_{BB} - S_{DS}} - \frac{S_{DS} L_{BB}}{S_{BB} - S_{DS}} \tag{4.2}$$

where A_a is the calibrated spectrum, S_a is the uncalibrated spectrum in ADC counts, S_{BB} and S_{DS} are the blackbody and deep space spectra as zero measurement and L_{BB} is the Planck function of the calibration blackbody (Sha, 2013; Kleinert et al., 2014).
This radiometric calibration is also used to calibrate single frames of the results shown in Chapter 5.2. There, effects are shown that appear and move within a single measurement and thus can not be seen after Fourier transform but only in the raw frames of the interferogram. There, S_a is one interferogram frame in ADC counts and A_a is a calibrated frame.

4.5 Data processing of lab measurements

4.5.1 Basic principle

The goal of the lab data processing is to separate the chopped blackbody signal from the background radiation. This is done by performing a Fourier transform of the recorded signal of each pixel. Figure 4.13 shows two examples of recorded signals. In the upper plot the modulated square wave is visible with almost no distortions. In the lower plot, the modulation is still visible but overlaid by noise and about 800 times weaker in amplitude.
By performing a Fourier transform, the signal is transformed from the temporal domain to the frequency domain. By looking only at the chopper frequency component, most of the background noise is cancelled. By doing this for each pixel, an image of the amplitudes of the chopper frequency component is generated.

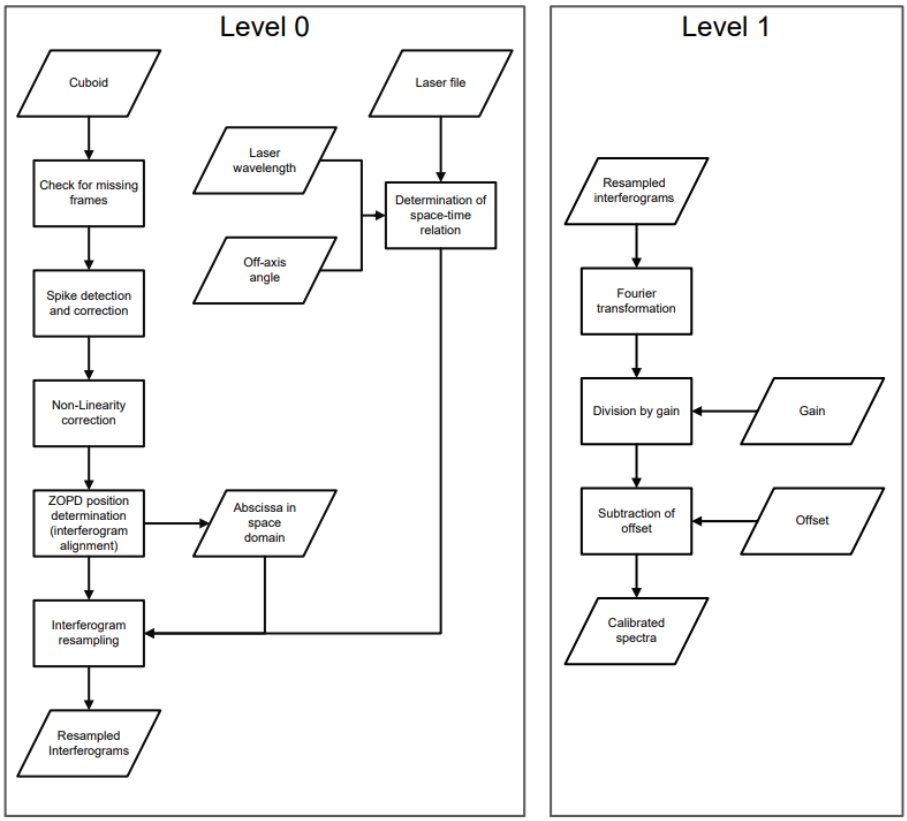

Figure 4.12: Simplified flowchart of the level 0 (left side) and level 1 (right side) processing. Figure from (Kleinert et al., 2014).

It turns out that the frequency of the chopper is not perfectly stable but drifts about 2 Hz up and down over time. This makes a frequency-detection algorithm necessary. The most obvious solution is to define the maximum signal within a given frequency window as the chopper signal. Therefore, the magnitudes of all pixels are averaged. The frequency at maximum signal between 186 Hz and 190 Hz of the previously calculated mean is considered the detected chopper frequency. As long as the chopper signal is stronger than the surrounding noise, this works fine. If the signal is in the order of magnitude of the noise, this approach leads to false detections.

To increase data quality, measurements with falsely detected chopper frequencies are corrected. The false detections are identified by their deviation from the moving median over the measurement series. A chopper frequency that deviates more than 0.25 Hz from the median is considered a false detection. In this case, the detection algorithm runs again but the median value is defined as the chopper frequency instead of taking the maximum signal as the chopper frequency. In Figure 4.14 the detected frequencies of the first measurement series are shown. The false detections only occur if the signal-to-noise ratio is low because then the highest noise peak is chosen as chopper frequency. The detected frequency after the false detection correction is shown in Figure 4.15. There, the false detections are corrected.

As last step of data processing, all pixels that are flagged as invalid by the regular level 1 processing algorithm are excluded from further processing (Kleinert et al., 2014).

Most of the data used are normalised relative to the brightest pixels that look right onto the blackbody source. This allows to relate the intensity of the stray radiation to the intensity of the

source. Therefore the highest pixel value from ten measurements that look right at the blackbody are selected and averaged. All other measurements are divided by that factor.

4.5.2 Detection algorithm

This section describes the detailed steps of the data processing algorithm:

1. Fast Fourier transform of the detector frames
2. Calculate magnitude spectrum of the Fourier transformed data
3. Reduce spectra to window of interest between 186 Hz and 190 Hz and increase spectral resolution by backward Fourier transform, zerofilling the data by a factor of 16 to increase spectral resolution and transform forward again.
4. Calculate the zerofilled spectra and average over all pixels.
5. Frequency of the maximum in the mean spectrum is defined as detected chopper frequency
6. For signal-to-noise ratio calculation, zerofilled spectra of the frequency ranges $166-186$ Hz and $190-210$ Hz are calculated. Figure 4.16 shows the three frequency ranges for signal detection and noise determination.
7. SNR determination by: $SNR = \left(\frac{A_{signal}}{A_{noise}}\right)^2$ where A_x are the root mean square amplitudes of the chopper signal and of the background noise between 166 Hz and 186 Hz and 190 Hz and 210 Hz.
8. Generation of a netcdf file that contains the raw data, the magnitude spectrum, the amplitude at the detected chopper frequency, and the SNR, all for each pixel. In addition, the value of the detected chopper frequency and the overall mean noise amplitude are provided.

For the measurements that tried to reproduce the in-flight effects it turned out, that the chopper frequency was below the frequency window of $186-190$ Hz. Therefore the window was shifted to $180-190$ Hz for that measurement series.

After applying this algorithm to all measurements, the identification and correction of all false detections is performed:

1. Calculate moving median of the detected chopper frequency for each measurement of a measurement series. The window length is 5 % of the total number of measurements within the series.
2. Check whether the detected chopper frequency deviates more than 0.25 Hz from the moving median.

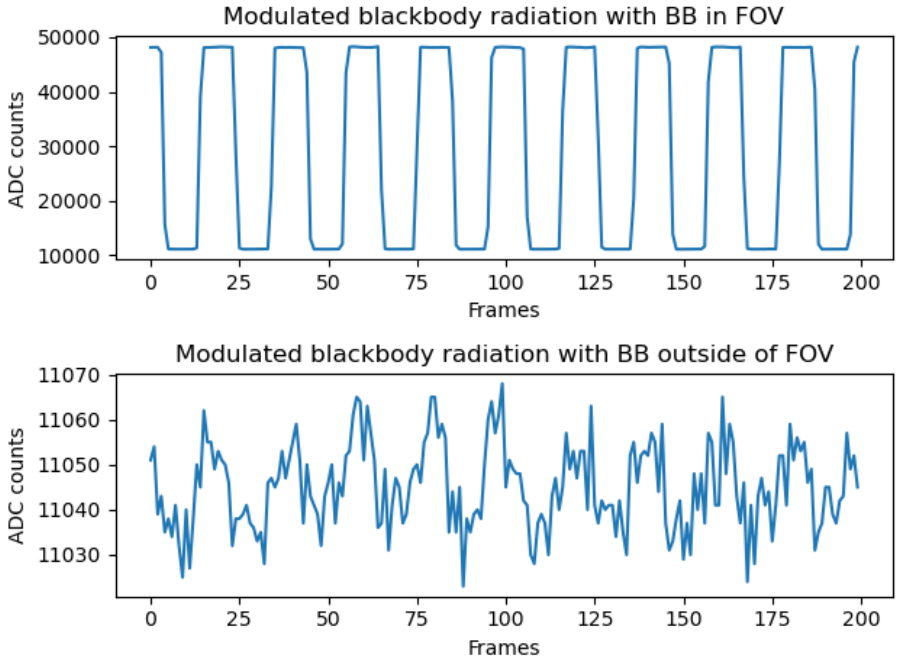

Figure 4.13: Two examples for the radiation detected during the lab measurements. Both plots show the signal of one pixel over a range of 200 frames. The upper signal is from a pixel that is looking directly into the chopped blackbody showing the square-wave signal with almost no distortion. The lower plot shows the signal of a measurement where the blackbody is outside of the FOV.

3. If it is a false detection, the steps 3,6,7 and 8 of the previous algorithm are executed again, but instead of taking the maximum signal as chopper frequency, the median is taken as target frequency.

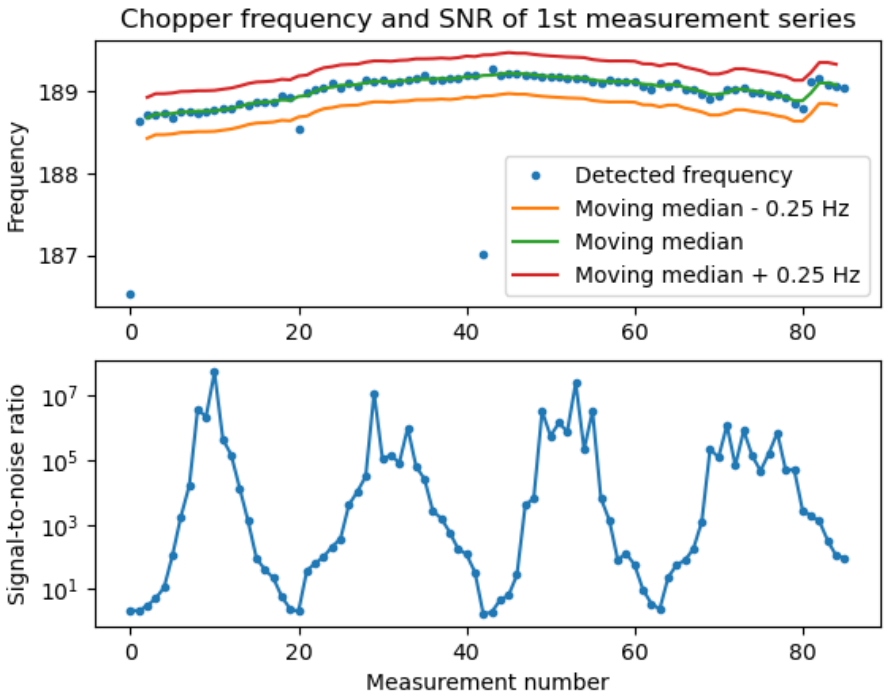

Figure 4.14: Detected chopper frequency and signal-to-noise ratio for each measurement during the first measurement series prior to the correction of the false detections. The false detections are the points outside of the $\pm 0.25\,\mathrm{Hz}$ corridor of the moving median.

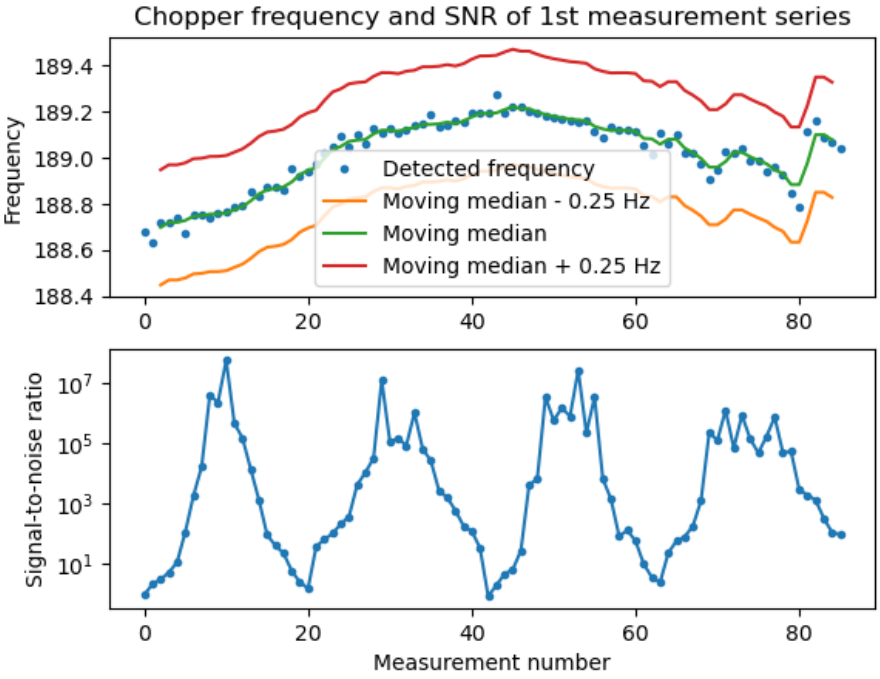

Figure 4.15: Detected chopper frequency and signal-to-noise ratio for each measurement during the first measurement series after correction of the false detections.

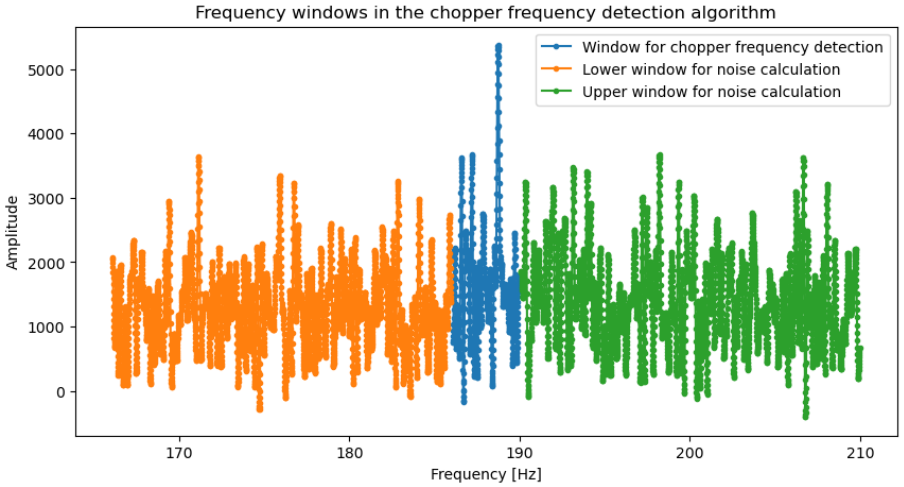

Figure 4.16: Schematic representation of the frequency ranges that are used for chopper frequency detection and noise determination. In this example, the peak of the true chopper signal is easy to find.

5 Flight measurement results

In this chapter, measurements gained during the flight are assessed to get a first impression of the stray light behaviour. The focus of the first section is on the assessment of the regular measurement operation. The second section focuses on the analysis of one single event, where stray light could be observed directly.

5.1 Analysis of operational measurements

5.1.1 Basic principle

During normal measurement operation, the LOS elevation angle is toggles every three minutes between $-1.33°$ and $-4.07°$. This process provides an overlap in the FOV of both measurement angles of $0.93°$. A sketch of the geometry is provided in Figure 5.1.
The atmosphere within the overlap area is sampled at both elevation angles but at different positions within the FOV and thus the radiation hits the detector at a different position. This provides the possibility for a first stray light assessment of the operational measurements during the flight: In an ideal instrument, measurements of the same atmospheric region with different detector pixels should still lead to the same results. Deviations from the ideal chase imply that a change in the measurement geometry also changes the intensity distribution at the detector. The presence of stray light can cause such effects. The toggling alters the background scene relative to the FOV, and thus the radiation source for certain stray light paths is a different part of the atmosphere, which may lead to a altered intensity of the stray light effect that affects the radiation intensity distribution at the detector.

5.1.2 Analysis

To analyse these effects, three cubes each right before and after an elevation change are averaged to reduce noise. Then, mean vertical radiance profiles are generated for each averaged cube by averaging over horizontal pixels and wavenumber. These vertical profiles now are matched according to their overlap, and the profile of the upper FOV is subtracted from the profile measured in the lower FOV. The matching of the profiles was provided by (A. Kleinert, personal communication,2025) by minimizing the spectral difference of the horizontally averaged pixels. This leads to a shift of 91.5 pixels, so pixel row 0 in the lower FOV sees the same region as pixel row 91 or 92 in the upper FOV. This leads to 36 pixel rows that can be matched: Rows 0 to 35 in the $-4.07°$ FOV match

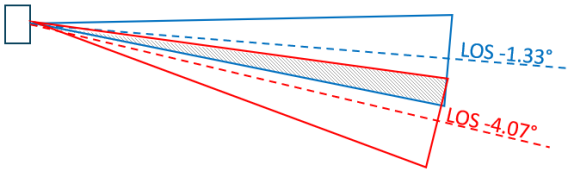

Figure 5.1: Sketch of the toggling process. The blue section represents the FOV at $-1.33°$ elevation while the red section represents the FOV at $-4.07°$ elevation. The shaded region is the overlap of both FOVs.

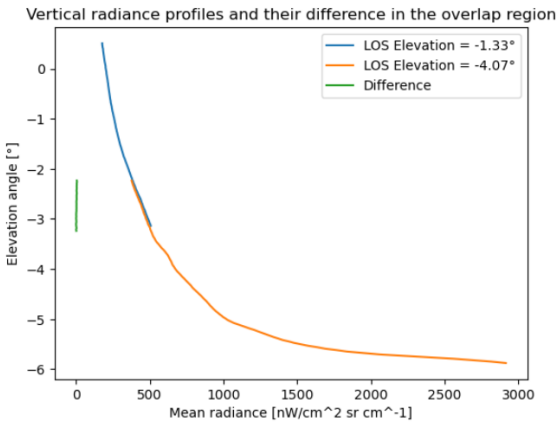

Figure 5.2: Measurements from 23.06.2024 19:16 and 19:17 UTC. The blue and orange curves represent the measured vertical radiance profiles at LOS elevations $-1.33°$ and $-4.07°$. The green curve is the difference of both profiles whereby the the upper profile is subtracted from the lower one.

with pixel rows 92 to 127 in the $-1.33°$ FOV. Figure 5.2 shows the two vertical profiles and the difference in the overlap region.
The analysed measurements were taken between 23.06.2024 16:16 UTC and 24.06.2024 12:44 UTC and provide 55 toggle processes.

5.1.3 Results

The 55 difference profiles are shown in Figure 5.3 while Figure 5.4 shows the mean of all difference profiles. Most of the differences are positive and range from 0 to $10\,\mathrm{nW/cm^2\,sr\,cm^{-1}}$ indicating that a bit more radiation is detected within the lower FOV. The mean of all differences is also positive and shows that the differences in the upper part of the overlap area are generally bigger than in the lower part.

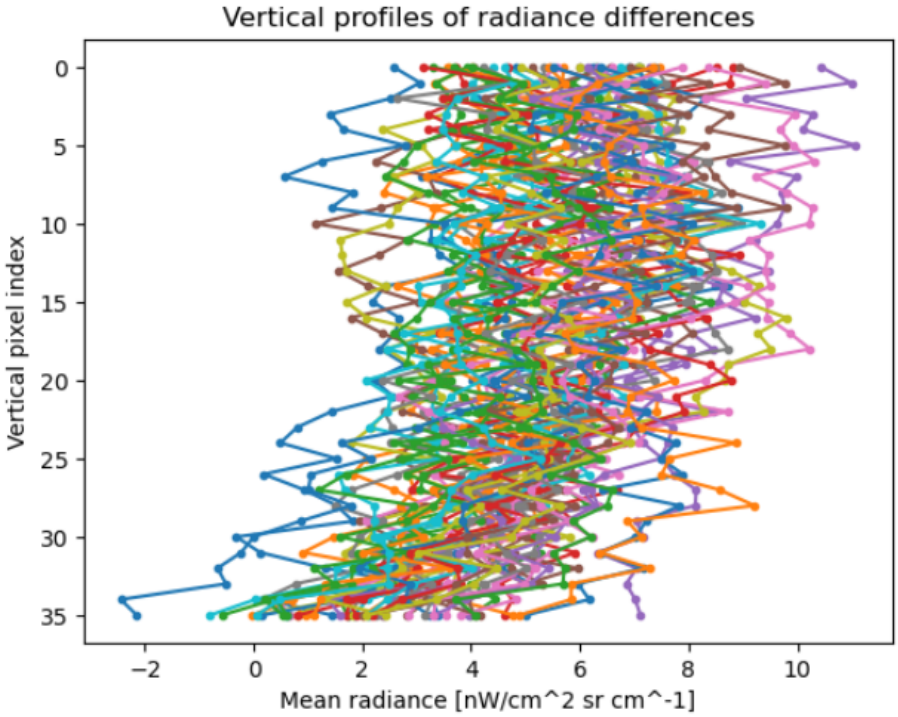

Figure 5.3: Profiles of all 55 radiance differences. The vertical pixel index refers to the pixel rows of the $-4.07°$ measurements.

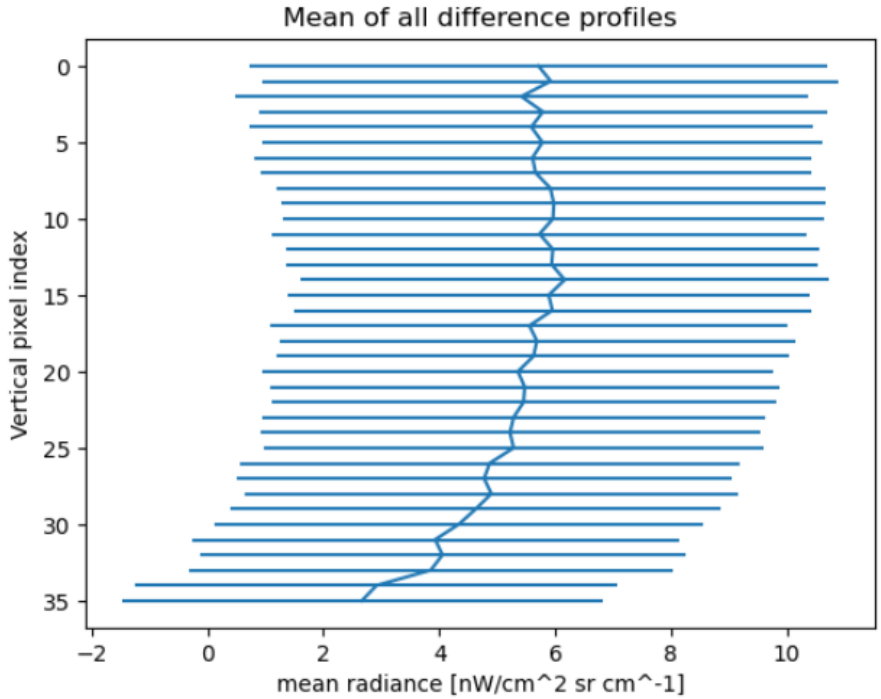

Figure 5.4: Mean of the difference profiles from Figure 5.3. The error bar depicts the standard error of the mean.

5.2 Failure of gondola azimuth control

5.2.1 Event description

Sometimes even mishaps can be turned into knowledge gain, just like in this case: Between 23.06.24 23:34 UTC and 24.06.24 00:20 UTC, CNES temporarily lost azimuth control of the gondola. Thus, the gondola made a full clockwise revolution around its vertical axis before control was regained. An overview of the azimuth angle over time is shown in Figure 5.5. Usually, the gondola was oriented so that GLite would look away from the sun. Due to the rotation of the gondola, GLite was looking towards the sun for a short time period. Figure 5.6 shows a picture of the GoPro camera that was mounted next to Glite, where the instrument was facing right towards the sun. To calculate the position of the sun relative to the FOV, the Skyfield software package (Rhodes, 2019) was used. The resulting relative positions for the relevant cubes are shown in Figure 5.7.

5.2.2 Observed effects

Looking at the data measured during that period, four consecutive cubes show effects that are likely caused by stray light from the sun. Figure 5.8 shows an example frame. On the upper edge of the detector image 3 bright spots are visible that move to the left or right over time.
A different representation of the effects is shown in Figure 5.9 where the upper row of pixels of each frame is plotted over time with respect to the horizontal orientation. It shows that there are three spots that move together in the opposite direction of the rotation. Figure 5.10 shows more detailed sections of Figure 5.9 and relates them to the position of the sun.
Figure 5.11 provides a different perspective for the intensity of the bright spots. Here, only a few frames for a time period of linear movement of the LOS are shown. The intensities of the brightest spot varies a bit, mainly depending on the position within the FOV. If the spot comes closer to the edges it weakens a bit. The spot on the right has almost no variation while the left varies also with its position. Compared to the main spot, the right spot has 51.8% intensity, while the left one has 36.7%.
When the maxima of the main spot in the middle and one of the side spots are visible in the same detector image, the distances between can be measured directly. This leads to a distance between the main spot and the left spot of 42 pixels and 36.5 pixels between the right spot and the main spot.

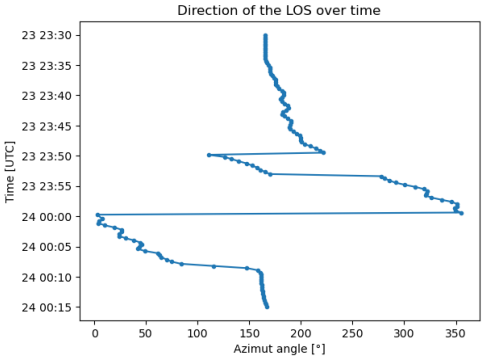

Figure 5.5: Azimuth of the LOS during the uncontrolled gondola rotation. The jump in the data between 23:50 UTC and 23:55 UTC is caused by a calibration sequence, where the instrument is looking at its calibration blackbody. There the LOS elevation is 90° and thus azimuth is not properly defined.

Figure 5.6: Image from a GoPro camera mounted right beside GLite showing that the instrument was looking towards the sun.

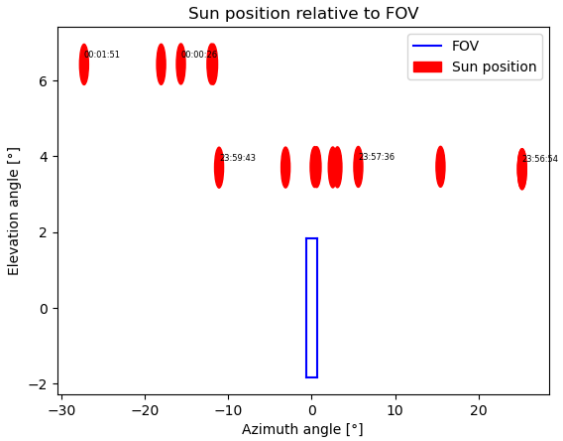

Figure 5.7: Position of the sun relative to the FOV during the rotation of the gondola. Each red spot marks the sun position at the measurement start of a cube. The spots are to scale with the apparent size of the sun.

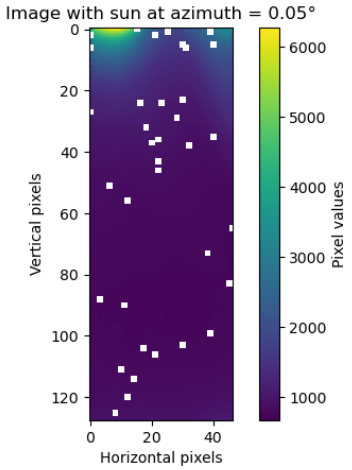

Figure 5.8: Exemplary detector image with bright spots at the upper edge that are likely caused by the sun.

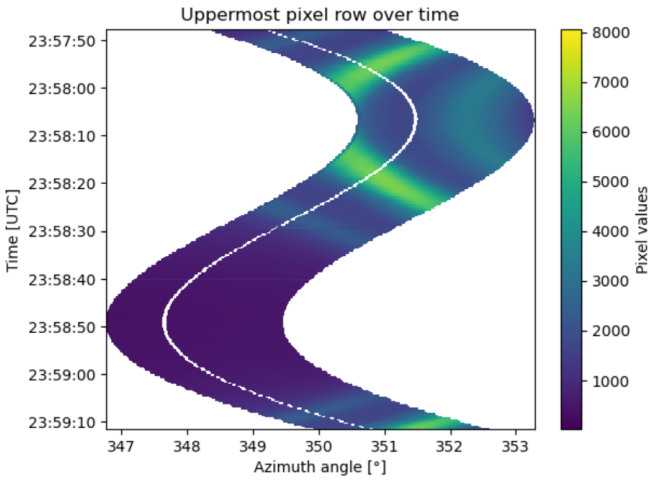

Figure 5.9: Representation of the behaviour of the bright spots from Figure 5.8 over time. Here the upper pixel row of each consecutive frame is plotted over time and aligned according to its azimuth angle.

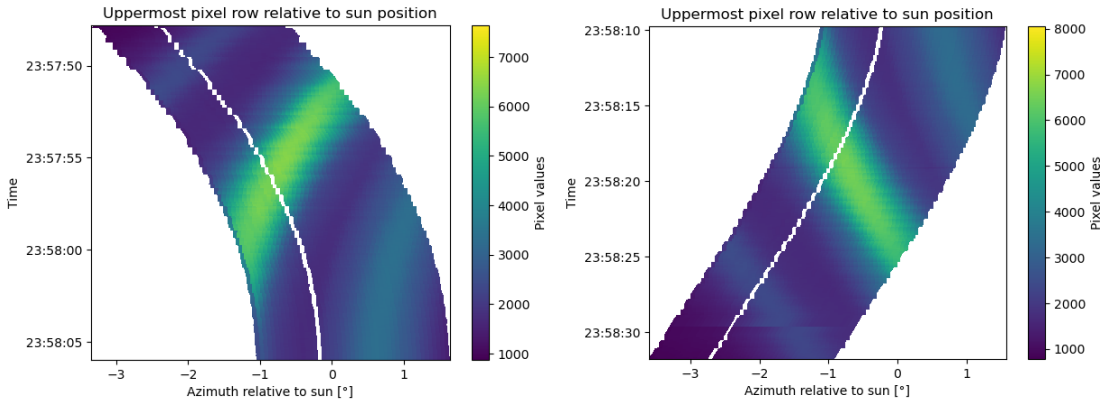

Figure 5.10: Detailed image sections from Figure 5.9 relative to sun position.

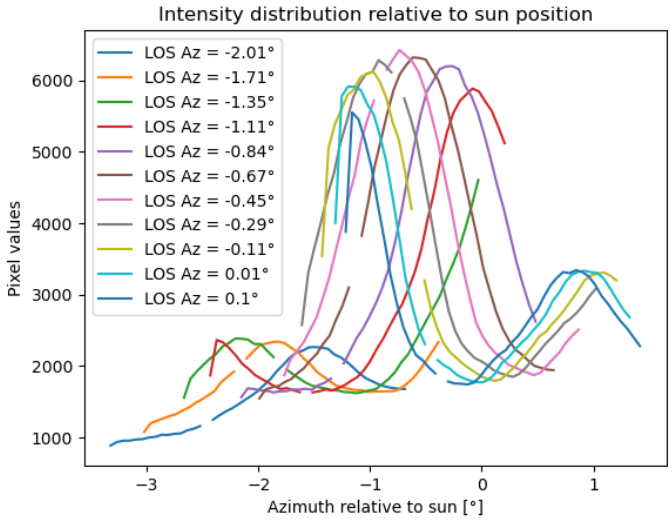

Figure 5.11: Intensity distribution of the upper pixel row for selected frames. The x-axis relates to the viewing direction of each pixel relative to the sun, while the LOS azimuth for each frame is color coded.

6 Laboratory measurement results

6.1 Overview of effects with first stray light measurements

The results of the first stray light measurements are shown in Figure 6.1 and 6.2. There, the detector images of the chopper signal are shown for ITC values 47 and 20. Generally, both figures show the same effects. Due to the shorter integration time in Figure 6.1, weaker effects are not visible but the images where the blackbody is within or close to the FOV are not overexposed. In Figure 6.2 it is vice versa: The images where the blackbody is within or close to the FOV are overexposed, but weaker effects become visible. It has to be noted that the colorbar of these images is adjusted for each frame separately to make stray light effects of different intensity best visible.
This brief overview makes a wide variety of stray light effects visible: The horizontal measurements show two ghosts on the left and right of the blackbody image. The left ghost image has 8.1% of the main image intensity, the right one 3.2%. They are caused by multiple reflections within the wedged beam splitter.
A third ghost is only visible in the vertical measurements of Figure 6.2. This ghost moves in the opposite direction of the blackbody image: At a blackbody elevation of $-2°$ the blackbody image is at the bottom of the frame while the ghost is at the top. In the following frames, the blackbody moves upward, while the ghost image moves downward. This ghost is likely caused by double passing through the interferometer and has an intensity of 1.1% to 1.6% depending on its position.
Another ghost-like effect can be observed at blackbody elevations above 6°. It has only an intensity of 0.014% at an elevation of 6°, but is still uncommon as such effects are not expected to be this far away from the FOV. Depending on the elevation angle, the effect is more spot-like or spreads over a bigger area of the detector.
Another effect that also occurs far from the FOV is visible at azimuth angles bigger than 6°. There the right edge of the detector image receives 80% more signal than the left side. This effect is a spot surrounded by a wider field of more radiation so it is likely caused by reflections somewhere.
Aside from concentrated stray light effects, many frames show enhanced stray light at the edges that are oriented towards the blackbody.
To get a first impression of the amount of radiation that reaches the detector from different angles, each of the detector images from Figures 6.1 and 6.2 is averaged and plotted with respect to its angular position. The results along the azimuth and elevation axis are shown in Figure 6.3. At first, the data with ITC$=20$ are not valid within or close to the FOV due to overexposing, as seen in the previous figures. The ITC$=47$ curves do not reach 1 at peak intensity because all measurements are normalized to the brightest pixels that look right onto the blackbody source as described in Chapter

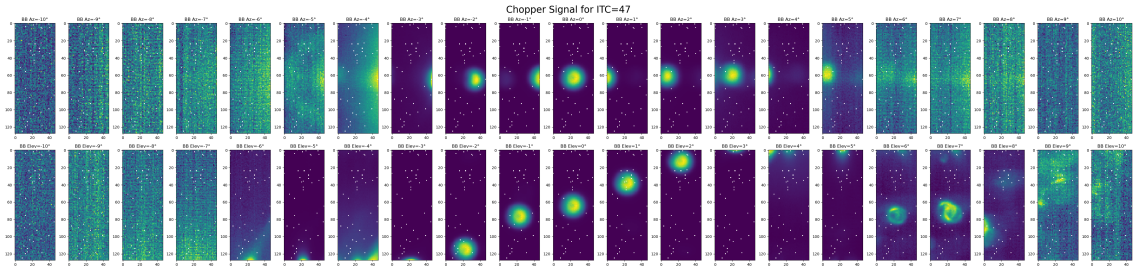

Figure 6.1: Chopper signal of the first stray light measurements with ITC=47. The upper row shows the detector images for the measurements from $-10°$ to $10°$ azimuth with an BB elevation of $0°$.The second row shows the measurements with blackbody elevations from $-10°$ to $10°$ at $0°$ azimuth. The colours are optimized for each frame to show the effects as good as possible, so a comparison between different images is not possible here.

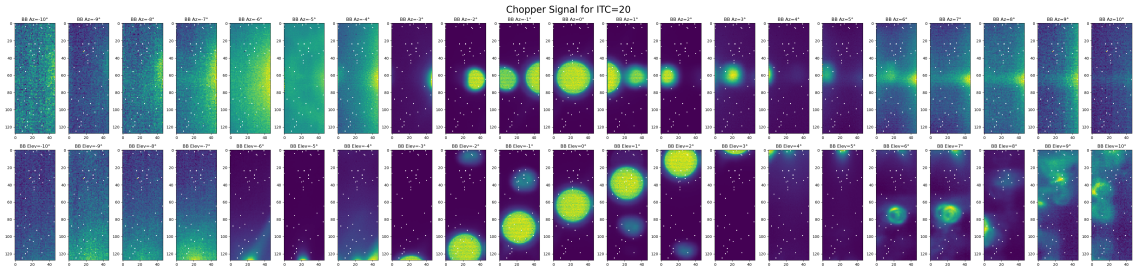

Figure 6.2: Chopper signal of the first stray light measurements with ITC=20. The frames are arranged in the same way as in Figure 6.1. The colours are optimized for each frame to show the effects as good as possible, so a comparison between different images is not possible here. The images in the middle of each row show the area around the blackbody as overexposed. This is easy to see as the overexposed area shows a typical pattern of horizontal stripes, caused by the ADC electronics.

4.5.1. As not all pixel of the detector look directly into the blackbody, they have a value < 1 and thus the mean over all pixels is < 1. The curves for both integration times show good agreement over a wide angular range and several orders of magnitude. In the horizontal plot, the area that is affected by the ghosts around the FOV is easy to see. It is followed by a rapid decline. At the edges of the measurement area, signal in the order of 10^{-6} is still detected. Looking at the vertical measurements, the larger area of peak values in the middle is noticed first. This is caused by the larger vertical FOV that covers multiple measurement positions, compared to the horizontal FOV. Second, the vertical measurements show significantly more asymmetry than the horizontal ones. This is caused by ghost-like effects above an elevation of $+6°$, that were mentioned previously. For negative elevation angles, similar to the horizontal measurements, the values decrease to 10^{-6}.

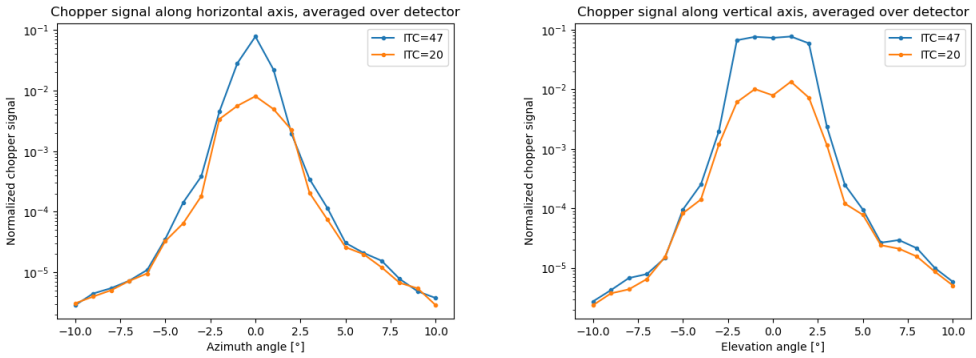

Figure 6.3: Chopper signal averaged over the entire detector image for each measurement. The left plot shows the measurements along the horizontal azimuth axis, the right plot shows the measurements along the vertical elevation axis. The ITC= 20 data within and close to the FOV are not valid due to overexposing.

6.2 Reproduction of in flight effects during gondola rotation

In this chapter, the measurements that tried to reproduce the effects seen during the uncontrolled rotation of the gondola described in Chapter 5.2 are analysed. In Figure 6.4 the results for the three different elevation angles $3°, 3.7°$ and $4°$ are shown. They are represented in the same way as in Figure 5.7: Each horizontal line is the upper row of the detector image of a measurement. All rows are aligned according to their position relative to the blackbody, which is plotted on the x-axis. The y-axis shows the measurement number from 0 which equals $-3.5°$ azimuth to 14 which equals $3.5°$. For better representation of the values that range over multiple orders of magnitude, the natural logarithm of the actual chopper signal is shown here.

When comparing the results with the flight results in Figure 5.7 it is apparent that the measurements at $3°$ blackbody elevation reproduce the in-flight effects best. The other two measurement series to not show the structure with three moving spots. They will not be considered further.

So in terms of general structure and behaviour relative to the source, the $3°$ measurement shows good agreement with the flight measurement. The intensity distribution of the lab measurements is shown in Figure 6.5. The data are represented similar to the flight data in Figure 5.11. This representation shows that the spot on the left side is more intense than the one on the right side. The spot in the middle is the most intense. The left spot has 9.5% intensity, compared to the main spot, the right spot has 1.8% compared with the main spot. When looking at Figure 6.5 it becomes apparent that the movement of the main spot is centred around$0°$ azimuth. The maximum of the main spot and the maximum of one of the side spots are visible together in one measurements, for azimuth angles $-1°$, $-0.5°$, $0.5°$ and $1°$. This provides the possibility to measure the distance between the spots directly. For the left spot this leads to a distance to the main spot of 37 pixels and for the right spot the distance is 36 pixels.

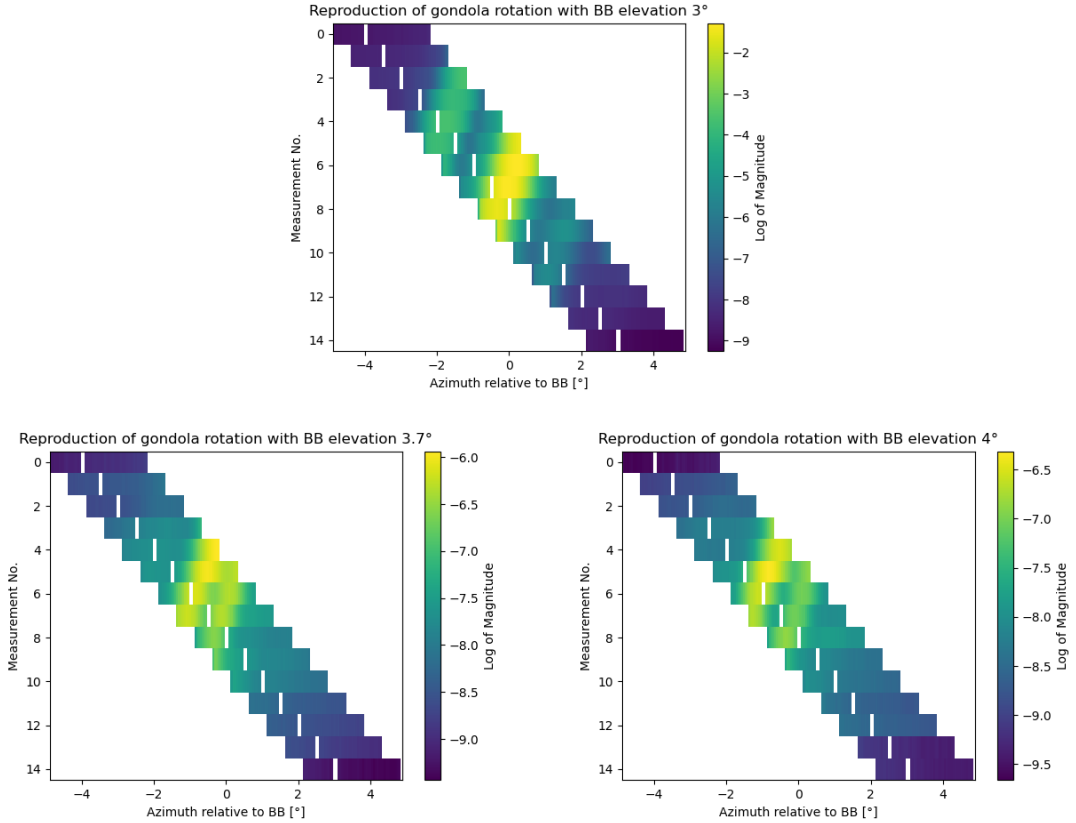

Figure 6.4: Results of the measurements that tried to reproduce the effects seen during the gondola rotation in flight. The data are represented in the same way as in Figure 5.10. To increase visibility of the stripes, the colorbar is logarithmic. The upper image shows the results for an blackbody elevation of 3°, the image on the left for 3.7° and the right image for an elevation of 4°

.

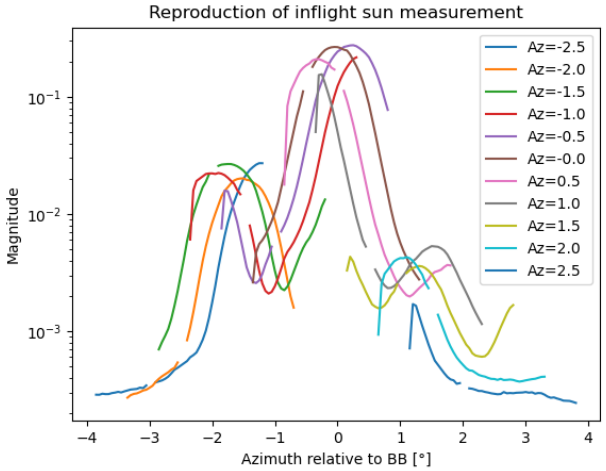

Figure 6.5: Intensity distribution of the upper pixel row for all frames between −2.5° and 2.5° with blackbody elevation 3°. The x axis relates to the viewing direction of each pixel relative to the blackbody, while the LOS azimuth is color coded. This figure represents the measurement data in the same way as Figure 5.11 does for the flight data.

6.3 Effects of interferometer carriage position

This chapter describes the effect of the position of the interferometer carriage onto stray light and shows the results of the measurements described in Chapter 4.3.3. In Figure 6.6 the results of four selected measurements are shown. The top left image shows a stray light effect at an azimuth angle of $-10°$. This effect was not visible in Figure 6.1 and 6.2 and thus was not mentioned yet. The effect only occurs at OPD positions close to maximum OPD and changes its side depending on the carriage position. The top right image shows the same stray light effect at $-6°$ azimuth. There it is only visible at reference position 5.2 but does not show up on the other side of the image at reference position 5.4. The lower left image shows an effect that occurred several times at different reference positions during the measurements: At reference position 5.4 almost no signal at all is detected. This happens, because by accident the interferometer was set to an OPD position that produces almost perfect destructive interference. As the reference positions are set by hand for each of the measurements, it is likely that such a position is hit by now and then. This affects the measurements at $-9°$, $-8°$, $-4°$, $6°$ and $8°$.

6.4 Detailed analysis of a selected stray light effect

This chapter shows the results of the additional measurements described in Chapter 4.3.4. The goal of these measurements is to investigate the stray light mechanisms of the ghost-like reflection that occurs when the blackbody is placed more than $6°$ above the LOS.
In these measurements, the blackbody elevation ϕ_{BB} and the elevation of the LOS are varied. This results in the same scene under the same relative angles β between LOS and blackbody for different blackbody elevations and different scanning mirror angles. The results are shown in Figure 6.7. It can be seen, that the vertical position of the ghost reflection is mainly controlled by β while the general appearance, whether it is more spot-like or more diffuse, seems to be determined by ϕ_{BB}. The peak intensities range from 1.6×10^{-5} to 3.5×10^{-4}, depending on the setting for β and ϕ_{BB}.
In the following measurements different parts of the instrument are covered with cardboard or foam as described in Chapter 6.4. The aim is to check whether these changes have an effect onto the observed reflection. In Figure 6.8 a modification with an additional stop between POM and IFMS is shown. The photo on the left shows the actual modification, where the stop can be seen twice: On the right side of the entrance aperture and on the left in the image of the scanning mirror. The stop is designed to be as small as possible but not to block the designed optical path. On the right side the horizontally averaged chopper signal is shown for $\beta = 6°, 7°, 8°$. For comparison, the results without any modification are labelled as β_{ref} while the results with modification are labelled β_{test}. This representation is the same for all following modifications. It can be seen, that the stop reduces the intensity of the ghost at all measurement positions, compared to the results without modification. The shape of the results are barely affected.
Figure 6.9 shows a modification of the beam splitter unit (BSU). There, the surfaces above and below the retroreflectors are covered with cardboard pieces as shown in the photo on the left. The results show a reduction in intensity for $\beta = 6°$ and $\beta = 7°$, there the shape of the results is not

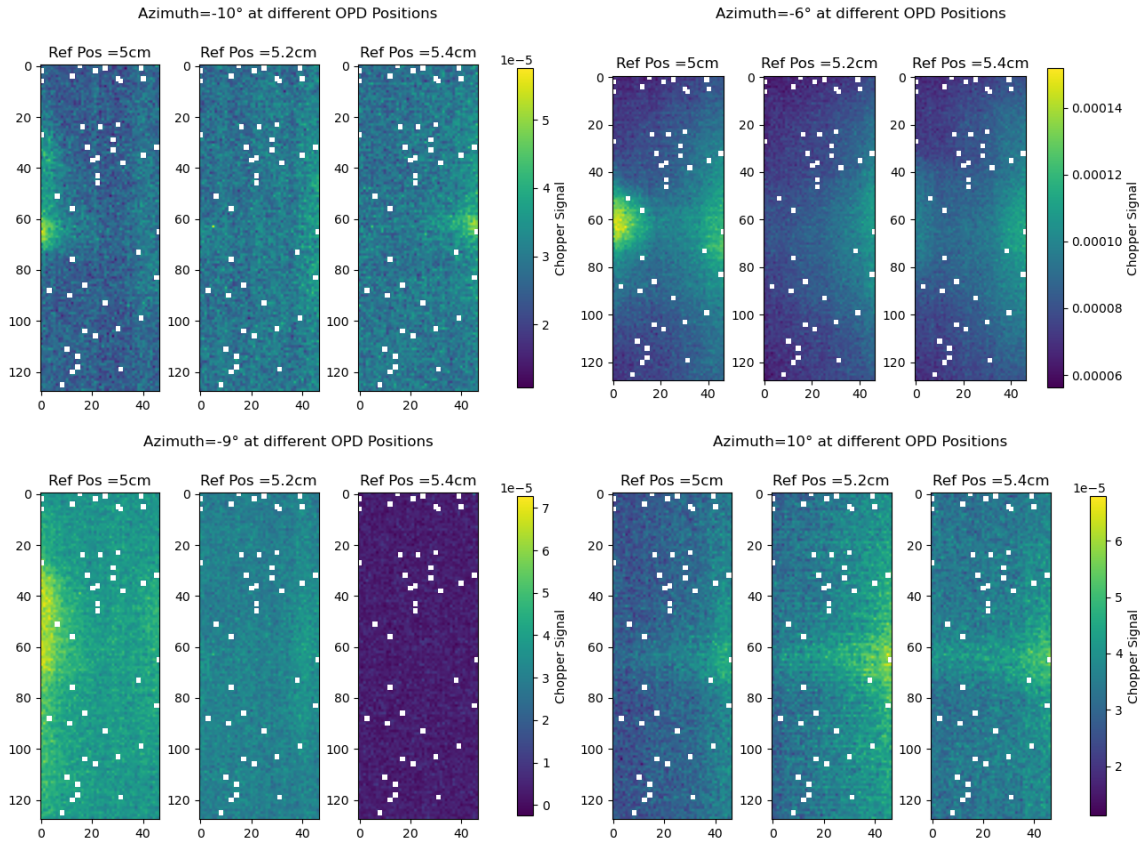

Figure 6.6: Comparison of chopper signal for different interferometer carriage positions for selected azimuth angles relative to the BB. The Ref Pos refers to the reference position of the interferometer carriage described in Chapter 4.3.3. The top left image shows a stray light effect at $-10°$ azimuth angle that changes the side on the detector image depending on the carriage position. The top right image shows the same stray light effect at $-6°$ azimuth, there the spot on the left side vanishes but it does not appear on the right side of the image. The lower left image shows an effect that is seen sometimes during measurement: reference position 5.4 has no signal at all because by accident, a OPD position causing almost perfect destructive interference is set. The lower right image shows the stray light effect at $10°$ azimuth, that were discussed in Chapter 6.1. There almost no effect of the carriage position is seen.

changed by the modification. For $\beta = 8°$ no effect of the modification can be observed.

In addition to the previous modification, in Figure 6.10 the beam splitter mounting around the beam splitter is also covered with cardboard. The results are shown on the right side of the figure. The modification only has an effect on the result at $\beta = 6°$. There, all values are significantly lower but not changed in shape, compared to the result without modification.

For Figure 6.11 the previous modifications are still in place. In addition the rotating cylinder of the POM is modified. There, the base surfaces are covered with black foam as visible in the photo on the left side. The results on the right side show a decrease in intensity and a change of the shape for all scenes.

A further modification is shown in Figure 6.12. There, the entrance aperture is reduced to a diameter of 35 mm. In addition the modifications from Figure 6.10 and Figure 6.11 are still in place. The results on the right show a reduction in intensity that depends on β. Also the shapes of the reflection are altered differently.

Figure 6.13 shows a modification that is based on Figure 6.13. Here, additional surfaces on the left

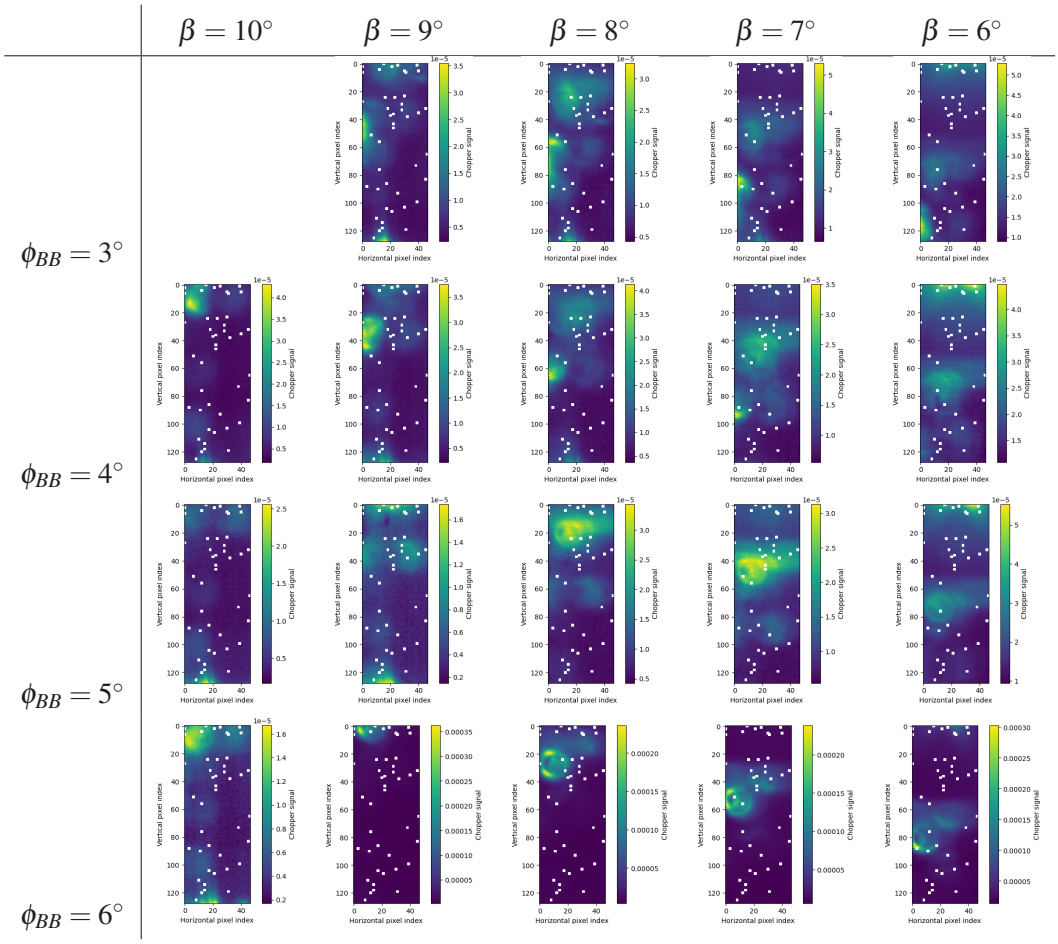

Figure 6.7: Detector images of the ghost-like reflections that occur when the detector is placed more than 6° above the LOS for different blackbody elevations ϕ_{BB} and LOS angles. The angular distance between the LOS and the blackbody is represented by β.

of the BSU are covered with cardboard. The results in the plot on the right side show a reduction of the chopper signal and a change of the shape for all measurement positions, compared to the results without modifications.

6.5 Quantitative stray light behaviour (PST)

The previous sections focused on the results of certain types of measurements and selected effects. This section focuses on a quantitative description of the stray light that reaches the detector from certain directions. Therefore, the elevation and azimuth dependent point source transmittance (PST) is determined from the measurements described in Chapter 4.3.5. The PST as defined in Chapter 2.4.1 is the irradiance at the focal plane caused by stray light divided by the irradiance incident at the aperture. That definition is not useful, as the measurement principle used provides neither the irradiance at the focal plane nor at the aperture. So, the definition is adapted in order to use the amplitude of the chopper signal detected at the focal plane divided by the amplitude of the brightest pixels that look right into the source. This is the same principle all previous measurements have

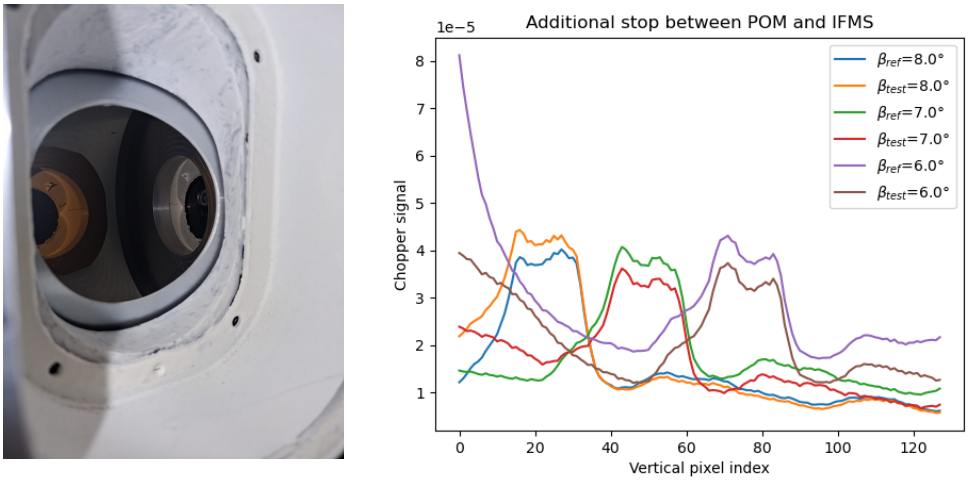

Figure 6.8: The left image shows an additional stop between POM and IFMS as modification to check whether this reduces the ghost reflections when the BB is placed more than 6° above the LOS. The plot on the right side shows the horizontal mean across the detector image with and without the modification where β is the angle between the LOS and the blackbody. The subscript *ref* designates the reference measurements without modifications, the subscript *test* designates the measurements with modifications. All measurements are taken with the blackbody placed at $\phi_{BB} = 6°$.

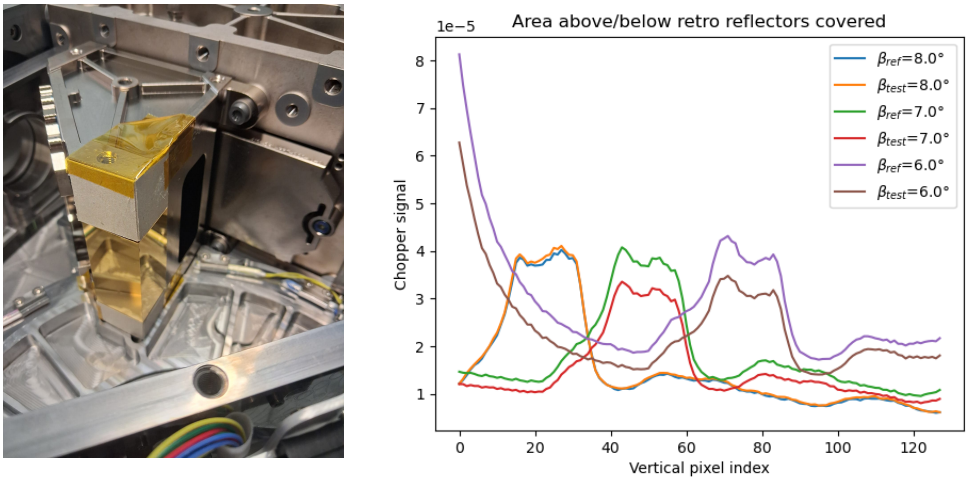

Figure 6.9: In the left image, the areas above and below the retroreflectors on the BSU are covered with cardboard to check whether this changes the intensity of the ghost. The plot on the right side shows the results with and without the modification. The representation and all parameters are the same as described in Figure 6.8.

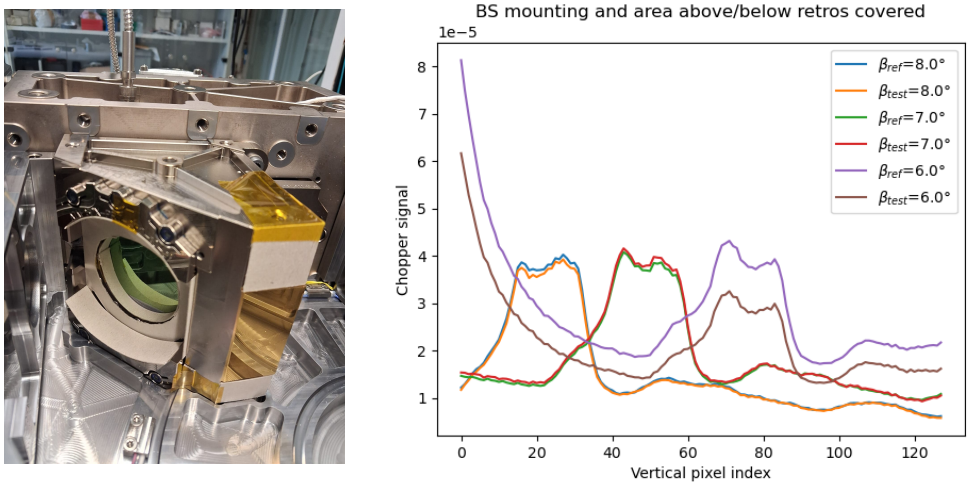

Figure 6.10: In addition to the modification from Figure 6.9 here the beam splitter mounting is covered with cardboard as shown in the left image. The plot on the right side shows the results with and without the modifications. The representation and all parameters are the same as described in Figure 6.8.

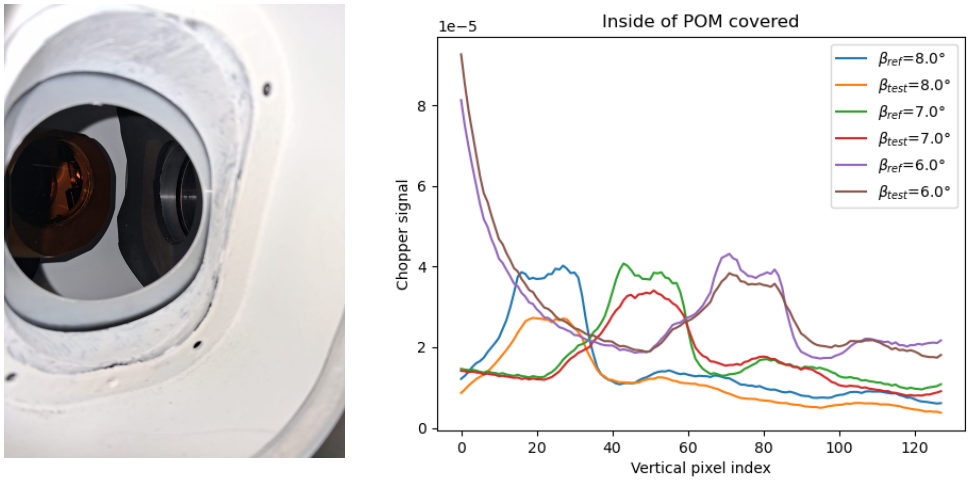

Figure 6.11: The image on the left side shows a modification of the rotating drum of the POM. There the base plates of the cylinder are covered with black foam to reduce reflections. The modifications from Figure 6.10 are still in use. The plot on the right side shows the results with and without the modification. The representation and all parameters are the same as descibed in Figure 6.8.

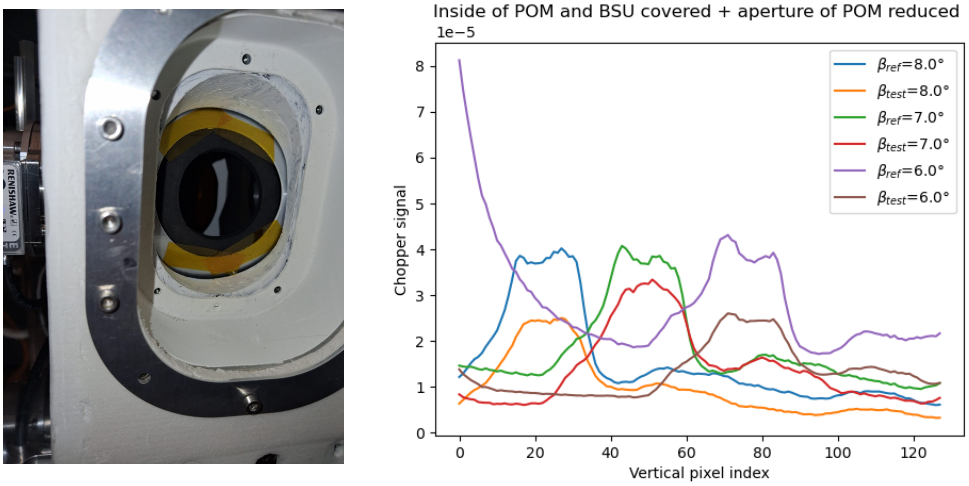

Figure 6.12: In addition to the modifications shown in Figure 6.11 here the entrance aperture of the POM is reduced to a diameter of 36 mm. The modifications from Figure 6.10 are still in use. The plot on the right side shows the results with and without the modifications. The representation and all parameters are the same as described in Figure 6.8.

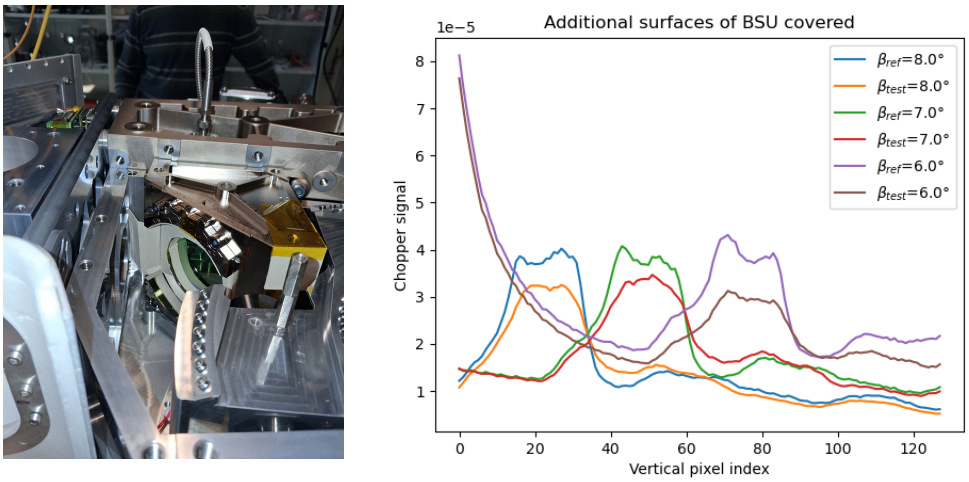

Figure 6.13: In addition to the modifications shown in Figure 6.10, the area to the left of the beam splitter mounting is also covered with cardboard as shown in the image on the left side. The results with and without the modification are shown in the plot on the right side. The representation and all parameters are the same as described in Figure 6.8.

been normalized as described in Chapter 4.5.1. This allows to relate the chopper signal at any point to the generated chopper signal. The altered PST reads as:

$$PST(\phi,\theta) = \frac{A_{SL}}{A_{Ch,max}} \tag{6.1}$$

where A_{SL} is the amplitude of the chopper signal at the focal plane and $A_{Ch,max}$ is the amplitude of the brightest pixels. Elevation and azimuth angles are represented by ϕ and θ.

To calculate the PST for the entire detector image, the normalized detector signal is averaged across the detector for each measurement position. The result for all measurement positions in the range from -10° to 10° in azimuth and elevation is shown in Figure 6.14. The plots show the amount of radiation that reaches the detector from a given direction. As discussed previously, the average over the entire normalized detector image is always below 1 because the detector is never fully illuminated. This leads to an underestimation of the amount of radiation within the FOV. For better results, the entire detector image should have been illuminated by the blackbody when placed right in front. The four missing pixels at 9° elevation in each following PST image were caused by an error when performing the measurement. Thus, these measurements cannot be reliably assigned to the corresponding positions. The patterns of 2-5 pixels with significantly lower values than the surrounding pixels are likely caused by false detections of the chopper frequency that could not be corrected by the algorithm.

For the integration times, the same problems as in all previous measurements apply also here: ITC$=47$ provides good results within or close to the FOV, while ITC$=20$ provides more sensitive results far away from the FOV. At intermediate angular distance both measurements agree. This leads to the idea of a continuous join to provide reasonable and sensitive results at any point within one PST image. A cross section of both integration times and the continuous join of both at 0° elevation is shown in Figure 6.15. This shows that it is possible to join both PSTs continuously to generate one PST with sufficient sensitivity at large angles and without adverse effects caused by overexposing within the FOV. Both PSTs are joined at the 5° frame. Outside, the data with ITC$=20$ are used, inside of the 5° frame the data with ITC$=47$ are used. The continuously joined result is shown in Figure 6.16. This PST shows a lot of the features mentioned before: The ghost effects close to the FOV, visible by enhanced values to the left and right of the FOV, the reflections at large positive azimuth angles, visible by a slight asymmetry along the azimuth axis and the ghost-like reflections above 6° azimuth angle by enhanced values in that area compared to the same area at negative elevation angles.

Due to averaging over the entire detector, most of the vertical structure is lost. For further investigation of the stray light effects it is reasonable to average not over the entire detector but over horizontal pixel rows to increase vertical resolution. This generates a elevation and azimuth dependent PST for each detector pixel row, showing the amount of light reaching the corresponding pixel row out of the angular space. As this leads to 128 PST plots, only three for the pixel rows 0, 64 and 127 are shown in Figure 6.17. This shows now that a pixel row receives the most radiation from an elevation angle that corresponds to the position of the pixel row within the FOV: A pixel row on the upper edge of the detector will receive more light from the upper edge of the FOV. The same is valid for pixel rows in the middle or the bottom of the FOV. As expected, this kind of PST resolves the vertical structure way better than the average over the entire detector, thus the

effect of the vertical ghost becomes visible. For detector pixel row 0 it is visible by two slightly brighter pixels of the PST at $-2°$ elevation. A beam incident from $-2°$ will produce a ghost image at detector pixel row 0, thus more radiation reaches the corresponding detector pixels at that row. The principle for detector pixel row 127 is the same. For detector pixel row 64 the ghost image only illuminates these detector pixels when the beam is incident at $0°$. Thus the image of the beam and the ghost image add up, leading to higher PST values than in the other pixel rows. This figure also shows that the angular area from which a significant amount of radiation reaches the detector pixels covers several degrees and is slightly dependent of the position of the detector pixel row. In that area, the values are above 10^{-4}.

For level 2 processing of the measured atmospheric data, pixels of the cubes are aggregated horizontally. Thus, the horizontal resolution is lost. As the horizontal structure of the PST does not affect the results of the level 2 data, the PST can also be integrated along the azimuth axis. By doing so, a vertical PST profile is generated for each detector pixel row. Each profile shows the amount of radiation that reaches the given detector pixel row from a certain elevation level. In Figure 6.18 the PST profiles for the pixel rows 9, 64 and 127 are shown. As already discussed, the elevation from which the most radiation reaches the detector pixels depends on the position of the detector pixel row. For detector pixel rows in the upper half of the detector image above row 64, ghost effects are visible at elevations between $-3°$ and $0°$. For detector pixel rows in the lower half of the detector image below row 64, the ghost effects are visible at elevations between $0°$ and $3°$. Most radiation reaches the detector from elevations between $-4°$ and $4°$. Outside of that elevation range, the PST values drop below 10^{-3}, reaching values lower than 10^{-4} at elevation angles greater than $\pm 8°$. Thus, the amount of radiation reaching the detector pixels from that elevation range is low.

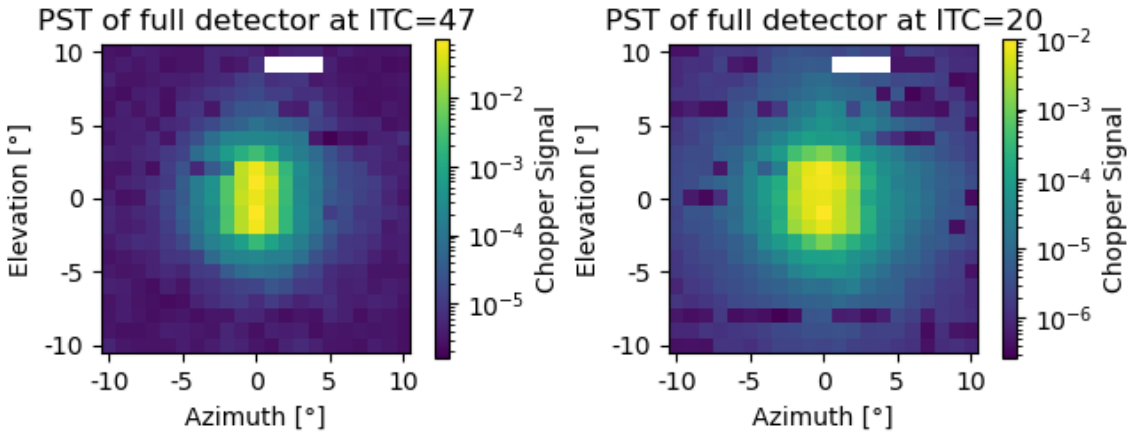

Figure 6.14: Point source transmittance of the entire detector image dependent on the position of the source. Each pixel in the plots represents the amount of radiation that reaches the detector from a certain direction in azimuth and elevation. The left image shows the PST calculated only out of the measurements with ITC value 47. The right plot shows the PST calculated from the measurements with ITC value 20. The four white pixels are excluded measurements.

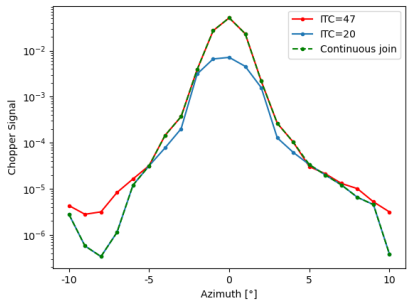

Figure 6.15: Cross section of the PSTs for both ITC values and their continuous join at 0° elevation.

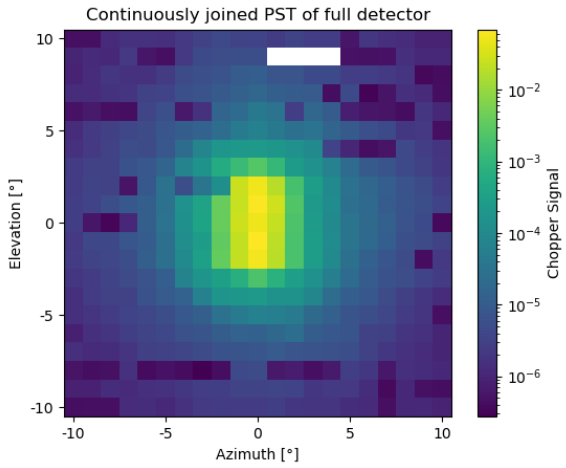

Figure 6.16: Continuously joined PST out of data with ITC value 47 close to the FOV and ITC value 20 beyond a 5° frame. The pixels in the image represent the amount of radiation that hits the detector pixels from a certain direction in azimuth and elevation.

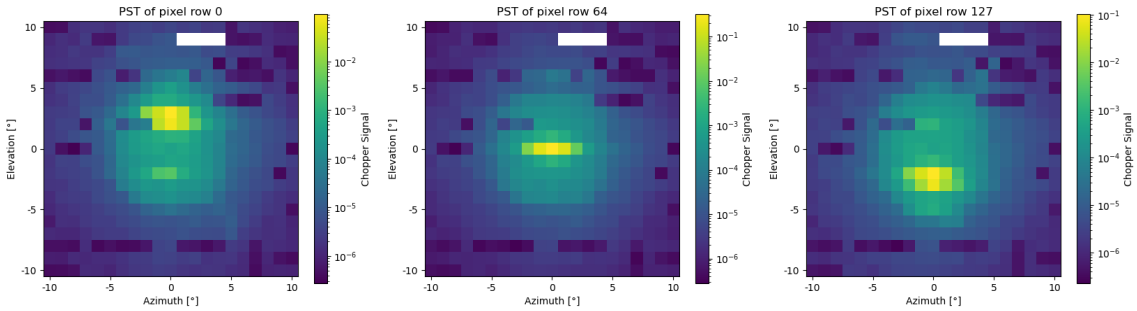

Figure 6.17: PSTs of the corresponding detector pixel rows. Here each pixel shows the amount of light that reaches the given detector pixel row from a certain direction. Thus more structure is visible compared to the PSTs in Figures 6.1 and 6.14.

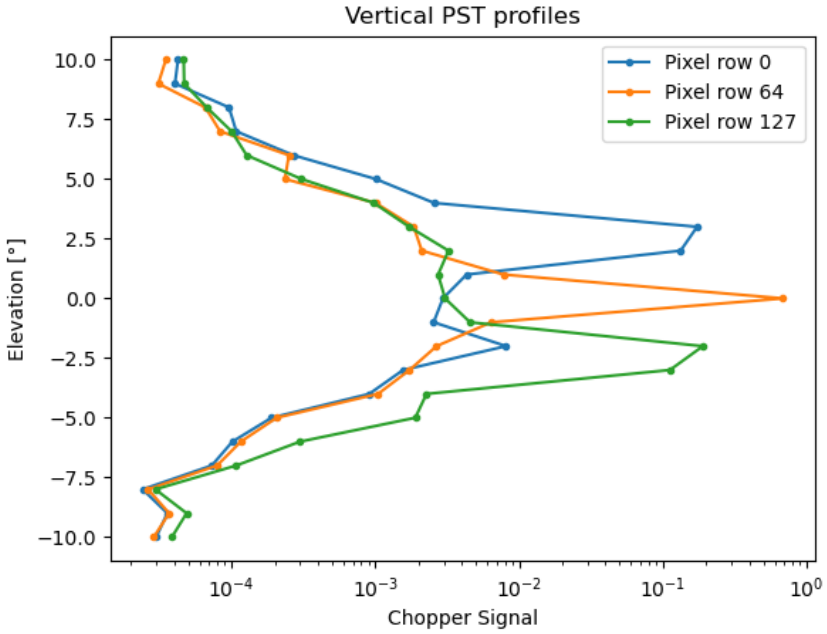

Figure 6.18: The vertical PST profiles here are the horizontally integrated PSTs from Figure 6.17 for the detector pixel rows 0, 64, and 127. The curves represent the amount of radiation that reaches the given detector pixel row from a certain elevation level.

7 Discussion

7.1 Flight data

7.1.1 Limitations and uncertainties

The factor that limits the quality of the flight data most is the quality of the pointing data. An analysis performed by (G. Maucher, personal communication,2025) compared the attitude data of the inertial measurement unit of GLite with the attitude data provided by CNES. The differences for pitch (elevation), roll and yaw (azimuth), angles are shown in Figure 7.1. This shows that the offsets of pitch and roll drift a bit in time and are are generally small. The roll angle shows an offset that is mostly between $0°$ and $-0.2°$, while the pitch offset mainly ranges between $-0.4°$ and $-0.6°$. This leads to a temporal mean of $-0.46°$ for pitch. Compared to that, the yaw offset is unstable and not continuous. It ranges between $-4°$ and $4°$ and is therefore one order of magnitude larger. The mean offset for the yaw angle is $-1.16°$.
Another analysis of the LOS elevation provided by (S. Johansson, personal communication,2025) compares the measurements with simulated radiances calculated from atmospheric model data. This leads to an average offset of $-0.6°$ for the elevation of the LOS. This corresponds to the average offset of $-0.46°$ for the pitch angle from the CNES data.

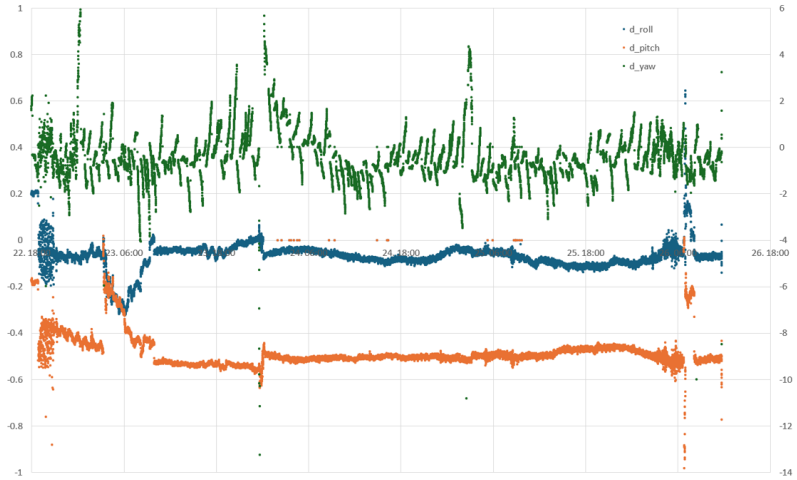

Figure 7.1: Offset angles for pitch (orange), roll (blue) and yaw (green) during flight. Roll and pitch refer to the left y-axis, while yaw refers to the right y-axis. The offsets are generated by comparing the attitude date from the internal inertial measurement unit of GLite with the attitude data provided by CNES. Plot by G. Maucher.

7.1.2 Operational measurements

The analysis of the operational measurements showed that measurements that look deeper into the atmosphere detect more radiation at the same point in the atmosphere than measurements at higher elevation angles. This is consistent with expectations, as deeper layers in the atmosphere are more radiant. Thus, the background scene at deeper levels has more radiance and any stray light process will bring more radiance to the detector. The mean of the vertical difference profile provides an estimate for the amount of stray light that reaches the upper part of the detector. Depending on the position at the detector, the stray light effects are in the order of $5\,\mathrm{nW/cm^2\,sr\,cm^{-1}}$. Despite the relatively large standard error of the mean, these results are considered consistent as the mean itself has no big variation.
The small angular space covered by these results limits the significance for the whole instrument. First, these data could only be generated in the region where both FOVs overlap, which are only the upper 36 pixel rows of the detector. Second, these data are only available for the two elevation levels discussed. Thus, the area of overlap always sees the same background scene. Variations in the background scene and different areas of overlap would have provided more variety and could have exhibited more of the stray light behaviour during flight. In addition, the limited quality of the elevation data has to be considered. Variations in the LOS elevation angle can lead to slightly different overlap angles and thus degrade the vertical resolution of the results.

7.1.3 Stray light effects during rotation of the gondola

The rotation of the gondola during flight exposed some strong stray light effects when the FOV was close to the sun. The analysis showed three bright spots at the upper edge of the detector image. Over time, the spots moved in the opposite direction of the rotation. This speaks for a source that is fixed in space as the sun is. When relating the movement to the position of the sun, the results showed that the movement of the main spot is not centered relative to the sun. The movement seems to be centered to an azimuth position of -0.7° relative to the sun. At this point that speaks against the sun as the source. At this point, the previously discussed uncertainty of the pointing has to be considered. The average offset of the yaw angle is -1.16° but shows a large variation. It has to be noticed that the quality of the azimuth data is not validated for that time period, mainly because there are no data from CNES to compare with the data of GLites internal inertial measurement system. Following this, the sun can be considered as radiation source of the observed stray light. This analysis showed that the optical system of GLite has stray light effects that become visible when a strong source as the sun is close to the FOV. It can be expected that these effects also occur without a strong source, but they may be not that easy to find. An explanation of these effects could not be provided, so further investigation with lab measurements is necessary.

7.2 Lab measurements

The lab measurements provided the possibility of measuring the the stray light caused by a source isolated from background radiation in a controlled environment.

7.2.1 Limitations and uncertainties

The measurement and adjustment accuracy of the blackbody elevation ϕ_{BB} and the azimuth of the LOS θ is determined by the reading accuracy for the corresponding scale. The azimuth can be determined directly on a 0.25°-scale as shown in Figure 4.6. Thus, the uncertainty for the azimuth is considered to be half the scale width, so $\Delta\theta = 0.125^\circ$. The blackbody elevation is given by:

$$\phi_{BB} = arctan(h/L) \tag{7.1}$$

Thus, the uncertainty is controlled by the uncertainties of h and L. The height h is determined by a pocket rule and a cross line laser. For this method, $\Delta h = 1\,\text{mm}$ is assumed. The distance is also determined by a pocket rule but as the measurement is more prone to errors, $\Delta L = 0.5\,\text{mm}$ is assumed. By applying error propagation for uncorrelated errors leads to $\Delta\phi_{BB} = 0.07^\circ$.
Another effect that affects the quality of the measurements and especially the image quality is the usage of an uncollimated source. The optics of GLite are designed to generate good images for incident radiation with parallel rays. The blackbody is not collimated and quite close to the instrument thus the image of the blackbody is out of focus. However, this affects only measurements, where the blackbody or a ghost image is directly imaged onto the detector. Stray light caused by diffraction and reflections somewhere is naturally out of focus, thus the uncollimated light has no effect.
Another source of errors is the processing algorithm described in Chapter 4.5.1. As the chopper frequency is determined by finding the maximum within a given frequency range, this leads to an artificial increase of the signal in cases where the signal-to-noise ratio is low. The strongest deviations caused by false detections, but not all deviations from the unknown true chopper frequency can be corrected. Measurements where the chopper signal is significantly stronger than the background noise are not affected by this issue.
The last limitation discussed is caused by the condition of the instrument during the measurements. The interferometer was inoperable and thus the radiation was not modulated. The lab measurements cannot distinguish whether a stray light effect is modulated by the interferometer or not. Effects that are modulated would be present in the level 1 and 2 data and thus affect the level 2 products directly. Stray light effects that are not modulated are removed during the level 1 processing and thus do not affect the level 2 products. These effects still illuminate the detector and block a part of its dynamic range. So, that kind of stray light reduces sensitivity and increases noise without being visible in the processed data.

7.2.2 Beam splitter ghost effects in theory and lab measurements

Theoretical calculation of position and intensity

The ghost effects to the left and right of the source are caused by single and double reflections within the wedged beam splitter. The different light paths that cause these ghosts are shown in Figure 7.2. The theoretical derivation of the ghost position and intensity was performed by (Sha, 2013) and is adapted for the new BS of GLite here.
The beam splitter is made of an artificially grown CVD Diamond coated with germanium as beam splitting material. Starting from the atmospheric port, the light passes four layers of media, air, the germanium coating, the beam splitter diamond with anti-reflective coating, and again air. The refractive indices of the four media are: $n_1 = n_4 = 1$ (air), $n_2 = 4$ (germanium) and $n_3 = 2.38079$ (diamond).
For the beam splitter wedge angle θ the manufacturer has provided two conflicting values:
$\theta_1 = 10.79' = 3.1387 \times 10^{-3}$ rad or $\theta_2 = 12.5' = 3.636 \times 10^{-3}$ rad (F. Friedl-Vallon, personal communication, 2025). The different angles of the beams caused by reflection and refraction are shown in Figure 7.2 and are calculated with angle of incidence α_1 as follows:

$$\alpha_2 = arcsin\left(\frac{n_1}{n_2} sin(\alpha_1)\right) \tag{7.2}$$

$$\alpha_3 = arcsin\left(\frac{n_2}{n_3} sin(\alpha_2)\right) \tag{7.3}$$

$$\alpha_4 = arcsin\left(\frac{n_3}{n_4} sin(\alpha_3 + \theta_i)\right) \tag{7.4}$$

$$\alpha_5 = arcsin\left(\frac{n_3}{n_4} sin(\alpha_3 - \theta_i)\right) \tag{7.5}$$

$$\alpha_6 = arcsin\left(\frac{n_3}{n_4} sin(\alpha_3 - 3\theta_i)\right) \tag{7.6}$$

The angular distance between the ghosts and the main image is given by D_1 and D_2 as follows:

$$D_1 = \alpha_5 - \alpha_4 \tag{7.7}$$

$$D_2 = \alpha_5 - \alpha_6 \tag{7.8}$$

During the measurements, the incident angles were $\alpha_1 = 45° \pm 1°$. The distance in pixels P_i is calculated by using the pixel size in the angular space $pix = arctan(d/f)$, with the focal length $f = 57\,\text{mm}$ and the pixel pitch $d = 0.03\,\text{mm}$. The results are given in Table 7.1. Depending on which wedge angle is true, the results differ substantially.

The intensities of the images are determined by the reflectance and transmittance coefficients of the surfaces within the BS. Because the coefficients of the different surfaces are unknown, they are treated as two surfaces with coefficients T_1, R_1 and T_2, R_2. Their values are taken from the transmittance curve of the BS and the reflectance curve of the diamond with AR coating, both provided by the manufacturer (Ltd, 2022). By following the paths of the beams through the

	$\theta_1 = 10.79'$				$\theta_2 = 12.5'$			
α_1	D_1	D_2	P_1	P_2	D_1	D_2	P_1	P_2
44°	−1.14°	1.12°	−37.75	37.12	−1.32°	1.29°	−43.73	42.90
45°	−1.16°	1.14°	−38.34	37.67	−1.34°	1.31°	−44.42	43.52
46°	−1.17°	1.15°	−38.96	38.24	−1.36°	1.33°	−45.14	44.18

Table 7.1: Positions of the ghost images relative to the main image in angular distance (D_i) and pixel distance (P_i) for different wedge angles θ_i and incidence angles α_1.

materials, the intensities of the main image (I_m), the first ghost image (I_{1m}) and the second ghost image (I_{2m}) are given by:

$$I_m = R_1 T_1 T_2 + R_1 T_1 T_2^3 + 2R_1 T_1 T_2^2 \tag{7.9}$$

$$I_{1m} = R_2 T_1 T_2 + R_2 T_1 T_2^2 + 2R_2 T_1^2 T_2 \tag{7.10}$$

$$I_{2m} = R_1^2 R_2 T_1 T_2 + R_1^2 R_2 T_1 T_2^3 + 2R_1^2 R_2 T_1 T_2^2 \tag{7.11}$$

As the interferometer was not moving, only the DC parts of the intensities are considered. The ratios of the intensities are calculated as I_{1m}/I_m and I_{2m}/I_m. For $T_1 = 0.45$, $R_1 = 0.55$ and $T_2 = 0.94$, $R_2 = 0.06$ the results read as:

$$I_m = 0.8756 \tag{7.12}$$

$$I_{1m} = 0.0721 \tag{7.13}$$

$$I_{2m} = 0.02889 \tag{7.14}$$

$$\text{Ratio}_1 = 8.2320\% \tag{7.15}$$

$$\text{Ratio}_2 = 3.3\% \tag{7.16}$$

$$\tag{7.17}$$

Comparison with measured position and intensity

As all measurements are taken with a 1° spacing, the maxima of the main image and one of the ghost images are never in the same image. The maxima of the ghost images are only seen in measurements with azimuth angle ±1°. Therefore, the angular positions have to be calculated relative to the measurement at 0° azimuth, where the main image of the source is visible. This leads to:

$$D_1(\alpha_1 = 46^\circ) = \alpha_5(\alpha_1 = 45^\circ) - \alpha_4(46^\circ) \tag{7.18}$$

$$D_2(\alpha_1 = 46^\circ) = \alpha_5(\alpha_1 = 45^\circ) - \alpha_6(46^\circ) \tag{7.19}$$

$$D_1(\alpha_1 = 44^\circ) = \alpha_5(\alpha_1 = 45^\circ) - \alpha_4(44^\circ) \tag{7.20}$$

$$D_2(\alpha_1 = 44^\circ) = \alpha_5(\alpha_1 = 45^\circ) - \alpha_6(44^\circ) \tag{7.21}$$

Here, $\alpha_1 = 46°$ is equivalent to an azimuth angle of $-1°$ and $\alpha_1 = 44°$ is equivalent to an azimuth angle of $1°$. The the resulting angular distances have been simulated in Zeemax (F. Friedl-Vallon, personal communication, 2025) in order to provide the distance in pixels without errors due to distortions caused by the COP. For θ_1, the ghost image 1 is at -4.4 pixels relative to the centre of the detector, for θ_2 the image is at -12 pixels relative to the centre of the detector. Ghost image 2 is at $+5.5$ pixels for θ_1, for θ_2 the image is at $+12.5$ pixels relative to the centre of the detector.
In the measurements, ghost image 1 is located at -16 pixels, while ghost image 2 is located at $+13$ pixels relative to the centre of the detector. This shows that there is a big difference when assuming θ_1 as true. When considering θ_2 as true, The difference between the measured and expected value for ghost image 1 are 4 pixels. For ghost image 2 the difference are 0.5 pixels. Four pixels equal $0.12°$ which is in the order of magnitude assumed for the uncertainty of the azimuth setting during the measurements. As described in Chapter 4.2, a $0.25°$ scale is used to set the desired azimuth angle. Using the half scale width as uncertainty for the azimuth angle, this leads to $0.125°$ which is slightly bigger than the difference between the expected and measured ghost image position. Looking at the difficulties that arose during the analysis of the ghost images, the conflicting wedge angles, the fact that main image and ghost image are not seen in the same detector image and the usage of an uncollimated beam as in all measurements, leads to the recommendation of repeating the measurements. By adjusting the number of pixels used on the detector, it should be possible to capture the main image and the ghost image in one shot. Using a collimated source reduces blur of the image. With such measurements, it should be possible to determine the true wedge angle of the beam splitter.

The calculated ghost image intensities of 8.2% and 3.3% agree well with the measured ratios of 8.1% and 3.2%. The theoretical values are very sensitive to changes in the coefficients. When using the specified values with a BS transmittance of 0.5 and a transmittance of 0.99 for the AR coating, the ratios for the ghosts would be 1.5% and 0.5%. It is likely that the coatings do not meet the specifications perfectly, so the assumption of less transmittance for both coatings is reasonable. Regardless of the actual numbers, both measurement and theory agree that the left ghost (I_{1m}) is substantially stronger than the right ghost (I_{2m}).
Despite the difficulties when comparing the positions, it can be concluded that the ghost images to the left and right of the main image of the source are caused by multiple reflections within the wedged beam splitter. Further measurements would allow to determine the true wedge angle of the beam splitter.

7.2.3 Aperture Diffraction

The effect of aperture diffraction as described in Chapter 2.2.3 is analysed here by comparing the measurements with results of the PSF of a circular aperture:

$$E_f(\theta_i, \theta_d) = \left(\frac{\pi D^2}{4\lambda f}\right)^2 \left[2\frac{J_1(\pi D \mid sin(\theta_d) - sin(\theta_i) \mid /\lambda)}{\pi D \mid sin(\theta_d) - sin(\theta_i) \mid /\lambda}\right] \tag{7.22}$$

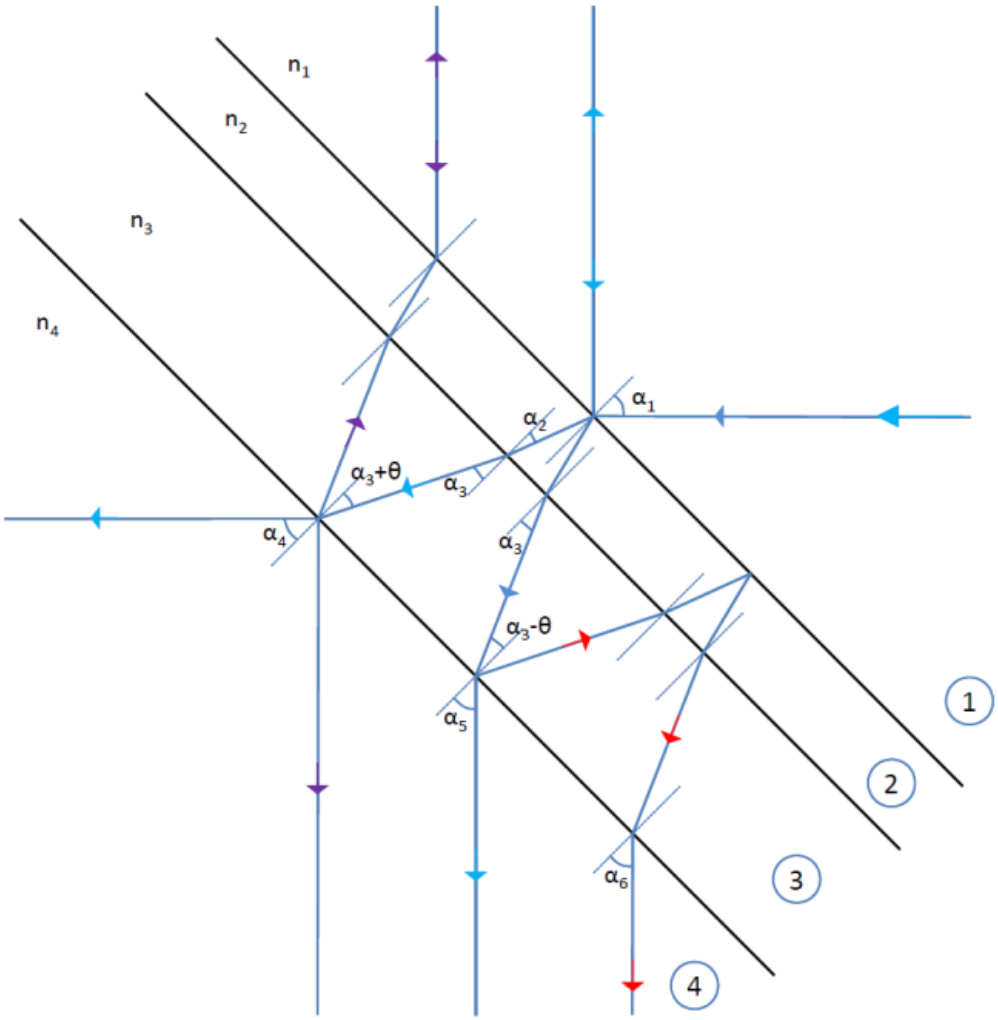

Figure 7.2: Ray propagation through the beamsplitter showing the multiple reflections and refractions that cause ghost images. The incident beam enters on the right (blue arrows), the corner cube reflector of the reflected beam (CC-R) is located at the top outside the image, so is the corner cube reflector of the transmitted beam (CC-T) on the left side. The detector port is at the bottom of the image. The reflected beams of CC-T are not relevant for the explanation, so they are not shown. The first ghost image (violet arrows) is caused by a single reflection at the rear surface of the BS, followed by a reflection at CC-R. The second ghost image (red arrows) is caused by a double reflection within the BS. The BS consists of the reflective germanium coating with refractive index n_2 and the diamond crystal with refractive index n_3. The anti-reflective coating on the rear side is missing in this representation. The air in front and behind the BS has the refractive index $n_1 = n_4$. Figure from (Sha, 2013).

The angles θ_i and θ_d are as in Figure 2.4. There θ_i is the angle at which the radiation is incident to the aperture, here it ranges from $-10°$ to $10°$. The diffraction angle θ_d ranges from $-0.708°$ to $0.708°$ which is the angular space covered by the detector. The intensity is reads as: $I(\theta_i, \theta_d) = E_f(\theta_i, \theta_d)^2$. Here, diffraction is only analysed in one dimension along the horizontal axis of the detector. For comparison with the measurement data shown in Figure 6.3, the intensity is integrated over the angular space of each pixel and then averaged horizontally. These values are then normalized with the intensity of the on axis pixel at $\theta_i = 0$.
The result, together with the measurement data, is shown in Figure 7.3. The peaks of the curves at $0°$ azimuth of theory and measurement with ITC$=47$ agree. This shows that the normalisation of the diffraction curve is consistent. The values of the ITC$=20$ measurement are overexposed within the FOV and thus not valid.
At any point the diffraction curve is several magnitudes below the measured values. This indicates that other stray light processes add radiation to the diffraction signal, independent from the angle of incidence. Comparison of curves shows that the slopes of the measured values agree with the slope of the diffraction curve for angles beyond $5°$. When moving closer to the center, the slopes differ due to ghosts reflections.
It should be noted that the measurement values are averaged over the whole detector image and thus also incorporate variations of the diffraction in two dimensions while the integrated diffraction function only covers variations along the horizontal axis of the detector. It can be expected that the theoretical diffraction curve overestimates the effects when it is generalized for the entire detector image, as done here.
Instead of comparing averages, also single pixels can be compared to their diffraction function. The results for three pixels are shown in Figure 7.4. There, the diffraction function is only integrated over the angular space of the corresponding pixel and then normalized by the value of the on-axis pixel. Pixel 23 shows good agreement at peak value, that indicates that the normalisation is here also consistent. The peaks at pixel 0 and pixel 46 differ from the peaks of the diffraction curves, which is mainly caused by the ghost effects that cause increased measurement values. At larger angles of incidence, the comparison of measurement values and theory also shows a difference of several magnitudes. That is consistent with the previous results that were averaged over the whole detector. Both results show that aperture diffraction is not the dominant stray light process within the instrument.

7.2.4 Ghost-like effect at elevations above $6°$

In the following, the effect of the different modifications described in Chapter 6.4 onto the ghost-like effect above $6°$ elevation are discussed. The modification with an additional stop between the POM and the IFMS reduces the intensity across the detector, but does not change the shape of the effect. Thus it can be concluded, that the stop does not affect the stray light path. The reduction in intensity occurs because the stop blocks a part of the edge beams.
For the covers above and below the retroreflectors, only the results for $\beta = 6°$ and $\beta = 7°$ differ from from the reference measurements. There, only the overall intensity is changed but not the shape. The additional modification of the beam splitter mounting only differs for $\beta = 6°$. This

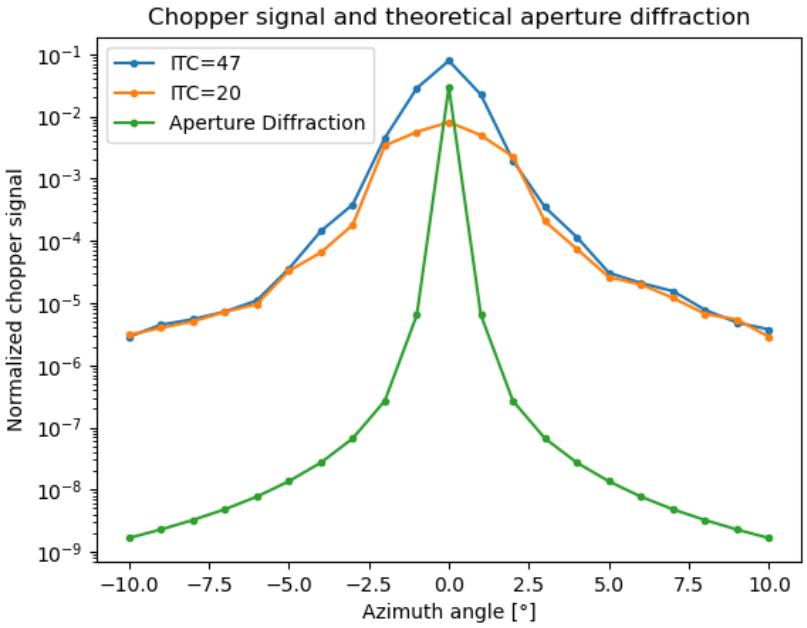

Figure 7.3: Comparison of the results from Figure 6.3 with theoretical aperture diffraction integrated over each pixel and then averaged over the angular space of the detector.

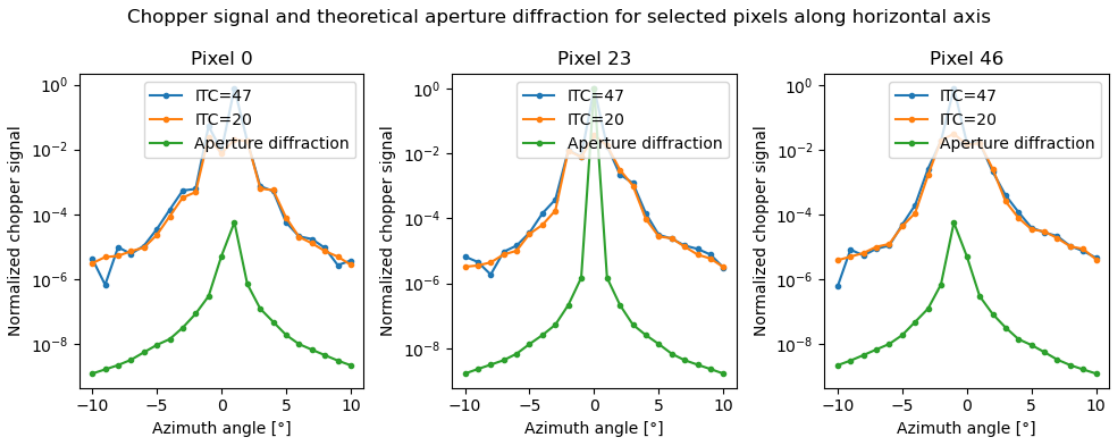

Figure 7.4: Comparison of three pixels with the theoretical aperture diffraction for the corresponding pixel position relative to the angle of incidence of the radiation. The pixel number only refers to their horizontal position. Pixel 0 is located at the left edge of the detector image, pixel 23 in the middle, and pixel 46 is located on the right edge. All pixels are located at vertical pixel row 64 which is the middle of the detector.

leads to the conclusion that the effects observed here are false positives, not actual effects of the modifications. If the covering above and below the retroreflectors affects the results for $\beta = 7°$ one can expect that the reduction of the intensity for the additional modification is at least as big as the initial modification. As the shape of the effect is not changed, it is likely that the intensity reduction is caused by false detections of the chopper frequency. If the frequency is not hit exactly this can lead to underestimation of the signal. At this point the modified surfaces around the retroreflectors and the modifications of the beam splitter mounting are considered to have no effect onto the ghost-like reflection.
The modification within the POM shows a reduction in intensity and a change of the shape of the signal. The reduction is the biggest for $\beta = 8°$ and the lowest for $\beta = 6°$. This shows that the base plates of the pointing cylinder are part of the stray light path, otherwise the signal would not have changed in shape. The variation with β is likely caused by areas that are not completely covered. Especially on the side, where the scanning mirror is mounted, not all surfaces could be covered by the foam. The additional reduction of the entrance aperture of the POM showed a further reduction of the overall intensity. This has the same reason as the previously discussed stop.
The results of the additional coverings at the BSU are similar to the results with the modifications within the POM. As this modification is still in place, it can be concluded, that the modification of the BSU has no effect at all.
As the reflection is caused by reflections within the POM, it is not a ghost effect as defined in Chapter 2.2.1 because the cause is no refractive element. A proper reduction of the reflectivity within the rotating cylinder of the POM would significantly reduce this reflection.
This effect reflects light from more than 6° above the LOS to the detector. During balloon operation, this angular area is always above the horizontal. Depending on the elevation of the LOS, this angle looks into the deep space and receives only very weak signals from the atmosphere. In this case, the effects of that reflections onto measurement quality small. But for future planned aircraft operation this might be important. There, the instrument has more structure around, which could cover the relevant angular space. In this case, the warm and radiant aircraft structures could have significant effects onto measurement quality caused by that reflection.

7.2.5 Stray light effects at large angular distances from the LOS

The different measurements showed spot-like stray light effects when the azimuth angle between source and LOS was big. Those effects are not very strong, but still can affect the measurement quality. For large negative azimuth angles, the effect depends on the position of the interferometer carriage. Thus, the light is either reflected by the corner cube reflector or the interferometer carriage itself into the optical path, or the interferometer carriage blocks the stray light path at all other positions. For positive azimuth angles these effects are not affected by the interferometer carriage position. The large angular distance between source and LOS together with the point-like shape of the stray light effect speaks for reflections at some surfaces as cause. Due to the design of the instrument, the walls of the interferometer housing are most likely involved in the stray light path.

7.2.6 Comparison of the effects during gondola rotation in flight and reproduction in lab

The results in Chapter 6.2 show that it was possible to reproduce the effects seen during the rotation of the gondola during flight in the lab measurements. The best agreement between flight and lab was found for the measurements with $\phi_{BB} = 3°$. The most obvious difference between lab and flight is the distribution of intensity, shown in Figures 5.11 and 6.5. During flight, the spot on the right side showed more intensity than the spot on the left side. In the lab measurements, the spot on the left side is more intense than the one on the right side. The ratios of the intensities also do not agree. The differences in the intensity distributions may be explained by the different measurement principles during flight and laboratory measurements: The flight data are calibrated radiances that incorporate radiation from all sources: Sun, atmosphere, and earth. Thus anything seen is a superposition of all these sources. On the other side, the lab measurements use blackbody radiation modulated by a chopper. After applying the digital lock in process, only the chopper signal is left. So there is no superposition with radiation from other sources. This may cause the observed differences.

The comparison between laboratory and flight data also allows for some conclusions regarding the quality of the attitude data during flight. In the laboratory the relative angles and positions are well known, whereas the same data during flight have uncertainties as discussed in Chapter 7.1.1. During flight, the sun was located 3.7° above the LOS. Now, one would expect that lab measurements with the blackbody located 3.7° above the LOS would generate the best reproduction of flight effects. As already discussed, this is not the case. The best reproduction is provided by the 3° measurements. Taking the lab measurements as accurate, this leads to an expected elevation offset for the LOS during flight of $-0.7°$. This offset roughly agrees with the one provided by (S. Johansson, personal communication, 2025) of $-0.6°$ and the offset of $-0.46°$ gained from comparison with CNES data. All the different offsets are close together and indicate that the real offset is also in that range. Taking these different values into account, the sun would be around 3.1° above LOS, which is very close to the 3° used in the lab measurement that fits the best.

Comparing the movements of the main spots provides an estimate for the azimuth offset. In the lab results, the movement of the main spot is centered at 0° relative to the position of the BB. During flight, the movement of the main spot is centered around $-0.5°$. This is difficult to identify, and thus carries some uncertainty. It leads to an expected azimuth offset of $-0.5°$. The analysis of the azimuth data from GLite and CNES (G. Maucher, personal communication, 2025) finds an average azimuth offset of $-1.16°$ The expected azimuth offset lies in that range. It should be considered that the azimuth offset varies over time and for the specific time of the gondola rotation, no azimuth data from CNES are provided, so a comparison directly for that time is not possible.

Looking at the results together with the previous discussion of the beam splitter ghost in Chapter 7.2.2 leads to an explanation of the effects observed in flight and lab measurements. Radiation by the sun or the blackbody is reflected or diffracted into the optical path of the instrument. This would generate one spot at the top of the image. If this occurs before the light passes the beam splitter, the single bright spot generates ghost images to the left and right caused by the beam splitter. The distances between the spots seen in the lab are 37 pixels for the left spot and 36 pixels for the right spot. In flight, the distances are 42 pixels for the left spot and 36.5 pixels for the right spot. These

values are close to the theoretical values. The intensities of the spots are also close to the theoretical values.
The deviations between lab and flight data described likely occur because the lab measurements do not exactly replicate the situation in flight. During the lab measurements the angle of the scanning mirror G_E was set to $-0.15°$. During flight, G_E was varying between $-1.57°$ and $-1.61°$. This leads to a different optical path through the POM which may cause the deviations.

7.2.7 Point source transmittance

The point source transmittance (PST) provides a good description of the amount of radiation and its origin in the angular space that reaches the detector. As naturally expected, the main part of the radiation reaching the detector comes from within the FOV. A significant fraction of the radiation originates within a cone of $\pm 4°$. Angles larger than $4°$ contribute only a small part.
The PST that refers to a single detector row shows that the main contribution in the angular space corresponds with the vertical position of the pixel row. There, the effects of the vertical ghost are also visible.
The adapted PST definition here leads to some uncertainty regarding the usage of the brightest pixels as normalisation factor instead of using the radiance incident at the aperture. The brightest pixels themselves are affected by stray light, so additional stray radiation brought onto those pixels affects the normalisation of all values.
The angular resolution of $1°$ along azimuth and elevation axis is not sufficient for further use of the data. because of this, not each pixel row has a measurement position, where it looks right onto the blackbody. This leads to a strong variation in the peak values of the PST. Thus, the comparison of different pixel rows is difficult. For future use of the PST data in the processing of the measurement data, the PSTs for different pixel rows have to be comparable. In addition, it is useful if the integral over the PST for each pixel row is normalized. If the peak values vary strongly and the whole measurement carries the described systematic error, this is not possible. Especially measurement positions with low values are affected by the artificial enhancement of the signal due to the chopper frequency detection algorithm that has been discussed in 7.2.1. This leads to overestimation of the PST at the edges of the measurement area.

7.2.8 Simulation of radiation contribution with measured PST

This chapter shows how radiation from different angles contributes to the radiation that is incident on the detector. This investigation is based on a forward calculated radiance profile provided by (S. Johansson, personal communication, 2025). This profile is based on atmospheric data for the time and position at which GLite was during the first flight on 23.06.24 between 00:00 UTC and 02:50 UTC. It provides radiances averaged over the spectral range from $7\,\mu$m to $14\,\mu$m and covers the elevation range from $0.4°$ to $-5.3°$ relative to the horizon. The profile is extended to higher and lower elevations by fitting an exponential function to it. Based on the observer altitude of 40 km, the earth is visible at elevations below $-6.4°$. The radiance from the earth is simulated as an ideal

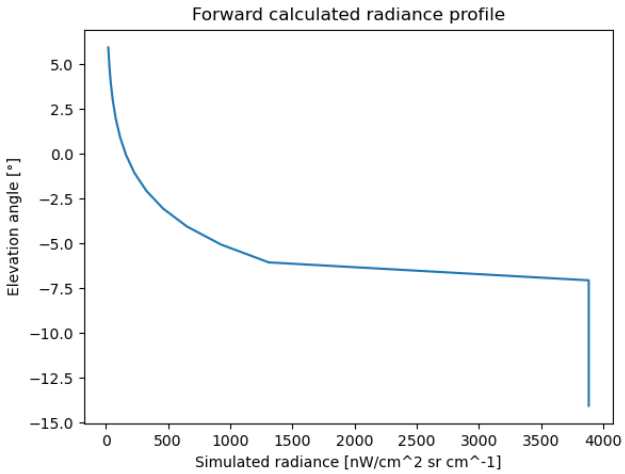

Figure 7.5: Forward calculated radiance profile from atmospheric data for an observer altitude of 40 km. Below -6.4° the earth is simulated as ideal blackbody with 253.15 K. The elevation on the y-axis is relative to the horizon. The radiances are averaged over the spectral range from 7 μm to 14 μm.

blackbody with a temperature of 253.15 K. This radiance is also averaged over the spectral range from 7 μm to 14 μm. The radiance from the earth extends the radiance profile to lower elevation angles. The final profile is shown in Figure 7.5.

This profile is now multiplied with the PST profiles described in Chapter 6.5. In this way a measurement with the LOS at elevation angle -4.07° is simulated. This LOS was chosen because it is one of the two angles used during flight measurements, as described in Chapter 5.1. The result is shown in Figure 7.6. This plot shows the contribution of different elevation angles to the radiance incident on the given detector pixel rows. The most radiations comes from the area within the FOV, where the peak corresponds to the position of the pixel row: Pixel row 0 has its peak at the upper edge of the FOV, while pixel row 127 has its peak at the lower edge of the FOV. For pixel row 0, the contribution of the vertical ghost is in the order of $10\,\mathrm{nW/cm^2\,sr\,cm^{-1}}$ and thus cannot be neglected. The atmosphere at positive elevations contributes only a little. Contribution from the earth and deeper atmospheric levels range from $-0.1\,\mathrm{nW/cm^2\,sr\,cm^{-1}}$ to $10\,\mathrm{nW/cm^2\,sr\,cm^{-1}}$.

For pixels in the upper part of the detector, elevations above the FOV contribute a bit more compared to pixels in the lower part of the detector. For elevations below the FOV the behaviour is similar: Lower pixels receive more contribution from those elevations compared to pixels in the upper half of the detector. As more radiation is coming from below the FOV, pixels in the lower half receive more radiation.

It has to be considered that the limitations discussed for the PST in the previous section also apply to the simulated radiance contribution here. Thus, the radiance contributions at the edges of the measurement space are overestimated. The peak values of the pixel rows also show stronger variation than they should. Thus, the simulation of a measured radiance profile which would be possible by integrating the contribution curves of each pixel over the elevation angle, is not meaningful. This simulation shows that stray light originating from the lower part of the atmosphere and the earth can affect the measurement quality. Following the simulation results, the estimate from Chapter 5.1.3 that the stray light effects are in the order of $5\,\mathrm{nW/cm^2\,sr\,cm^{-1}}$ seems reasonable.

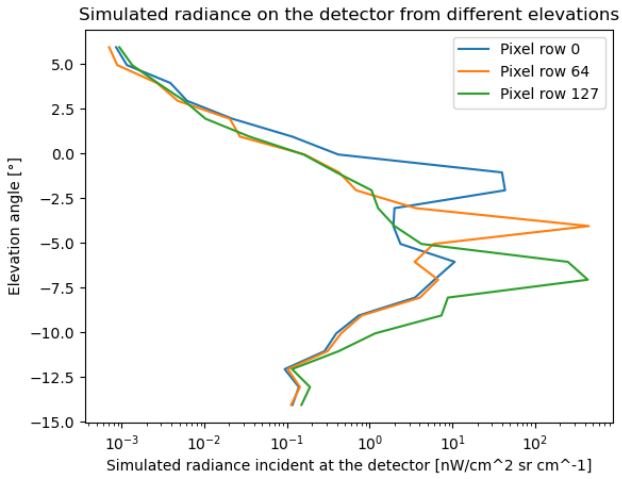

Figure 7.6: Amount of radiation that reaches the detector from different elevation angles, based on the forward calculated radiance profile in Figure 7.5 and the PST profiles. The elevation angle on the x-axis refers to the origin of the radiation relative to the horizontal.

8 Conclusion and outlook

8.1 Summary

This thesis characterised the stray light present in the optical design of GLORIA-Lite. Therefore, data from the first flight of the instrument and lab measurements were analysed. The flight results provided an estimate for the for the amount of stray light present in the optical system of $5\,\mathrm{nW/cm^2\,sr\,cm^{-1}}$. The flight measurements also showed stray light effects caused by the sun during the flight.
The lab measurements showed that it is possible to reproduce the effects seen in-flight in the lab measurements. These measurements provided an qualitative overview of the different stray light effects present in the optical design. The main effects are identified as:

1. Ghost reflections caused by the wedged beam splitter. With intensities of 8.1% and 3.2% relative to the source, they are the strongest effect. The measured values showed good agreement with theory.

2. A reflection that is likely caused by double passing of the interferometer. It has a intensity of 1.1% and 1.6% relative to the source. This effect was not further investigated as it is more useful to do this with a working interferometer.

3. A ghost-like reflection caused by radiation incident from 6° above the LOS. This effect has a intensity in the order of 0.01%. For this reflection, different mitigation approaches were tested and a solution was found. The effect is caused by reflections within the rotating cylinder of the pointing optic module. By reducing the reflectivity of those surfaces, the effect can be reduced.

4. Radiation incident at large angles from the left or right causes spot-like reflections at the sides of the detector image. They are expected to be caused by reflections at the bare metal surfaces of the interferometer housing.

5. Aperture diffraction was also investigated but turned out to play a minor role.

The determination of the point source transmittance provided a first instrument model that considers stray light within an angular space of $\pm 10°$ in azimuth and elevation. This allowed to determine the amount of stray light, that reaches the detector from different directions. This showed that the most radiation reaching the detector originates within the FOV. Most of the stray light outside the FOV originated within a cone of $\pm 4°$ from the LOS. The angular space beyond played only a minor role.

Simulations with a forward calculated radiance profile from real atmospheric data together with the measured PST profiles supported the estimate for the magnitude of the stray light gained from the flight measurements that was mentioned at the beginning of this section.

8.2 Recommendations for design optimization

For further optimization aiming at the reduction of stray light effects in the optical system, the following improvements are suggested:

- Reduction of the reflectivity within the rotating cylinder of the pointing optic module. This optimization has been tested in this thesis and showed a reduction of stray light from more than 6° above the LOS. The reduction can be achieved by coating all metal surfaces with a coating that has a high emissivity in the used infrared range. Thus, the reflectivity of the surface will be low.

- The reflections from the interferometer housing can be encountered by coating the surfaces of the interferometer housing with a material of high emissivity to reduce the reflectivity. Another possibility is the placement of stray light baffles within the interferometer housing. These reduce the number of possible stray light paths and thus block the light.

- By reducing the diameter of the passes between the modules to a smaller diameter, the number of possible paths is also reduced. The same is valid for the placement of additional stops, for example between the POM and the IFMS.

- Lastly, a change in the design of the entrance is encouraged. By placing a stray light baffle at the entrance aperture of the POM, radiation from outside the FOV is prevented from entering the instrument. This is considered a very effective measure.

These suggestions mostly follow the coat it or block it concept mentioned in Chapter 2.5. These concepts allow practical solutions without changing the entire optical and mechanical setup of the instrument. Keeping the instrument clean also reduces stray light by particle contamination. As the instrument will be used in research campaigns under challenging conditions, this is considered to be difficult.

8.3 Future research

For future research, extended measurements with a working interferometer are encouraged. With these measurements it can be determined whether the observed stray light effects are modulated by the interferometer or not. Effects that are modulated will be included in the level 2 products and thus directly affect the retrieved profiles. Stray light that is not modulated will not be visible in the final products but still affects the measurement quality by reducing the dynamic range of the detector.

It is also encouraged to perform the measurement of the PST with increased resolution to provide data that can be used as an instrument model in the operational data processing algorithm.
Finally a testing of the proposed modifications is also encouraged.

9 Abbreviations

FTS Fourier transfor spectrometer

IFTS Imaging Fourier transform spectrometer

PST Point source transmittance

LOS Line of sight

POM Pointing optic module

BDDF Bidirectional diffraction distribution function

BSDF Bidirectional scattering distribution function

SNR Signal-to-noise ratio

FOV Field of view

BS Beam splitter

BSU Beam splitter unit

OPD Optical path difference

ZOPD Zero optical path difference

FWHM Full width at half maximum

MIPAS Michelson interferometer for passive atmospheric sounding

GLORIA Gimballed limb observer for radiance imaging of the atmosphere

GLite GLORIA-Lite

HALO High altitude and long range research aircraft

IFMS Interferometer structure

COP Camera optics

MCT Mercury-Cadmium-Telluride

ADC Analog-digital-converter

IDCA Integrated detector cooler assembly

CNEA Centre national d'etudes spatiales

BB Blackbody

ITC Integration counter

LMI Length-measurement interferometer

Bibliography

Ben, C., H. Shen, X. Yu, L. Meng, H. Cheng, and P. Jia, 2024: Stray light analysis and suppression for an infrared fourier imaging spectrometer. *Photonics*, **11 (2)**, 173, doi:10.3390/photonics11020173.

Brault, J. W., 1996: New approach to high-precision fourier transform spectrometer design. *Appl. Opt.*, **35 (16)**, 2891–2896, doi:10.1364/AO.35.002891.

Centre national d'études spatiales, C., 2024: Succès du vol du ballon « transat » opéré par le cnes. Https://cnes.fr/communiques/succes-vol-ballon-transat-opere-cnes accessed on 13.09.2025, Online.

Ebert, M., 2024: Charakterisierung des gloria lite imaging fourier transform spektrometers. Bachelorthesis, KIT.

Fest, E., 2013: *Stray Light Analysis and Control*. SPIE, doi:10.1117/3.1000980.

Friedl-Vallon, 2025: The novel limb-imaging ftir sounder gloria-lite. 13th international Limb Workshop 2025.

Friedl-Vallon, F., 2023: Flight support application. Tech. rep., IMK-ASF, KIT. Unpublished.

Friedl-Vallon, F., and Coauthors, 2014: Instrument concept of the imaging fourier transform spectrometer gloria. *Atmospheric Measurement Techniques*, **7 (10)**, 3565–3577, doi:10.5194/amt-7-3565-2014.

Holton, J. R., P. H. Haynes, M. E. McIntyre, A. R. Douglass, R. B. Rood, and L. Pfister, 1995: Stratosphere-troposphere exchange. *Reviews of Geophysics*, **33 (4)**, 403–439, doi:10.1029/95rg02097.

Huhs, O., J. Borchardt, S. Krautwurst, K. Gerilowski, H. Bovensmann, H. Bösch, and J. P. Burrows, 2025: Impact of stray light on greenhouse gas concentration retrievals and emission estimates as observed with the passive airborne remote sensing imager mamap2d-light. doi:10.5194/egusphere-2025-2953.

iMAR Navigation GmbH, 2022: inat-m200/tle - inat-m200/xle. Manual, iMAR Navigation GmbH.

Johansson, S., 2019: Analysis of the unusually cold arctic winter 2015/16 lowermost stratosphere by airborne and satellite observations and atmospheric models. Ph.D. thesis, KIT.

Kleinert, A., and Coauthors, 2014: Level 0 to 1 processing of the imaging fourier transform spectrometer gloria: generation of radiometrically and spectrally calibrated spectra. *Atmospheric Measurement Techniques*, **7 (12)**, 4167–4184, doi:10.5194/amt-7-4167-2014.

Kretschmer, E., 2023a: Technical specification pointing optic module. Requirement document, IMK-ASF, KIT. Unpublished.

Kretschmer, E., 2023b: Technichal specification inertial measurement and control unit. Requirement document, IMK-ASF, KIT. Unpublished.

Kretschmer, E., 2024: Gloria-lite mass budget. Campaign preparation document, IMK-ASF, KIT. Unpublished.

Lau, A. S., 1977: The narcissus effect in infrared optical scanning systems. *Stray Light Problems in Optical Systems*, J. D. Lytle, and H. E. Morrow, Eds., SPIE, Vol. 0107, 57–62, doi: 10.1117/12.964596.

Ltd, E. O. C., 2022: Certificate of conformity. Quality data sheet, Evaporated Optical Coatings Ltd. Unpublished.

Marshall, S. J., 1982: We Need To Know More About Infrared Emissivity. *Thermal Infrared Sensing Applied to Energy Conservation in Building Envelopes*, R. A. Grot, and J. T. Wood, Eds., SPIE, International Society for Optics and Photonics, Vol. 0313, 119 – 128, doi:10.1117/12.932890.

Murray, A. E., 1949: Reflected light and ghosts in optical systems. *Journal of the Optical Society of America*, **39 (1)**, 30, doi:10.1364/josa.39.000030.

NASA;ESA; CSA; Leah Hustak, S., 2021: Types of spectra: Continuous, emission, and absorption. Https://science.nasa.gov/asset/webb/types-of-spectra-continuous-emission-and-absorption/ visited on 21.09.2025, Online.

Poli, P., and P. Brunel, 2016: *Meteorological satellite data rescue: Assessing radiances from Nimbus-IV IRIS (1970-1971) and Nimbus-VI HIRS (1975-1976)*.

Rhodes, B., 2019: Skyfield: High precision research-grade positions for planets and earth satellites generator. Astrophysics Source Code Library, record ascl:1907.024.

Riese, M., and Coauthors, 2014: Gimballed limb observer for radiance imaging of the atmosphere (gloria) scientific objectives. *Atmospheric Measurement Techniques*, **7 (7)**, 1915–1928, doi: 10.5194/amt-7-1915-2014.

Scherr, L. M., H. J. Orlando, J. T. Hall, and T. E. Godfrey, 1996: Narcissus considerations in optical designs for infrared staring arrays. *Optical System Contamination V, and Stray Light and System Optimization*, A. P. M. Glassford, R. P. Breault, and S. M. Pompea, Eds., SPIE, Vol. 2864, 442–452, doi:10.1117/12.258334.

Schwab, M. B. W. H., 2021: Pasmi design and analysis report. techreport, SPACEOPTIX GmbH, Hans-Knöll-Straße 6, 07745 Jena.

Sha, M. K., 2013: Characterization and optimization of the new imaging fourier transform spectrometer gloria. phdthesis, Karlsruher Institut für Technologie.

Ungermann, J., A. Kleinert, G. Maucher, I. Bartolomé, F. Friedl-Vallon, S. Johansson, L. Krasauskas, and T. Neubert, 2022: Quantification and mitigation of the instrument effects and uncertainties of the airborne limb imaging ftir gloria. *Atmospheric Measurement Techniques*, **15 (8)**, 2503–2530, doi:10.5194/amt-15-2503-2022.

Ungermann, J., and Coauthors, 2013: Filamentary structure in chemical tracer distributions near the subtropical jet following a wave breaking event. *Atmospheric Chemistry and Physics*, **13 (20)**, 10 517–10 534, doi:10.5194/acp-13-10517-2013.

Wei, L., L. Yang, Y.-P. Fan, S.-S. Cong, and Y.-S. Wang, 2022: Research on stray-light suppression method for large off-axis three-mirror anastigmatic space camera. *Sensors*, **22 (13)**, 4772, doi:10.3390/s22134772.

Acknowledgments

First and foremost i want to thank Michael Höpfner for providing the opportunity to write this thesis in his group under his excellent supervision. I am also grateful to Björn-Martin Sinnhuber for his role as Co-Supervisor.
A big thank goes to Felix and Erik for providing guidance and discussion during the whole duration of the thesis. For their time to answer my questions and providing support in lab and data analysis at any time. I also want to thank the whole GLORIA team, Sören, Anne, Guido, Christoph, Roland and Thomas for the warm welcome, the opportunity to join a research campaign and the support in all issues regarding hardware, software, knowledge about the instrument, the provision of additional data that was beyond my abilities and the share of their decade long druidic knowledge.
I am grateful to my parents and family for supporting on my path whatever i was doing. I want to thank them also for their financial and moral support during my studies.
I want to thank all my friends and colleagues for the wonderful time i had during my time in Karlsruhe.
Last but most important, i want to thank Pia for enduring me during the writing of this thesis and providing nutritional and endless emotional support.

During the preparation of this thesis, following AI tools were used to support translation and grammar and spelling correction: DeepL (https://www.deepl.com/de/pro) and ChatGPT (https://chatgpt.com/).

Erklärung

Ich versichere wahrheitsgemäß, die Arbeit selbstständig verfasst, alle benutzten Hilfsmittel vollständig und genau angegeben und alles kenntlich gemacht zu haben, was aus Arbeiten anderer unverändert oder mit Abänderungen entnommen wurde sowie die Satzung des KIT zur Sicherung guter wissenschaftlicher Praxis in der jeweils gültigen Fassung beachtet zu haben.

Karlsruhe, den 17.10.2025

(Mark Danny Deibele)

Accepted as an examination copy

(Michael Höpfner)